Title
LOW ENERGY ELECTRON DIFFRACTION STUDIES OF PHASE TRANSFORMATIONS AT METAL SURFACES

Author
Goodman, Richard Martin.

Publication Date
1969-08-01

UCRL-19008

eq. 2

LOW ENERGY ELECTRON DIFFRACTION STUDIES OF PHASE TRANSFORMATIONS AT METAL SURFACES

Richard Martin Goodman
(Ph. D. Thesis)

August 1969

AEC Contract No. W-7405-eng-48

LAWRENCE RADIATION LABORATORY
UNIVERSITY of CALIFORNIA BERKELEY

UCRL-19008

eq. 2

DISCLAIMER

TABLE OF CONTENTS

LOW ENERGY ELECTRON DIFFRACTION STUDIES OF PHASE TRANSFORMATIONS AT METAL SURFACES

Richard Martin Goodman

Inorganic Materials Research Division, Lawrence Radiation Laboratory,
and Department of Chemistry,
University of California, Berkeley, California

ABSTRACT

The post-acceleration technique of low energy electron diffraction in ultra-high vacuum has been used to investigate phase transformations at metal surfaces. Investigations of possible order-order surface phase transformations at metal single crystal surfaces were undertaken on the (100) faces of silver, gold, palladium, and nickel. The clean Au(100) surface was found to undergo an order-order surface phase transformation designated Au(100)-1×1 → Au(100)-5×1 in the temperature range 300°-500°K. Studies of the (100) surface of silver and nickel, as well as the (111) face of nickel, show that these surfaces retain a stable (1×1) surface structure even under extreme vaporizing conditions at high temperatures. Lead, bismuth, and tin were melted in situ while monitoring the surface atomic arrangement by low energy electron diffraction. The (111), (100), and (110) surfaces of lead and the (0001) and (01$\bar{1}$2) surfaces of bismuth retain an ordered (1×1) surface structures at all temperatures up to their respective bulk melting points. These surfaces melt spontaneously at a temperature corresponding to their respective bulk melting points.

Background intensities obtained from molten lead, bismuth, and tin surfaces provide information on the atomic scattering factors for low energy electrons scattered by atoms in metal surfaces. Using a Debye-Waller technique the root-mean-square displacement normal to the surface of atoms in low index faces of iridium, palladium, lead, and bismuth was shown to be

one and one-half times larger than the bulk root-mean-square displacements for the respective metals.

I. INTRODUCTION

Low energy electron diffraction (LEED) has already demonstrated its utility for studying the structures of surfaces important to investigations in surface chemistry,[1-3] semi-conductor surface physics,[4,5] and solid state physics.[6] LEED has been used to monitor changes of the surface structure of solids during oxidation[7,8] and heterogeneous catalysis.[9] In the fields of surface dynamics and surface phase transformations progress using LEED has been made in studies on surface diffusion,[10] mean square displacement of surface atoms,[11] and the temperature dependence of surface structures.[12,13] Theories have been presented to describe surface dynamics[14] and surface phase transformations.[15] These theories are not general enough nor do they describe experimental results well enough to be considered accurate descriptions of the nature of surface phase transformations.

The objective of this dissertation is to present data from studies of several different types of surface phase transformations. The surface structures of the (100) faces of silver, gold, palladium, and nickel have been investigated from 300°K to very high temperatures near their respective bulk melting points. The structure of lead, bismuth and tin surfaces have been studied at temperatures as high as their respective bulk melting points; during melting; and in the molten state at and above the melting point. The normal component of the mean square displacement for surface atoms of iridium, palladium, lead, and bismuth have also been determined in an attempt to establish a possible correlation[16] between the melting behavior of solid surfaces and the mean square displacement of surface atoms.

I have investigated the orientation of surfaces of lead and bismuth crystals grown from the melt as a function of the rate of growth. Also,

the surface structure of freshly vaporized silver and nickel surfaces was investigated in order to determine the degree of order present in freshly vaporized surfaces.

These investigations are pioneer efforts using LEED in the study of surface phase transformations. These experiments provide information which is useful in describing surface melting and the stability of different surfaces with respect to surface structural rearrangements, even to the melting points or under extreme vaporizing conditions. The main emphasis of all this work has been on exploratory research and several areas studied in the course of this research should provide a source of much future research.

The most significant result of this research is the discovery that even at temperatures up to the bulk melting point, Pb(100), Pb(111), Pb(110), Bi(0001), Bi(01$\bar{1}$2) surfaces are stable and are not disordered. Indications from studies of freshly vaporized Ag(100), Ni(111), and Ni(100) surfaces are that even under vaporizing conditions the bulk, or (1×1),structure can remain essentially ordered on an atomic scale. These experiments on melting and molten surfaces and on vaporized surfaces are discussed in Sections VI, VII, and IX, respectively. Surface structural changes and studies on crystal growth from the melt are discussed in Sections IV and VIII, respectively. The experimental equipment is described in Section III; the theoretical discussion of LEED is in Section II. All the conclusions and key results are discussed in Section X. Three appendices are provided for the compiling of supplementary data on the specular intensities and surface structural changes obtained in the course of other experiments and to outline several theories of melting.

These experiments have demonstrated the utility of LEED in the study of surface phase transformations and suggest directions for future research in lattice dynamics, diffraction theory and surface thermodynamics.

II. PRINCIPLES OF LOW ENERGY ELECTRON DIFFRACTION

A. Coherence and Diffraction Intensity

The interpretation of low energy electron diffraction data requires the understanding of the principles of two-dimensional and three-dimensional diffraction. For a two-dimensional grating the reciprocal lattice is represented by a series of rods in reciprocal space as shown in Fig. II-1a.[17] The addition of full three-dimensional periodicity to the array of scattering centers leads to a lattice in reciprocal space consisting of points as shown by the small circles in Fig. II-1b. The Ewald sphere represents the surface generated by elastic scattering in all directions of an incident wave of wave vector $\underset{\sim}{k}_o$. The diffraction condition for single scattering is satisfied whenever the Ewald sphere intersects the reciprocal lattice.[18] For two-dimensional scattering this condition is satisfied for any $|\underset{\sim}{k}_o|$ larger than the shortest distance between the reciprocal lattice rods. To satisfy the diffraction condition for a three-dimensional array of scattering centers the Ewald sphere must intersect a reciprocal lattice point. In LEED, $|\underset{\sim}{k}_o| = 2\pi\sqrt{eV/150.4}$ Å^{-1} where eV = the energy of the incident electrons.* Thus, on changing the accelerating voltage of the electron beam the magnitude of $|\underset{\sim}{k}_o|$ is changed. In Appendix B, several such scans of the specularly-reflected beam (i.e. scans along 00-rod as shown in Fig. II-1a) as a function of voltage are indicated. The curves do not fit either the two-dimensional model

---

* From the deBroglie equation

$$|\underset{\sim}{k}| = 2\pi/\lambda = 2\pi(p/h) = 2\pi\sqrt{2m_e E/h}$$

where m_e = mass of the electron, E = electron energy, h = Planck's constant. Substitution of appropriate values gives the constant, 150.4, above.

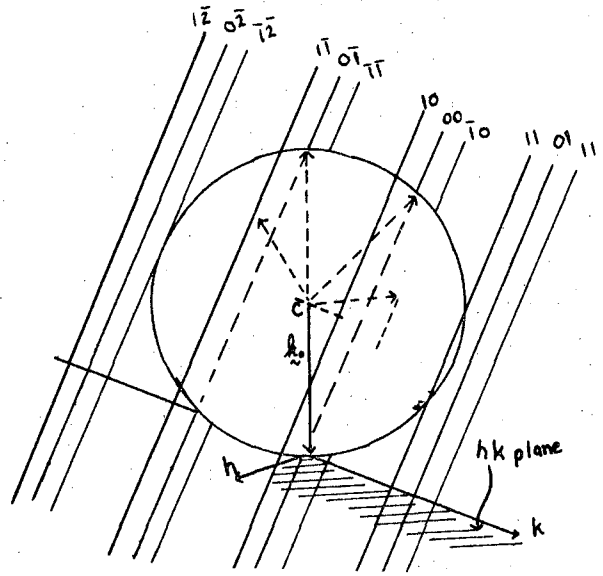

Fig. IIA-1a Reciprocal lattice for a two-dimensional grating.

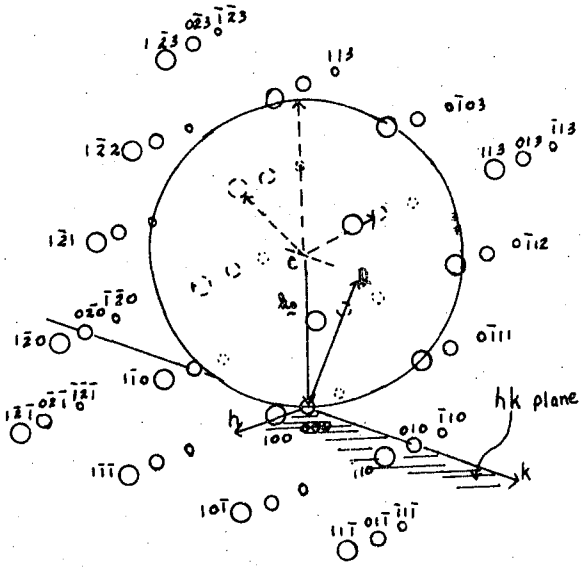

XBL 696-700

Fig. IIA-1b Reciprocal lattice for a three-dimensional array. The dashed arrows represent allowed diffraction beams. The solid circle represents the Ewald sphere whose radius is proportional to $1/\lambda$; the numbers represent the Miller indices, h k ℓ, for the allowed diffraction points.

(where intensities would be constant as a function of voltage) or the three-dimensional model (where the intensities would show very sharp maxima and minima as in x-ray diffraction). Rather the curves indicate a modulation of intensity as a function of beam voltage. Using simple kinematic models, Lander[17] indicates that this modulation corresponds to scattering from about 2-6 atomic layers for most materials at moderate electron energies (25-200 eV).

Several researchers, e.g. Farnsworth,[19] Taylor,[20] and Estrup and Morrison[21] have epitaxially deposited materials on foreign substrates and find that the diffraction patterns characteristic of the substrate deteriorate rapidly after one or two monolayers have been deposited. After the deposition of 5-10 atomic layers the epitaxially grown films give diffraction patterns characteristic of the bulk phase of the freshly deposited epitaxial materials.

Experiments indicate that the number of elastically scattered electrons back-reflected from crystal surfaces is found to vary with incident electron beam energy; about 20% of the incident electrons back scatter elastically at 10 eV, about 1% at 100 eV, and less at higher energies.[17] The inelastically scattered electrons contain much valuable physical information which recent advances in Auger spectroscopy[22] promise to uncover. However, no such experiments on the inelastically scattered electrons were undertaken as part of this work.

Perhaps one of the most crucial questions in using LEED to study phase transformations concerns the number of atoms which lead to coherent scattering. Heidenreich[23] indicates that incoherence sets an upper limit to the number of atoms which can contribute to coherent scattering. This incoherence arises from two effects, first, the finite size of the

electron source, and second, the incoherence due to spreading of the wave packets over the distance between two scattering centers. This latter distance is usually referred to as the Fresnel zone. If r = width of Fresnel zone = $(R\lambda/2)^{1/2}$, where R = distance from scattering center to detector, and λ = wavelength of the incident wave, then using the appropriate values for LEED: $R \cong 7\times10^{8}$Å, $\lambda \cong 1$Å; gives $r = 2\times10^{4}$A. However, because of the need for high intensities in LEED, the instrumental incoherence introduced by the use of a large electron source is much more significant. The coherence width of the electron beam at the scattering object,

$$\Delta X = \frac{\lambda}{2(1+\Delta E/2E)\beta_s} \qquad \text{IIA(1)}$$

where β_s = half angle indeterminacy in the angle of incidence for an incident electron due to the size of the electron source, ΔE = thermal spread of electron beam, and E = energy of the electron beam. In LEED, $\beta_s \sim .001$ radians, $\lambda = 1$Å (for E = 150 eV), $\Delta E \sim .2$ eV. These values give a coherence width of about 500Å, i.e. much smaller than the width of the Fresnel zone. Thus, in LEED, no area larger than $\sim(\Delta X)^2$ can contribute coherently to the diffraction pattern since no area larger than this receives coherent radiation.

The question of what is the minimum area necessary to give a coherent diffraction pattern has not been definitely answered experimentally. However, if one assumes that ordered arrays of 25-100 atoms are sufficient to give coherent diffraction best agreement with present results is obtained. Thus, considering all of these factors, we can characterize coherence in LEED by the following description: minimum order necessary to give a coherent diffraction beam consists of ordered patches of about

10% of the crystal surface. As the surface is further ordered, the intensity of the diffraction spots should increase, and the sharpness of the spots improve until the surface consists almost entirely of regions of ordered arrays of about 10,000 atoms. Beyond this degree of ordering, the experimental factors prevent any improvement in the pattern; the macroscopic beam width (about 1 mm^2) limiting the sharpness of the spots, and the source incoherence limiting the intensity.

Returning to the calculation of LEED intensities; at normal incidence the two dimensional grating formula gives for the location of the diffraction spots; $n\lambda = d_{hk} \sin \theta_{hk}$, where d_{hk} = interplanar spacing on the grating, and θ_{hk} = the angle between incident and scattered beams. Spots appear at diffraction angles in LEED in agreement with the grating formula, however, the intensities are not constant as a function of λ. The intensity of the spots predicted by the simplest three-dimensional kinematic models[17]

$$I = |f_o|^2 \left\{ N + \sum_{n \neq m}^{N} \sum^{N} \cos (\underset{\sim}{k}_o - \underset{\sim}{k}) \cdot \underset{\sim}{r}_{nm} \right\} \qquad \text{IIA-(2)}$$

does not agree with experiment. Here N = total number of atoms contributing to coherent scattering, $|f_o|^2$ = atomic scattering factor, $\underset{\sim}{r}_{nm}$ represents a vector to the nm^{th} atom in the lattice. If the atoms were perfectly ordered then (2) collapses to

$$I = N^2 |f_o|^2 \qquad \text{IIA-(3)}$$

the position of the diffraction spots satisfying the grating law. This result is totally inadequate to explain the intensity data for LEED. Figure IIA-2 shows a theoretical intensity curve from this simple model;

it is in disagreement with a typical experimental curve as shown in Fig. IIA-3. To improve agreement between kinematic theory and experiment the following corrections to this simple model can be applied: (1) Correction for the fall-off of the percent of elastically scattered electrons with increasing electron energy,[17] (2) correction for the degree of penetration by low energy electrons,[17] (3) correction for possible anisotropy between atomic layers near the crystal surface,[24,25] (4) correction for the inner potential, and (5) correction for possible surface expansion.[26] Using models incorporating many of these correction factors reasonably good fits to available experimental data have been made, especially in the higher energy ranges (e.g. Lander[27] on graphite above 70 eV, Rhodin[24] on nickel and copper above about 150-200 eV, etc.). However, at lower energies no kinematic model has shown any particular success in fitting the experimental results. As seen in Fig. IIA-3 intensity curves show far more structure at low energies than is predicted by kinematic models. Dynamical models[28,29] (i.e. those allowing for multiple scattering mechanisms) have been quite successful in predicting positions of maxima and minima in intensity curves, especially in the lower energy ranges. However, primarily due to the lack of knowledge of atomic potentials which are responsible for electron scattering at crystal surfaces, diffraction intensities can only be fitted by the use of adjustable parameters. However, the exciting success in predicting the location of intensity maxima from ab initio calculations and the ability to fit the intensity of many maxima with only a few adjustable parameters promises to increase tremendously the understanding of LEED.

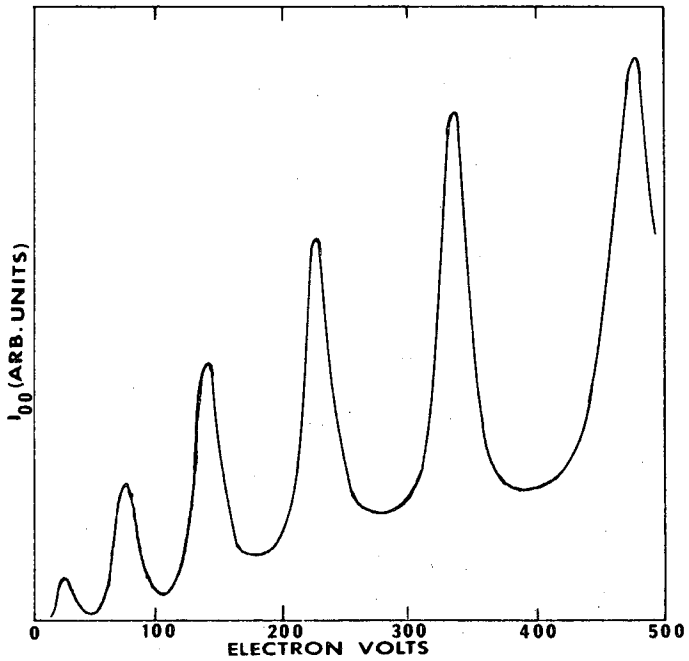

Fig. IIA-2 Theoretical intensity curve for the specularly reflected beam from an ideal lattice having geometry of iridium (100) surface.

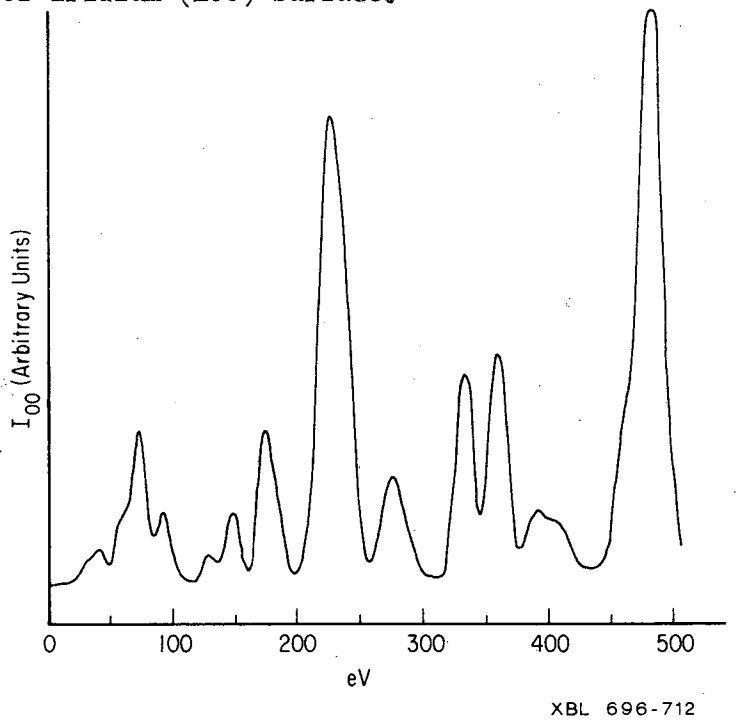

Fig. IIA-3 Experimental intensity curve for the specular beam from an Ir(100) surface.

B. Temperature Dependence in LEED (Debye-Waller Factor)

Real crystal surfaces are neither perfectly ordered nor ideally flat. Real surfaces are highly irregular on an atomic scale with emerging dislocations, steps, pits, grain boundaries, vacancies and regions where atoms are disordered. The atoms in these surfaces are constantly undergoing thermal vibrations. This section is concerned with the effect of these lattice vibrations on the scattered electron beam intensities; the next section will cover the effect of surface disorder on electron beam intensities.

The main effect of lattice vibrations is to scatter a fraction of the elastically back scattered electrons out of phase. Thus the intensity of the diffraction beams decrease while the intensity of the background (background in LEED is defined as all the back scattering excluding the diffraction beams) increases. Electrons of energies of about 100 eV, e.g., spend about $2\times10^{-17}\times \ell$ seconds scattering (where ℓ = distance in Å traversed; t = transit time = $\ell \sqrt{m_e/2eV} \times (\sqrt{10^{-16}}/1.6\times10^{-12})$ where m_e = mass of electron, eV = electron energy). Since characteristic vibrational frequencies are as "slow" as 10^{-12} seconds, the electron "sees" a disordered "snapshot" of the lattice. However, in the laboratory frame we monitor intensities for times of one-tenth of a second or longer and thus obtain an average of a great number of "snapshots." We can calculate the effect of lattice vibrations on laboratory measurements of intensity (including motion due to zero-point energy of an atom, since for the heavy atoms and temperatures used in LEED research these are negligible). Define an arbitrary atom position at 0°K by a vector $\underset{\sim}{r}$ as shown in Fig. IIB-1. At any finite temperature the atom will be displaced by an

amount $\underset{\sim}{u}(t)$, a time-dependent function. The scattered intensity from an array of such scattering centers is:

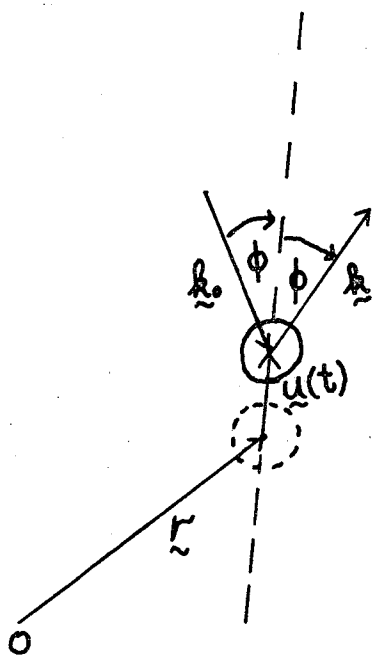

fig. II B-1

$$I = |f_o|^2 \left\{ \sum_{\ell\ell'} \exp\left[i\,(\underset{\sim}{k}-\underset{\sim}{k}_o)\cdot(\underset{\sim}{r}_\ell-\underset{\sim}{r}_{\ell'}) + i(\underset{\sim}{k}-\underset{\sim}{k}o)\cdot(\underset{\sim}{u}_\ell - \underset{\sim}{u}_{\ell'})\right]\right\} \qquad \text{IIB(1)}$$

where we are summing over all pairs of scattering centers ℓ, ℓ'.[30] The first term in the exponential is the interference function given in IIA(2) above.

Without any loss of generality we can expand the displacements in a complete set of the normal lattice mode coordinates:[31]

$$\underset{\sim}{u}_\ell(t) = \sum_{qj} \underset{\sim}{u}_{qj}\, a_{qj} \cos\,(w_{qj}\, t - \underset{\sim}{q}\cdot\underset{\sim}{r}_\ell - \psi_{qj}) \qquad \text{IIB(2)}$$

where the summation is over all the lattice modes q and polarizations, j.

The $\underset{\sim}{u}_{qj}$ are unit vectors in the direction of the phonon of wave vector, $\underset{\sim}{q}$, of frequency w_{qj}, amplitude a_{qj}, and arbitrary phase angle ψ_{qj}.

Following the derivation given by James,[30] Chapter five, the effect of this "phonon" scattering on the scattering intensity can be determined. The assumptions used in this calculation are: 1) the ergodic hypothesis, i.e. that the time average over all the thermal motions (what is actually observed experimentally) is equivalent to an ensemble average of the thermal motions. 2) That thermal motions are symmetric, i.e., that the net (or average) motion along any coordinate is zero. 3) That the thermal motions are small. The result of James' calculations is:

$$I = |F_{hk\ell}|^2 e^{-2W} - |fo^2| e^{-2W} \sum_{\ell\ell'} 2W \cos\{\underset{\sim}{q}\cdot(\underset{\sim}{r}_{\ell}-\underset{\sim}{r}_{\ell'})\} \exp i\Delta\underset{\sim}{k}\cdot(\underset{\sim}{r}_{\ell}-\underset{\sim}{r}_{\ell'}) \qquad \text{IIB(3)}$$

where $|F_{hk\ell}|^2$ is the kinematic diffraction intensity for a perfectly ordered lattice.

In the high temperature limit of the Debye model[32] ($T > \theta_D$) the mean square displacement is given by

$$\langle u^2 \rangle = \frac{3N\hbar^2}{Mk} \cdot \frac{T}{\theta_D^2} \quad , \qquad \text{IIB(4)}$$

where N = Avogadro's number, $\hbar$ = Planck's constant $\div 2\pi$, k = Boltzmann's constant, M = atomic mass in grams, T = °K, θ_D = Debye temperature, thus,

$$-2W = \frac{16\pi^2\cos^2\phi\langle u^2\rangle}{\lambda^2} = \frac{12N\hbar^2}{Mk} \cdot \frac{\cos^2\phi}{\lambda^2} \cdot \frac{T}{\theta_D^2} \qquad \text{IIB(5)}$$

or, (by substitution of $\lambda = \sqrt{150.4/eV}$ and collecting constants),

$$\exp_{10}(-2W) = \exp_{10} \frac{-KVT\cos^2\phi}{M\theta_{D,EFF}^2}, \quad K = \text{const.} = 66.6 \frac{g°K}{\text{mole eV}}, \quad \text{IIB(6)}$$

where ϕ = angle of incidence, and $\theta_{D,EFF}$ = effective Debye temperature.

Equation IIB(6) combined with IIB(3) suggests that at a given beam voltage and angle of incidence the intensity of a diffraction feature decreases as an exponential function of temperature. From this result an effective Debye temperature for the atoms involved in the scattering can be derived. From results using LEED[11,33,34] the value of θ_D for the surface atom is smaller than for bulk atoms. However, as indicated in Section IIA, LEED samples an increasing amount of the bulk as the energy increases. Thus at different voltages, the beam penetrates a different number of layers and the Debye temperature measured is an average of the surface and bulk layers which we designate as $\theta_{D,EFF}$. In the limit of low voltages $\theta_{D,EFF} \rightarrow \theta_D$, surface and at high voltages $\theta_{D,EFF} \rightarrow \theta_{D,BULK}$. Studies of $\theta_{D,EFF}$ as a function of beam voltage provide a means of studying the surface dynamics of crystals as discussed in Sections V and X. However, one must be very cautious in applying Eq. IIB(6). First, the use of the Debye model may not be appropriate to describe surface motions where anharmonic effects could be large. Second, the second term in Eq. IIB(3), usually referred to as the thermal diffuse scattering, must be evaluated. For certain values of "2W" the effect of the thermal diffuse scattering on the Debye-Waller results may be significant.

Maradudin[35] has evaluated the cubic and quartic contributions to anharmonic motion and their effect on the Debye-Waller factor. He obtains the result:

$$2W = \frac{16\pi^2 \cos^2 \phi \alpha_o^2}{\lambda^2} \cdot \frac{T}{\theta_\infty} \cdot 1.861\times10^{-4}\left[1 + 0.0483 \frac{T}{\theta_\infty}\right] \qquad \text{IIB(7)}$$

where α_o = lattice parameter and θ_∞ is a parameter determined independently in Maradudin's model. Using lead as an example, $\alpha_o = 4.95\text{Å}$, $\theta_\infty = 143.4°\text{K}$. One may fit his value for 2W into the form of Eq. IIB(6) if a temperature dependent $\theta_D(T)$ is defined as

$$\frac{1}{\theta_D^2(T)} = \frac{Mk\alpha_o^2}{Nh^2\theta_\infty} \; 0.6205\times10^{-4}\left[1 + 0.0483 \frac{T}{\theta_\infty}\right] \qquad \text{IIB(8)}$$

Using the values for Pb, this becomes:

$$\frac{1}{\theta_D^2(T)} = \frac{1}{154(143.4)}\left[1 + 0.0483 \frac{T}{143.4}\right] \qquad \text{IIB(9)}$$

which for $T \sim \theta_\infty$, gives $\theta_D \sim \theta_\infty$. Maradudin's model indicates that anharmonic effects should be expected to increase linearly with temperature (being about 9% anharmonic at 0°C and about 20% at the melting point) and that to first order anharmonicity only affects the magnitude of the θ_D but not the form of the Debye-Waller factor.

Another effect which is important in LEED studies of the Debye-Waller factor is the second term in Eq. IIB(3) called the thermal diffuse scattering. Thermal diffuse scattering arises from the independence of the phonon modes from each other. Webb et al.[36] have shown that the thermal diffuse scattering intensity, the second term in Eq. IIB(3) is (let I_2 = second term):

$$I_2 = \frac{|fo^2|}{4} e^{-2W} [2W \; I_o \; (\Delta\underset{\sim}{k} \pm \underset{\sim}{q})] \qquad \text{IIB(10)}$$

where $|I_o(\Delta\underset{\sim}{k})|^2 \cdot |fo^2| = |F_{hk\ell}|^2$, i.e., $I_o(\Delta\underset{\sim}{k})$ is referred to as the interference function and is non-zero only where the argument, $\Delta\underset{\sim}{k} = \underset{\sim}{G}$, a reciprocal lattice vector. From Eq. IIB(10), I_2 has significant magnitude only where $\Delta\underset{\sim}{k} \pm \underset{\sim}{q} = \underset{\sim}{G}$. Webb shows that the thermal diffuse intensity falls off in a manner inversely proportional to the distance in reciprocal space from the nearest reciprocal lattice rod. Studying the ratio R of the thermal diffuse intensity to the kinematic intensity Webb finds $R = \frac{2W}{4}(1+\Delta)$ where Δ is a small correction factor, less than unity, and of order $|\underset{\sim}{q}|^2/|\underset{\sim}{G}^2|$ which decreases to zero for large $|\underset{\sim}{G}|$.

We have, thus far, neglected multiple scattering effects, though as indicated in Section IIA they are definitely prominent, especially at low energies. Work in this laboratory[28] indicates that the double diffraction mechanism is the most likely. Figure IIB(2) indicates a possible double diffraction process. An incident beam $\underset{\sim}{k}_o$ making an angle ϕ with the normal to the surface may scatter in two ways: part of the beam is specularly reflected into the beam $\underset{\sim}{k}$, another part scatters into vector $\underset{\sim}{k}_1$. $2\phi_1$ is the angle between $\underset{\sim}{k}_o$ and $\underset{\sim}{k}_1$. The $\underset{\sim}{k}_1$ beam may then be rescattered into $\underset{\sim}{k}_2$ beam (actually identical to $\underset{\sim}{k}$) where the angle between $\underset{\sim}{k}_1$ and $\underset{\sim}{k}_2$ is $2\phi_2$. From simple geometrical considerations: $\Delta\underset{\sim}{k} = \Delta\underset{\sim}{k}_1 + \Delta\underset{\sim}{k}_2$. Physically, the constructive interference between $\underset{\sim}{k}_2$ and $\underset{\sim}{k}$ could contribute to a diffraction maxima. The Debye-Waller factor for the double scattered case is:

$$2W = \frac{KVT}{2M}\left[\frac{\cos^2\phi}{\theta_D^2} + \frac{\cos^2\phi_1}{\theta_{D_1}^2} + \frac{\cos^2\phi_2}{\theta_{D_2}^2}\right] \qquad \text{IIB(11)}$$

where θ_{D_n} refers to the effective Debye temperature for thermal motions

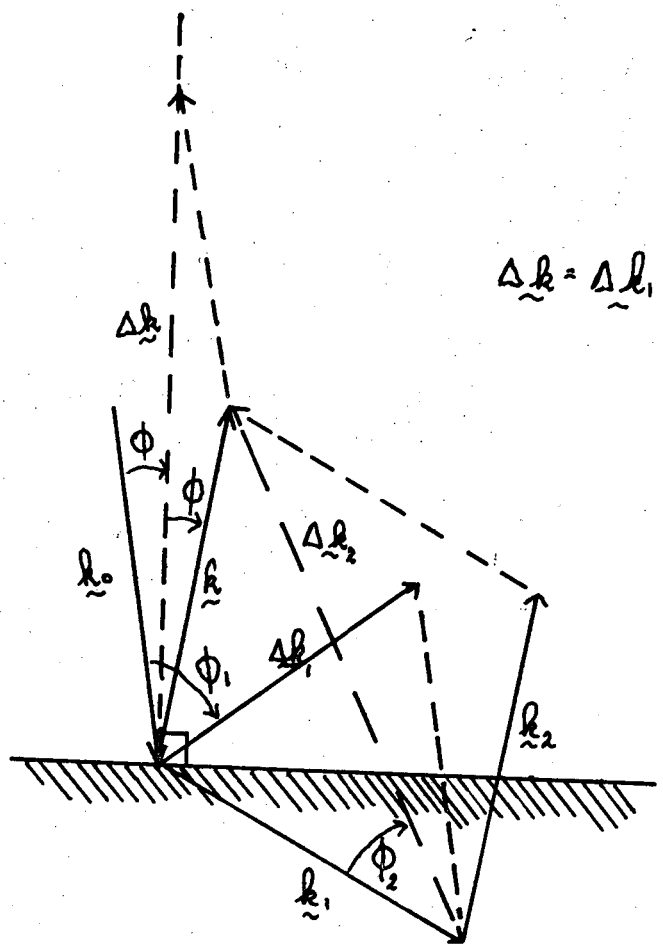

fig. II B-2

XBL 696-707

Vector diagram for the double diffraction mechanism. Note that $\underset{\sim}{k} = \underset{\sim}{k}_2$ and $\Delta\underset{\sim}{k} = \Delta\underset{\sim}{k}_1 + \Delta\underset{\sim}{k}_2$ and $|\underset{\sim}{k}_0| = |\underset{\sim}{k}_1| = |\underset{\sim}{k}_2| = |\underset{\sim}{k}|$.

in the direction of Δk_n. Comparing Eq. IIB(6) and Eq. IIB(11), if

$$\frac{\cos^2\phi_1}{\theta_{D_1}^2} + \frac{\cos^2\phi_2}{\theta_{D_2}^2} = \frac{\cos^2\phi}{\theta_D^2} \qquad \text{IIB(12)}$$

then the results interpreted in terms of kinematic diffraction would be in agreement with this dynamical result. Assuming $\theta_D = \theta_{D_1} = \theta_{D_2}$ this condition is met whenever $\phi = 0°$. However, for ϕ near 0° and $\theta_D \sim \theta_{D_1} \sim \theta_{D_2}$, the most usual case experimentally, the results interpreted in terms of kinematic diffraction do not significantly differ from the dynamical result. But, especially at lower energies, where the differences in surface and bulk θ_D's are most significant and at large angles of incidence, the interpretation of Debye-Waller experiments not allowing for multiple scattering effects could lead to discrepancies. The problem is tractable, however, since dynamical theory does predict the exact multiple diffraction mechanisms applicable and by a form of iterative procedure the θ_{D_n}'s could be determined. This will be further discussed in Section V.

In order to complete the discussion of thermal effects, we must also consider what possible temperature dependent physical phenomena can occur on a crystal surface and how such phenomena will affect the diffraction intensity. As will be discussed in the next section, disordering would lead to a decrease of diffraction intensity. In fact, Estrup[37] has investigated a system in which an adsorbed species (O_2) undergoes an order-disorder transition on the surface of a crystal (W(100)) as the temperature is increased. Attempts to fit the observed intensity decrease with increasing temperature by a Debye-Waller formalism was impossible. However, using a simple Bragg-Williams[38] model for disorder

a reasonable fit of the intensity versus temperature curves was found. Qualitatively, such results are fairly common in LEED work, i.e. frequently patterns due to adsorbed species will show very dramatic intensity decreases as the crystal is heated (the extra spots seem to disappear) even though the absence of a pressure rise suggests the adsorbed species did not desorb. Thus, especially in situations where the cleanliness of the crystal surface is in some doubt, the effect of foreign absorbates on Debye-Waller measurements must be considered. Finally, theoretical calculations[39] predict that surface vacancies may increase rapidly with increasing temperature occupying perhaps, 1-2% of the total surface sites at the melting point. Their effect on the Debye-Waller measurements may be significant. This possibility is discussed in the next section and in Section V.

To summarize: thermal motions introduce two effects in LEED: (1) peak intensities decrease, in fairly good agreement with the Debye-Waller model; (2) the ratio of peak intensity to the background intensity follows the predictions of Webb. Thus, the measurement of temperature dependence of scattered intensity provides a useful means for determining the root mean square displacement of surface atoms and effective surface Debye temperatures. Such experiments are reported in Section V on Pd, Pb, Bi, and Ir. Several factors already discussed above which introduce uncertainty in the interpretations of thermal effects are: (1) anharmonicity, (2) the linear temperature-dependent term in the thermal diffuse scattering (Eq. IIB(10)); (3) multiple scattering of low energy electrons; (4) temperature-dependent disordering; and (5) impurities in the crystal surface.

C. Intensity From Disordered Structures

The discussion has thus far been concerned primarily with the electron scattering properties of idealized surfaces, i.e. perfectly ordered arrays of scattering centers thermally vibrating as harmonic oscillators. Real surfaces, however, contain many imperfections. These are: 1) steps, pits, ledges, etc., 2) vacancies and impurity sites, 3) dislocations, 4) mosaic structures, low angle grain boundaries, 5) liquid-like regions of disorder due to surface preparation, melting, vaporization, or adsorption of foreign substances. The effect of these defects on the scattered intensity is discussed in this section.

If N_T is defined as the total number of scattering centers in an array, then from IIA(2),

$$I = |fo^2| \left[N_T + \sum_{n \neq m}^{N_T} \sum^{N_T} \cos \{ (\underset{\sim}{k}-\underset{\sim}{k}_o) \cdot \underset{\sim}{r}_{nm} \} \right] \qquad \text{IIC(1)}$$

which reduces to $I = N_T |fo^2|$ for a perfectly ordered array.[17] In LEED on real surfaces (assuming the utility of the kinematic models) we are mostly concerned with situations between the two extreme cases of complete order and complete loss of periodicity (disorder). An interesting study of the influence of disorder on LEED intensities is provided by the results of Jona[40] plotted in Fig. IIC-1. In this experiment Jona deposited silicon on a clean Si(111) substrate. Previous studies indicated that under the experimental conditions used in his study, the silicon deposited in a disordered arrangement. In effect then, as Jona deposited more silicon (if he assumed that the coverage was uniform and not patchy) the number of silicon atoms in ordered arrays contributing to the scattering should decrease linearly with the amount deposited. From experiments described

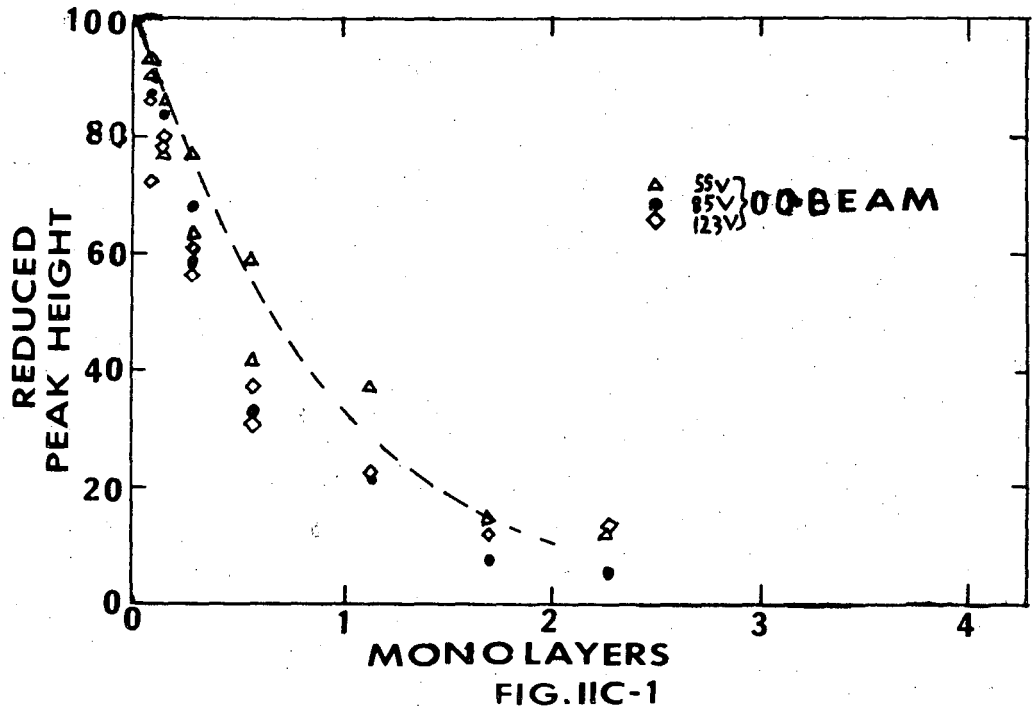

FIG. IIC-1

XBL 696-702

Reduced heights of selected specular intensity maxima (see legend) as a function of the deposited amount of silicon (maximum coverage).

earlier, we concluded that a reasonable estimate for the penetration by low energy electrons was 2-5 layers at low energies. The dotted line in Fig. IIC-1 corresponds to the expectation if 90% of the coherent intensity was from the top three layers and Eq. IIC(1) was accurate. While the fit is not perfect, the results indicate that qualitatively the effect of disorder on LEED diffraction intensities (in the figure the circles, squares, and triangles refer to intensities at diffraction maxima at the indicated beam voltages) can be described by a simple kinematic (single scattering) model.

An interesting effect frequently noted in LEED studies is that random surface irregularities on a macroscopic scale (10^4 Å or larger) do not, in any apparent way, affect the results. Figure IIC-2 is the photograph of the diffraction pattern from a Ni(111) surface taken at an accelerating potential of 174 eV. The sharpness of the spots and the intensity relative to the background is optimum, at least in my experience in LEED. However, as shown in Fig. IIC-3, which is a metallograph under low magnification of this same nickel surface, the surface was macroscopically very rough and irregular having a great concentration of pits, ledges, grain boundaries, etc. of about 1-10μ in size. These results support the basic consideration discussed earlier concerning coherence. That is, if the surface is ordered in patches of perhaps 1000 atoms, then the intensity is unaffected as long as all the patches are oriented with respect to one another as is indicated in Fig. IIC-3 by the registry of the several triangular pits on the surface. Macroscopic steps, pits, ledges, dislocations, grain boundaries, etc. have virtually no effect on either spot size or intensity in LEED as long as the spacing of the defects is of the order of the coherence width of the electron beam or larger. However,

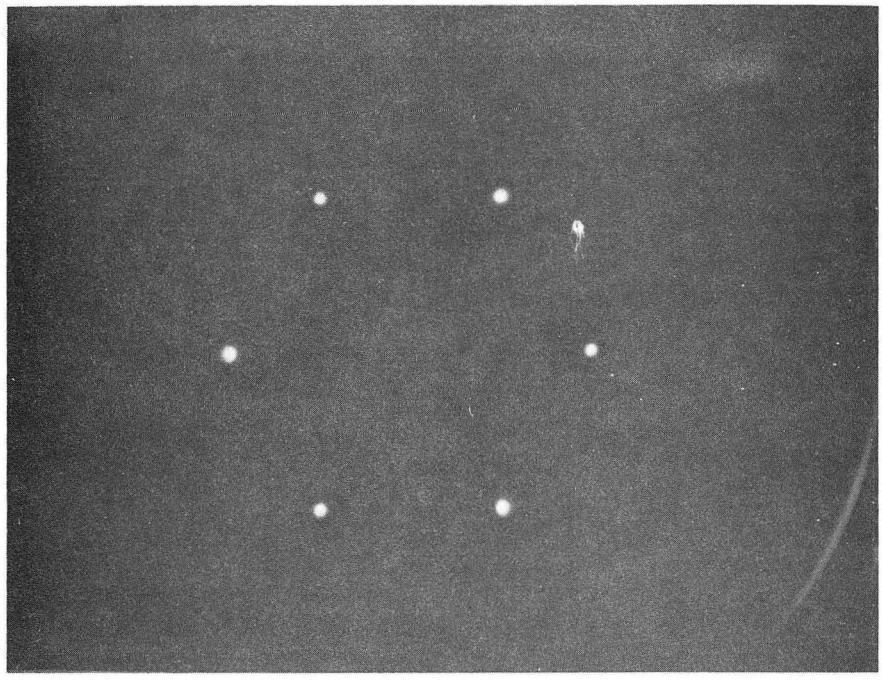

XBB 699-5786

Fig. IIC-2 LEED pattern from a Ni(111)1×1 surface at 174 eV.

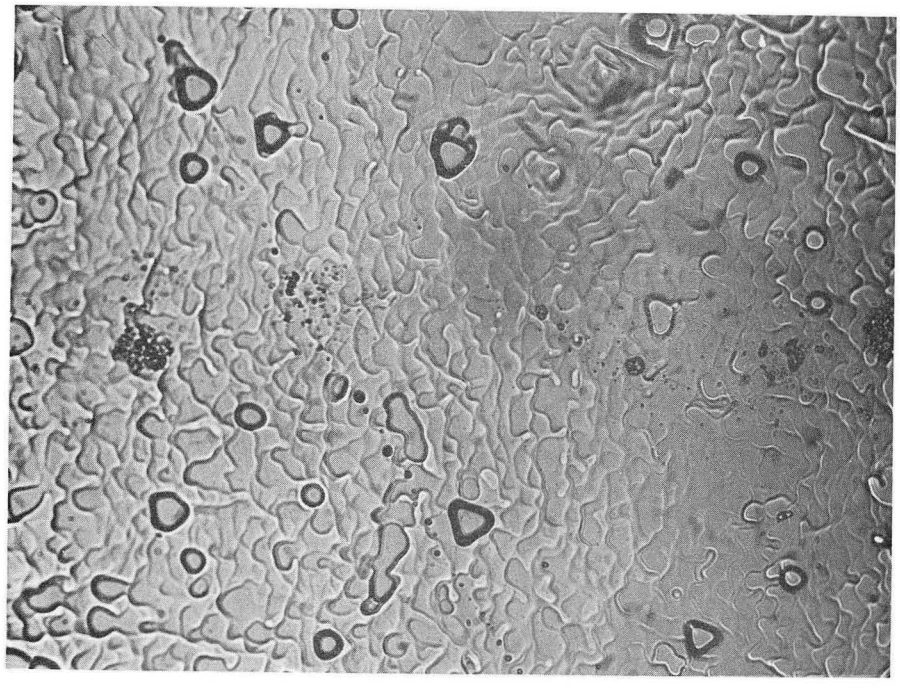

XBB 699-5785

Fig. IIC-3 Optical micrograph of a vaporized Ni(111) surface. Magnification 238×

surface imperfections closer to each other than the coherence width will contribute to an intensity decrease in the diffraction features (similar to results of Jona experiments).

Experimentally, many diffraction patterns have been found in LEED studies which are not characteristic of an equivalent bulk plane parallel to the exposed surface. Many of these patterns are believed to result from structural rearrangements of the surface atoms, i.e. are surface phase transformations. Section IV describes results found on surfaces of many metals and semi-condutors. Models used to explain these new structures will be discussed in Section IV, however, one possible mechanism involves the role of ordered arrays of surface vacancies in producing the structures. The main point to be considered at this time is that vacancies (and/or impurities) if arranged in some ordered or periodic array on a crystal surface can greatly affect the LEED patterns, but that random arrangements have only limited or no detectable effect.

Surface imperfections, which are closely spaced, can have a marked effect on diffraction patterns. Two examples are uniaxial and linear disorder. Uniaxial disorder in LEED can be defined[17] as disorder in which within any one domain the surface atoms are perfectly ordered, but there is no preferred orientation of the domains with respect to each other. The result is that the diffraction pattern shows circular symmetry about the specular reflection. Such patterns have been found on the Au(100) surface[41] and for carbon on platinum surfaces[42] at high temperatures. The ring-like diffraction patterns occasionally become segmented due to partial orientation of the domains as on the Ag(100)[13] surface. Linear disorder occurs whenever atomic spacings along one crystallographic direction are disturbed while maintaining order in the others. A good example is

provided in work by Ellis[43] on UO_2 in which purposely cutting a crystal face off axis introduced very high step densities in the surfaces and streaking in the diffraction patterns. Such streaking is very frequent in LEED patterns, for example, Fig. IIC-4 shows streaking on a Pd(100) 2×2 surface characteristic of a Pd(100) surface in transition from (2×2) → C(2×2) surface structures.[13] An interesting result, discussed in Section VIII, is the tendency for recrystallized tin surfaces to display both uniaxial and linear disorder.

Finally, we should consider the complete loss of long-range order, that referred to as amorphous or "liquid-like" disorder. Guinier[44] separates amorphous structures into two classes: (1) these are correlated disorder which refers to disorder in which the atoms are displaced from equilibrium sites a small amount (relative to equilibrium internuclear separations) and the average positions of all atoms is equivalent to the perfect lattice. The most obvious example is the disorder introduced by thermal motions discussed in Section IIB above. On the other hand, (2) uncorrelated disorder exists when displacements from equilibrium positions may be large and the macroscopic atomic density differs from that due to the ordered lattice. A good example is intensity from a volume containing a monatomic gas at low pressures. The intensity scattered from an array having uncorrelated disorder would show complete uniformity, the diffraction intensity, $I = N_T|fo^2|$ over all reciprocal space as indicated earlier.[17] However, amorphous arrangements of atoms in condensed phases do tend to have some characteristics or correlated disorder. Figure IIC-5 shows a photo of the diffraction pattern from a Ni(111) surface at 109 eV after a very heavy ion bombardment at room temperature. The diffraction spots are almost totally blurred out, but the six-fold symmetry

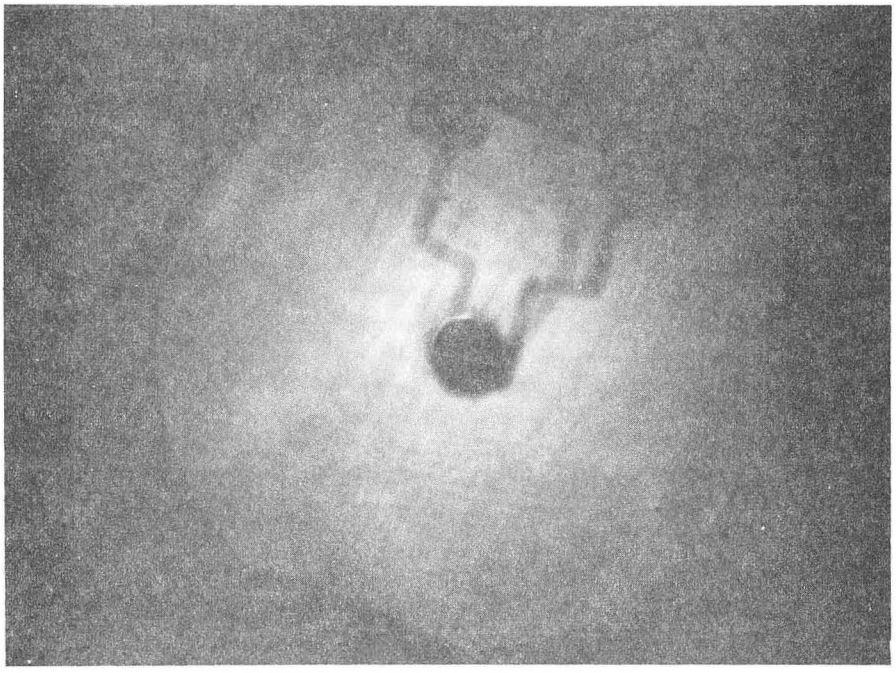

XBB 699-5787

Fig IIC-4 LEED pattern from a Pd(100)-2×2 with streaks at 105 eV.

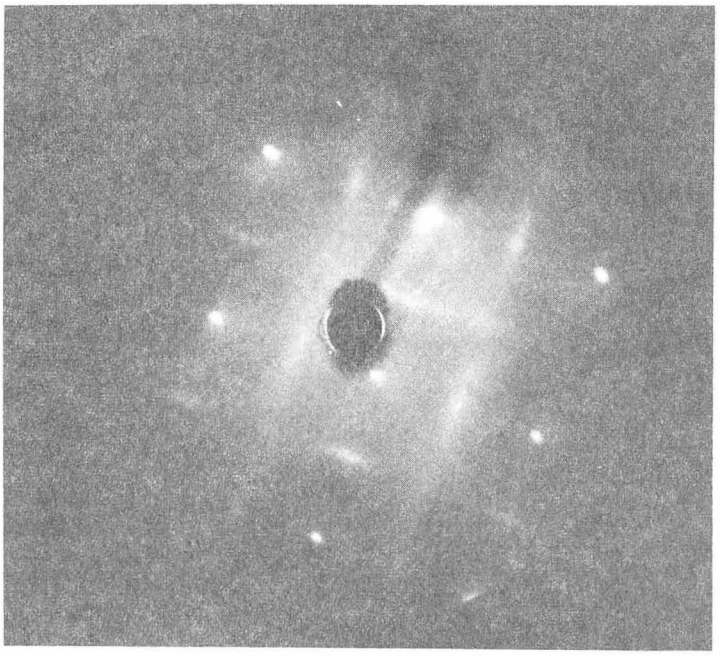

XBB 699-5788

Fig. IIC-5 LEED pattern from a heavily ion-bombarded Ni(111) surface at 109 eV.

characteristic of the substrate is still obvious in the diffraction pattern indicating the surface atoms are still in positions correlated with the bulk. In fact, this photo looks very much like the scattered intensity distribution due to thermal diffuse scattering from an ordered structure.

Liquids possess unique characteristics: like all condensed amorphous phases they possess some elements of correlated disorder. Unlike the ion-bombarded surface structures, however liquids do not show any of the bulk symmetry, but only correlations in internuclear separations (i.e. short range order). The distribution of atoms in liquids can be best described by a radial distribution functions. Figure IIC-7 shows a typical radial distribution function, $\rho_a(r)$, taken from Kaplow's[45] x-ray data on liquid lead. The curve labelled ρ_o represents the average value from the density of the liquid. The main points to observe are: ρ_a goes to zero for small distances (due to repulsions), has a strong maxima near the nearest-neighbor distance of the solids and at large r's, $\rho_a - \rho_o = 0$. For diffraction from an array satisfying such a distribution function, Guinier[44] derives the interference function,

$$I(s) - 1 = \int_0^\infty 4\pi r^2 [\rho_a(r) - \rho_o] \frac{\sin(2\pi rs)}{2\pi rs} dr \qquad \text{IIC(2)}$$

where $s = \frac{4\pi \sin\theta}{\lambda}$. Figure IIC-6 shows typical results for the interference function for a liquid (lead near Tm from Kaplow, et al.[45]). The intensity actually observed is the sum of the three terms shown in Fig. IIC-6. The key point is that the intensity at the first maximum is roughly twice that of the background, the ratio quickly decreasing so that the fourth maximum is almost indistinguishable from the background except by the

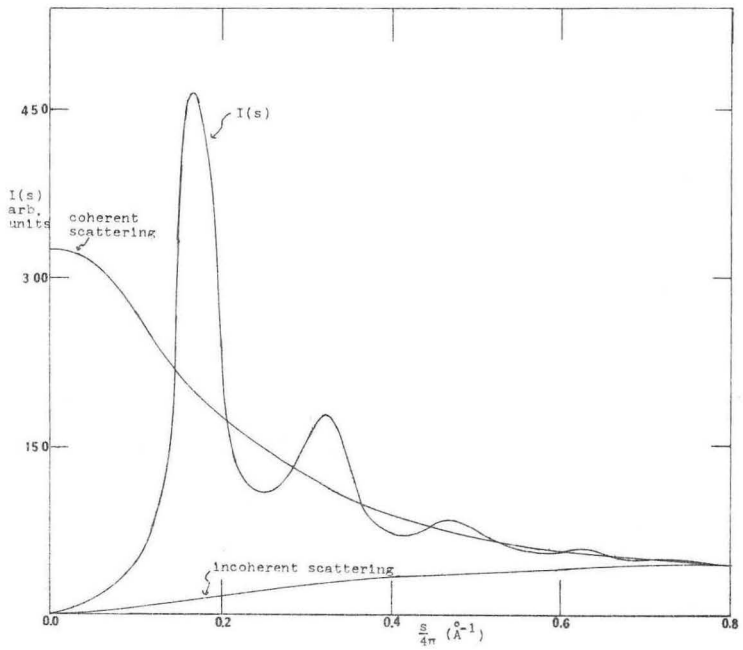

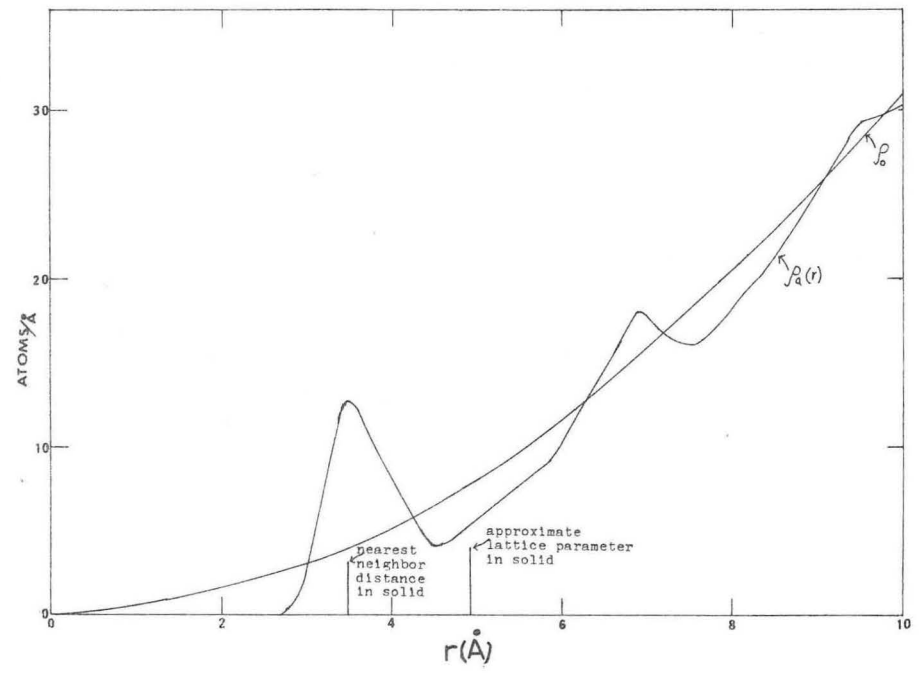

XBL 696-646

Fig. IIC-6 (Top) X-ray intensities obtained from liquid lead at 327.4°C.

Fig. IIC-7 (Bottom) Radial density function for liquid lead at 327.4°C.

most precise experimental techniques. Similar results are obtained for most metallic melts using x-rays as well as high energy ($\gtrsim$ 60 keV) electron diffraction (HEED).[46,47]

Because of the importance of the number of atoms contributing to coherent scattering, LEED should be less sensitive to "liquid" structures than HEED or x-ray diffraction.

From the work of Heidenreich[23] the coherence length, Δx, due to the finite width of the electron source is given by,

$$\Delta x = \frac{\lambda}{2(1+\frac{\Delta E}{E})\beta s} \qquad \text{IIC(3)}$$

which reduces to:

$$\Delta x = \sqrt{\frac{150.4}{eV}} \left(\frac{1}{2\beta s}\right) \qquad \text{IIC(4)}$$

in practice for both HEED and LEED. Thus, the number of atoms per atomic layer, N^*, which can be considered to scatter coherently =

$$\frac{\pi\Delta x^2}{\pi r^2} = N^* = \frac{150.4}{4eV\beta_s^2} \left(\frac{1}{4r^2}\right), \qquad \text{IIC(5)}$$

where r = interatomic distance in the solid.

From data given by Heidenreich[23] one can estimate that $|fo^2| \propto 1/eV^n$ where n is about equal to 2 depending on the technique used to calculate it. We can empirically assign a penetration depth, L, for electrons of any energy based on the variation of scattering cross-sections for electrons derived from Heidenreich's data,

$$L = 2 + (V/150)^2 \qquad \text{IIC(6)}$$

which is a reasonable choice since it gives a reasonable magnitude for penetration depths (L = number of layers transmitted through) in both LEED

(i.e. L varies from 2 → 10 for energies 0-450 eV) and HEED (L varies from 160,000 to 640,000 for energies 60-120 K eV). Obviously, the total number of atoms scattering coherently, N_T, therefore, from Eqs. IIC(5) and (6) is

$$N_T = N^* L = \frac{150.4}{16r^2\, eV\beta_s^2} \left[2 + \frac{eV}{150}\right]^2 \qquad \text{IIC(7)}$$

For most metals, $r \sim 2\text{Å}$ and as indicated above, $\beta_s \sim 10^{-3}$ in LEED (HEED designs often reduce β_s to as low as 4×10^{-4} radians) and HEED. The table below indicates the approximate values of N_T as a function of eV using Eq. IIC(7).

eV =	15	45	150	450	15K	45K	150K
N_T =	5×10^5	7×10^5	2×10^6	7×10^6	2×10^8	7×10^8	2×10^9

Thus, for the most useful range in LEED, $N_T \sim 10^6$ atoms maximum, while for HEED, $N_T \sim 10^9$ for the most useful experimental region. Since intensity varies as N_T^2, it is expected that (excluding experimental difficulties) HEED should be much more sensitive to small degrees of ordering than LEED. Another source of difficulty in detecting radial correlations in liquids using LEED is the presence of the surface which may lead to differences in distribution functions for surface versus bulk atoms, just as surface atomic motions are characterized by a different characteristic θ_D than bulk thermal motions. Finally comparing the Debye-Waller factors for HEED and LEED we find that the LEED intensities are reduced to a far greater extent. In transmission HEED, scattering angles θ satisfy $\sin\theta \propto \lambda/2d$ from the Bragg law and at 60 KeV, $\lambda = 0.05\text{Å}$, $d \sim 2\text{Å}$, therefore $\sin\theta \sim 0.01$. Therefore, the Debye-Waller factor for HEED is

$$2W = \frac{KV_H T \sin^2\theta}{M\,\theta^2_{D,BULK}}$$

and for LEED

$$2W = \frac{KV_L T \cos^2\phi}{M\theta^2_{D,EFF}} \quad .$$

At appropriate voltages for looking at liquid structures by the two techniques, $V_H \sim 60$ keV, $V_L \sim 30$ eV, $\theta^2_{D,EFF} = \frac{\theta^2_{D,BULK}}{2}$, $\sin\theta \sim 0.1$, $\cos\phi \sim 1.00$ and, of course, M, K, and T are the same in both. Therefore, the ratio of the Debye-Waller factors

$$R_{2W} = \frac{2W_{HEED}}{2W_{LEED}} = \frac{60\times10^3}{30} \cdot \frac{(.01)^2}{(1)^2} = .20 \qquad \text{IIC(8)}$$

indicating that HEED intensities are not so affected by thermal effects as LEED intensities. Finally, LEED intensities are much more sensitive to multiple scattering effects which may mask the intensity variations due to the radial density functions. The net effect of these effects is that the sensitivity of LEED to "liquid-like" surface structures is expected to be much less than is HEED for the study of bulk liquids.

In summary, Fig. IIC(8) shows examples of diffraction patterns for an idealized one-dimentional crystal of point-scattering centers.[44] In curve (A) the array is perfectly ordered and of infinite length, thus producing a diffraction characterized by infinitely sharp maxima. For "small" N_1 as in curve (B), the pattern is characterized by definite maxima having finite half width. In curve (C) thermal effects produce a diffraction pattern having reduced intensity and "wings" of thermal diffuse scattering. Curve (D) shows the diffraction pattern from an array made by disordering the lattice (B), as for example, would be characteristic of an

fig.IIC-8

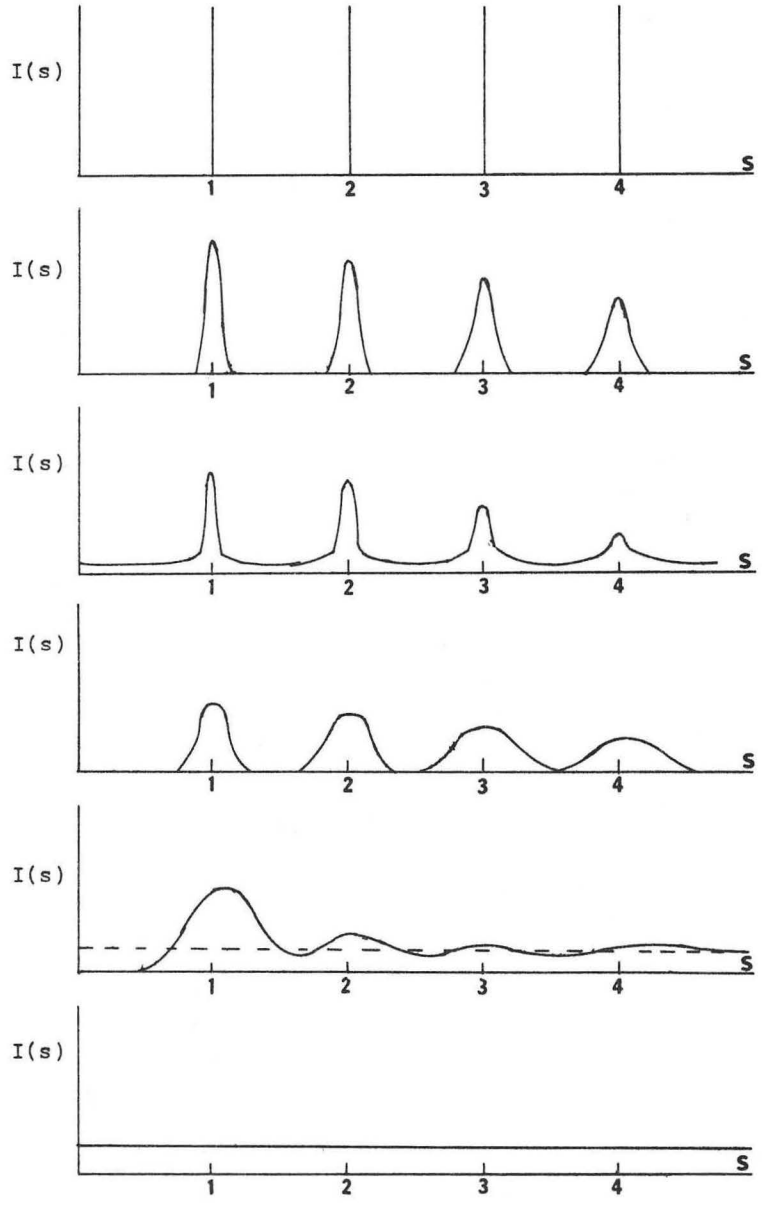

A. Ideal lattice, N→∞

B. Ideal lattice, N small

C. Curve B+ thermal effects

D. Curve B and correlated disorder

E. Liquid structure

F. Ideal monatomic gas

XBL 696-631

ion-bombarded surface. Curve (E) gives pattern if the scattering centers in (B) arranged themselves according to a distribution function characteristic of a liquid. Finally, (F) gives the pattern for the case of point scatterers arranged completely randomly, as in an ideal gas.

III. EXPERIMENTAL

A. Technique of Post Acceleration Low Energy Electron Diffraction

1. Basic Design Features

The instrument used in these studies is the commercially available Varian Low Energy Electron Diffraction (LEED) unit. No significant modifications were made to the unit except those indicated below. The ultra high vacuum system never developed a leak during three years of research and base pressures of $2\text{-}5\times10^{-10}$ torr were routinely obtained after bakeout in virtually every experiment (even in melting experiments where bakeout was only at 175°C instead of 250°C).

The key factor in all LEED studies is the possible contamination of the sample crystal surface. Figure III-1 shows a mass spectrum obtained with a quadrupole residual gas analyzer from a LEED chamber at a base pressure of 1×10^{-10} torr.[25] Table III-I shows the approximate concentrations of the ambient gases estimated from the mass spectrum. Turning on all the filaments (as in the electron optics, ionization gauge, or ion bombardment unit) raised the pressure in the chamber generally to $3\text{-}10\times10^{-10}$ torr, but the ambient composition was not greatly altered. However, the hot tungsten filaments have been shown to produce condensable vapors which can be a source of contamination. Analysis of the ambient composition under ion bombardment conditions ($1\text{-}4\times10^{-5}$ torr Xe or Ar, 140-350V ion accelerating potential, 0.5-2μ amp ion current to crystal) indicates that background contamination is generally less than 0.1% of the pressure of rare gas.[25] In addition to contamination due to the ambient conditions in the diffraction chamber, residues from etching, and polishing of the single crystal samples; thermocouples, crystal

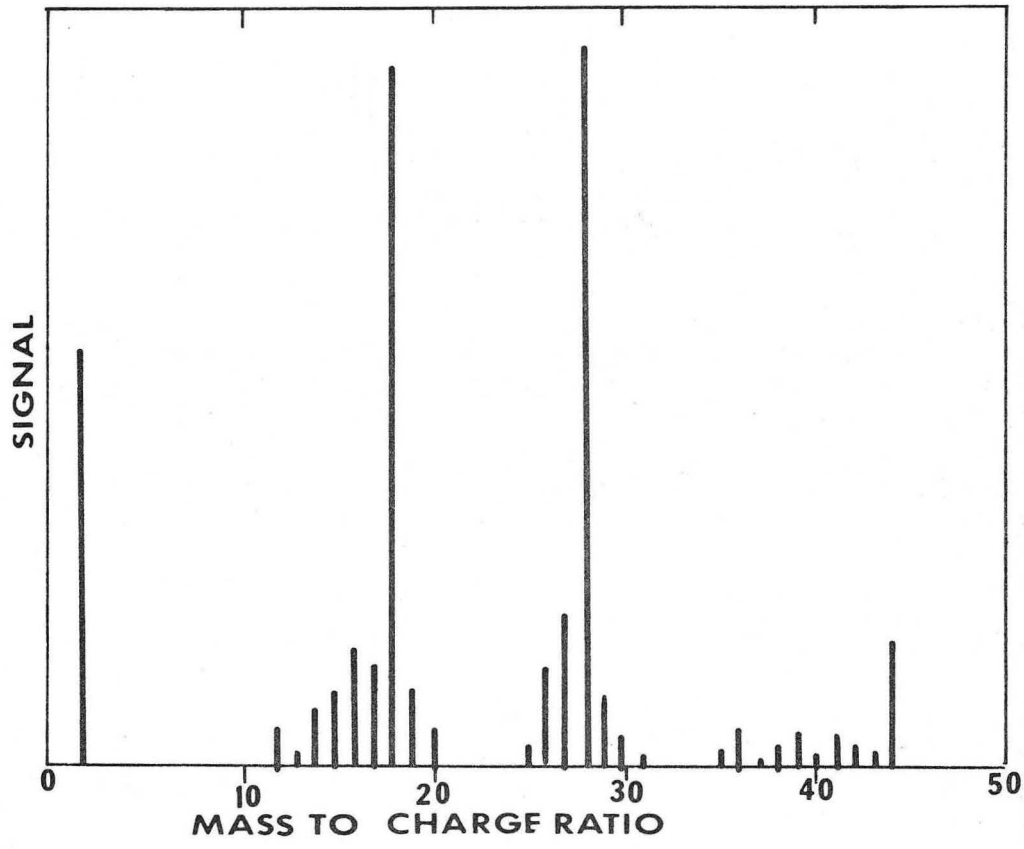

XBL 696-703

Fig. III-1 Quadrupole mass spectrum (1-45 AMU) of LEED ambient background at a pressure of 1×10^{-10} torr.

TABLE III-I

Ambient composition

total pressure = 1×10^{-10} torr

m/e	Possible species	Uncorrected abundance (%)	Uncorrected partial pressure (torr)
2	H_2^+	12	1×10^{-11}
16	CH_4^+, O^+	6	5×10^{-12}
17	OH^+	5	5×10^{-12}
18	OH_2^+	19	2×10^{-11}
28	CO^+, N_2^+, $C_2H_2^+$	19	2×10^{-11}
44	CO_2^+	7	6×10^{-12}
other	O_2^+, Ar^+, CH_3^+, $C_2H_5^+$, C^+ etc.	~32	3.4×10^{-11}
	total	~100	

∴ primary contamination in background (with filaments off) is hydrocarbons, CO, H_2O, and H_2.

holders, and especially bulk impurities can contaminate the crystal surface. for a crystal 10×10×1 mm, a concentration of bulk impurities which exceeds 1 part in 10 million will provide a sufficient number of impurity atoms to produce one tenth of a monolayer of impurities if all the impurity precipitated out on the crystal surface. However ion bombardment can actually remove surface atomic layers (sputtering yield measurements indicate that under the usual LEED ion bombardment cleaning procedures one ion sputters about one substrate atom[48]), for example 10-100 monolayers could be removed by a bombardment of 10 minutes to 2 hours. Thus, repeating heating (to cause diffusion to the surface of those impurities which segregate on the surface) and ion bombardment (to remove those impurities) cycles could remove bulk impurities up to concentrations of 100 parts per million during a typical LEED experiment. At elevated temperatures (especially near the melting point for most materials) surface diffusion of holder material onto the crystal surface can become significant. Considering all of these sources of contamination the following definition of a clean surface can be made: A clean surface (i.e. free of all contaminants in concentrations greater than one-tenth of a monolayer) exists if: bulk purity is greater than 99.99%, the crystal is mounted on holders of similar purity of the same material (or material insoluble in the sample crystal); it has been subjected to several heating and ion bombardment cycles; it is in an ultrahigh vacuum system so that the product of exposure time (in seconds) and background pressure (in torr) is less than 10^{-7}. Of course, if the sticking coefficient of ambient gases is significantly less than unity, or if the bulk impurities do not segregate on the crystal surface, etc., then less stringent requirements for surface purity can be made.

Figure III-2 shows a schematic of the electron optics used during the course of these studies. The power supplies for the filament, filament can,

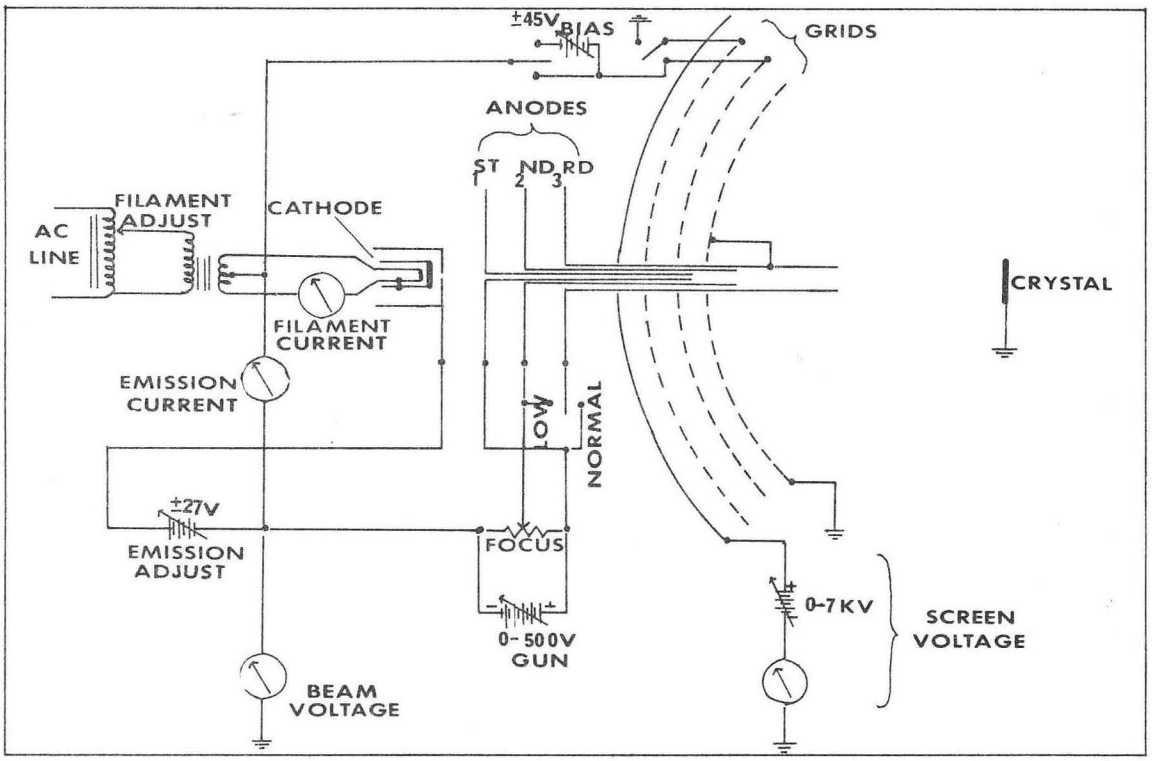

fig. III-2 LEED ELECTRON OPTICS AS MODIFIED

XBL 696-632

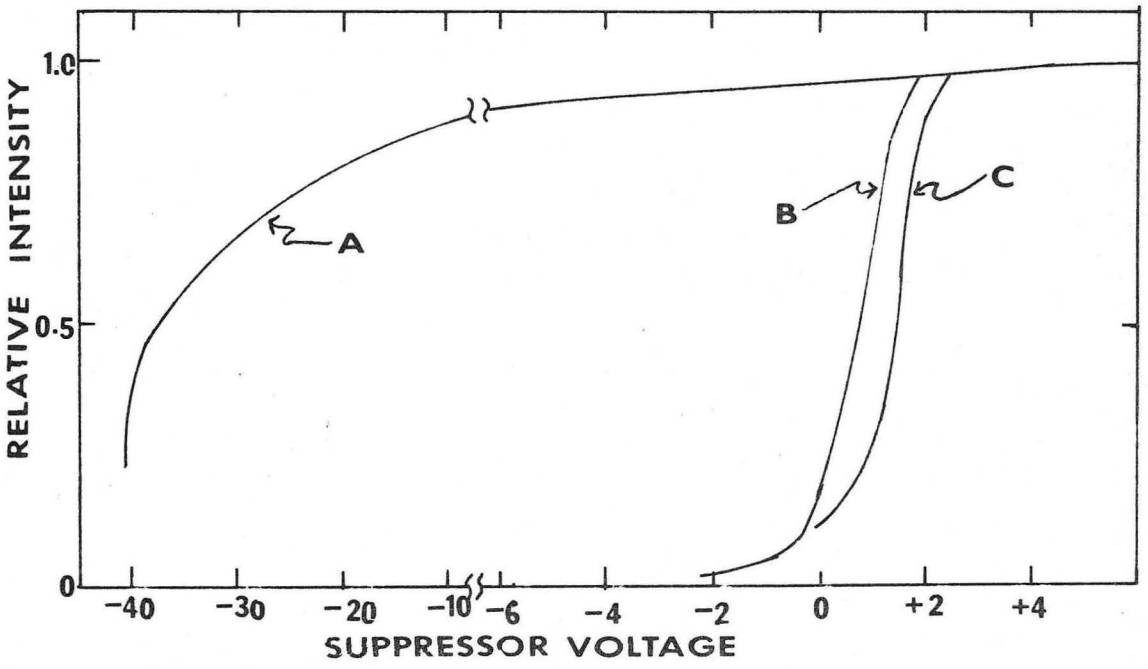

XBL 696-630

Fig. III-3 Cut-off characteristics of a three-grid system. A: first and second grids grounded, third grid is the suppressor; electron optics operate as a two-grid system. B: first and third grids grounded, second grid is the suppressor. C: first grid grounded, second and third grids are suppressors.

cathode, screen, and anodes remain identical to the original Varian design. However, a bariated tungsten cathode has been substituted for the original oxide cathode.[49] Its performance was adequate for these studies; however, the voltage spread in the beam is quite large (as much as 5-7 eV). The addition of a third grid improved the resolution of the optics as shown in Fig. III-3.[50] The bias supply (shown in Fig. III-2) provided a means of investigating the effect of the slightly inelastic electrons on diffraction patterns. The net response of the modified optics was excellent in producing good patterns with sufficient intensity to enable me to do quantitative analysis of the background at lowest electron energies.

Thermocouples (Pt-/Pt-10% Rh, chromel/alumel, Fe/constantan) were used to measure temperatures: whenever possible checks using an optical pyrometer were made. The camera used to photograph the patterns was a Graflex Pacemaker Crown Graphic 45 fitted with a Carl Zeiss Tesser f4.5/135 mm lens and demountable film backs. The films used were Polaroid 57 or 52 for positives and Kodak Royal Pan or Polaroid 55 P/N for negatives. A simple geometrical relationship correlated film spacings to the diffraction angles on the LEED screen.[25] Intensity measurements were made with a Gamma Scientific Model 2000 Telephotometer.

2. Modifications Made for the Study of Molten and Vaporized Surfaces.

Figure III-4 shows the crystal mounting system arrangement used to support the crystal samples and provide coupling to the electrical and motion feedthrough. For the surface structure studies on Au and Pd, the crystals were spot-welded directly to the tantalum strips and the chamber was employed in the usual LEED configuration. However, for the studies on melting and vaporization the chamber was tipped over as shown in Fig. III-5. Diffraction patterns could be monitored in the melting

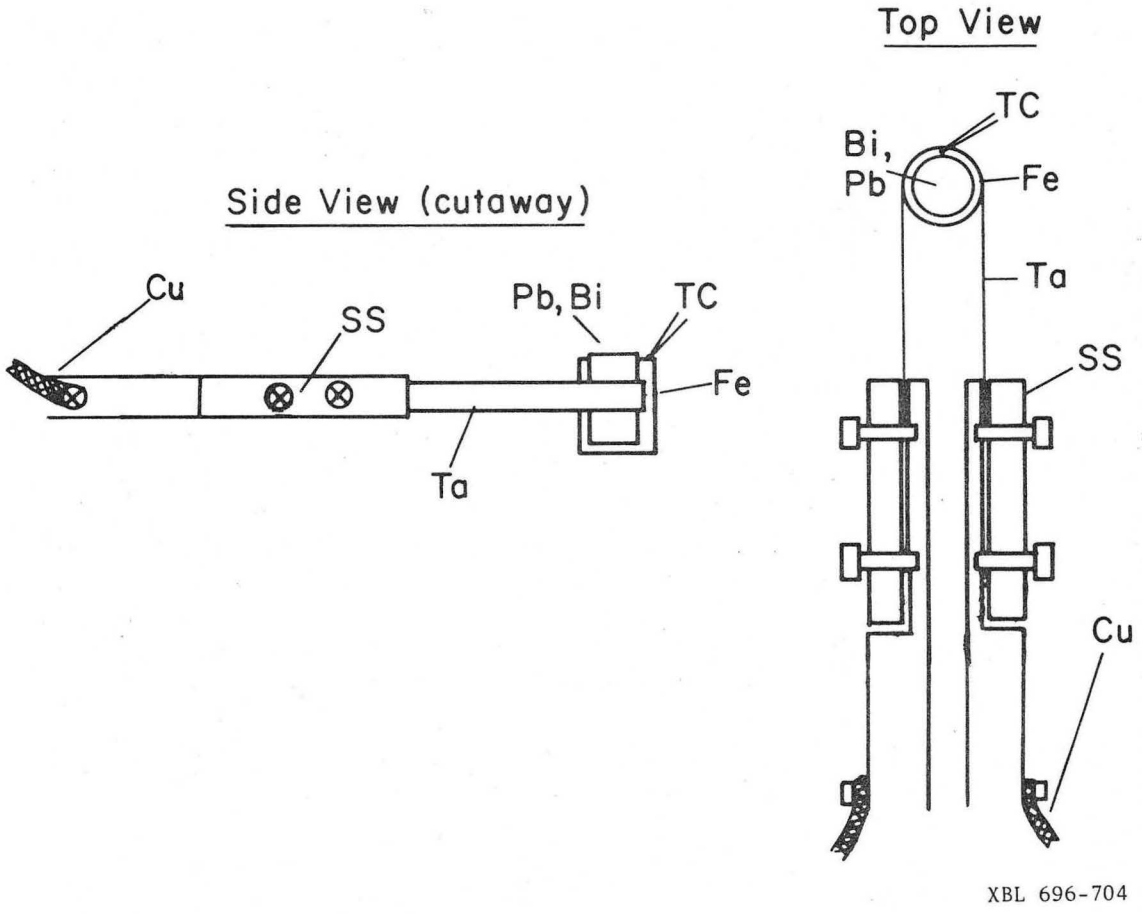

Fig. III-4 Crystal holder assembly for melting studies. For the tin studies the crucible was silicon or molybdenum, not iron.

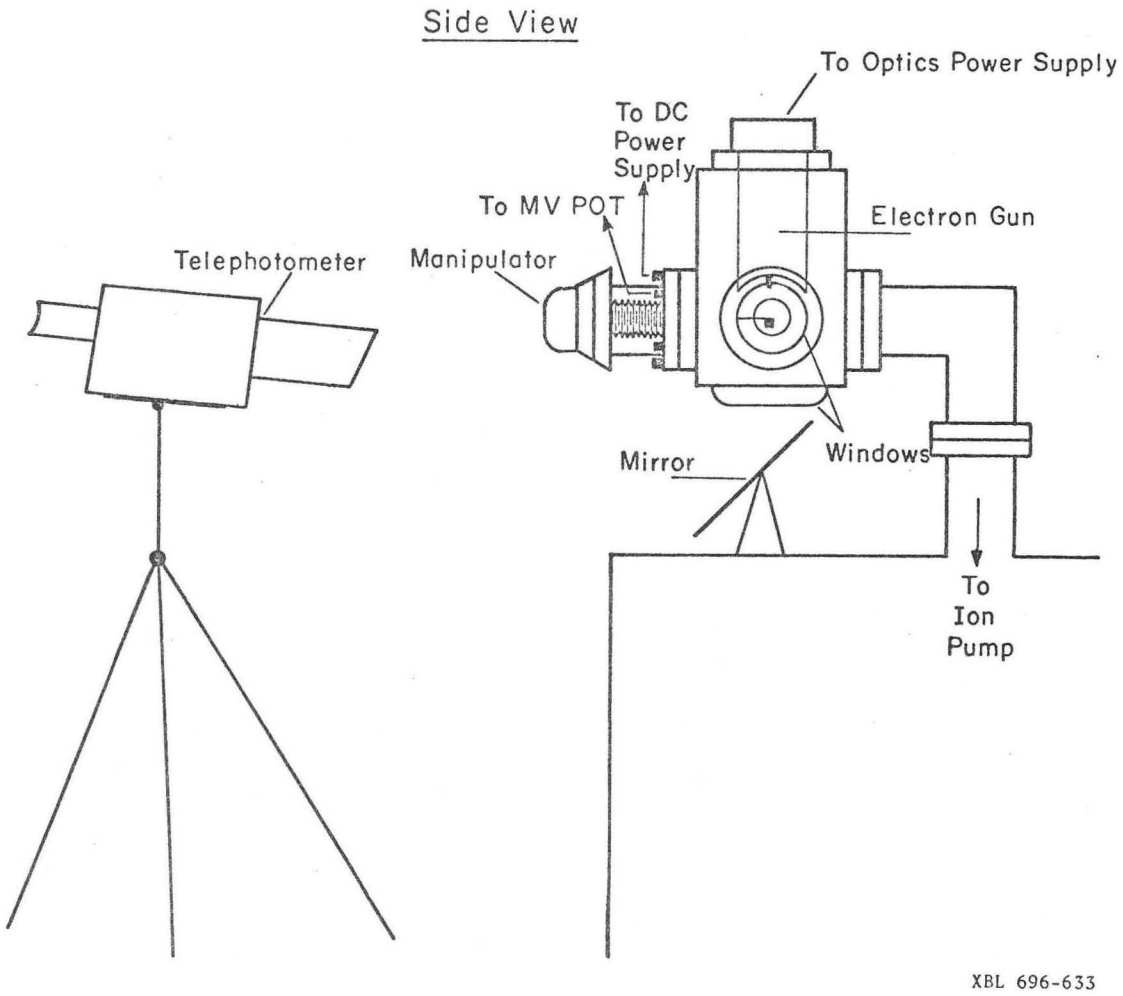

Fig. III-5 Experimental arrangement for the melting experiments.

experiments continuously during heating (by a regulated constant current DC power supply and/or thermal imaging of a 650W projection lamp as shown in Fig. III-6) even to and above the melting point.

For the studies on vaporized surfaces the side window was removed; the manipulator transferred to the side port, the ion gun to the front port and an additional motion feedthrough placed opposite the manipulator. Figure III-7 shows the design of the crystal holder for these studies. By moving the two motion feedthroughs the two halves of the tantalum "can" are brought together (as in Fig. III-7d) which provide an isolated environment protecting the chamber from coating by sublimed metals. After heating the "can is opened" and the diffraction pattern from the crystal is viewed with minimal oscuring of the screen by the Ta can or crystal holders.

Additional studies on lead were made using a low temperature holder previously designed in this laboratory.[51] In all other respects the experimental arrangement was identical to the melting experiments.

B. Crystal Preparation

1. General Procedure

Crystal preparation is a very crucial phase of LEED experiments. The attainment of a reproducibly clean, ordered single crystal surface is a necessary prerequisite for a precise LEED study. Most of the samples used in my experiments were obtained from 1/4 in. single crystal rods.[52] The purities of the crystals used is given in Table III-II. The rods were cut and etched as described below and oriented on a precision goniometer using back-reflection Laue x-ray diffraction generally to $\pm 1^\circ$ of the desired crystal face. After cutting, the crystals were

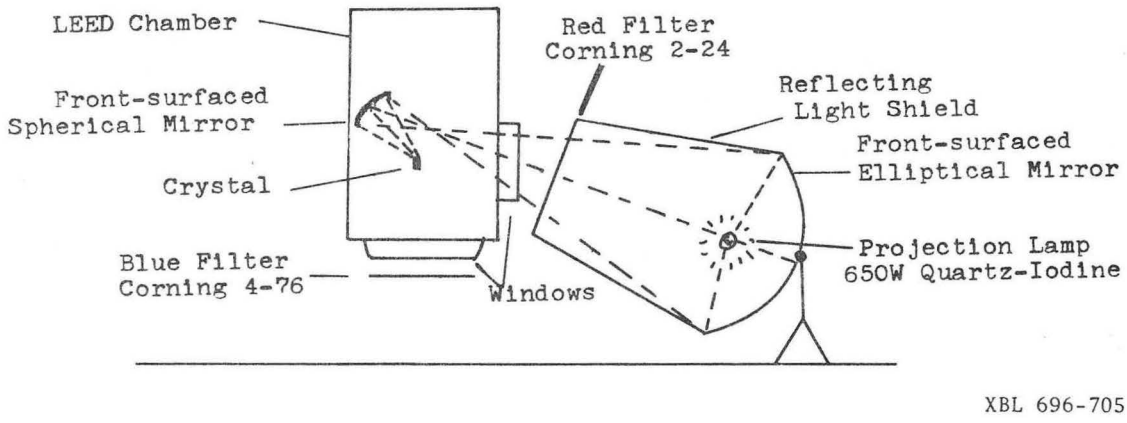

Fig. III-6 Experimental arrangement used for thermal image heating of lead samples during melting experiments.

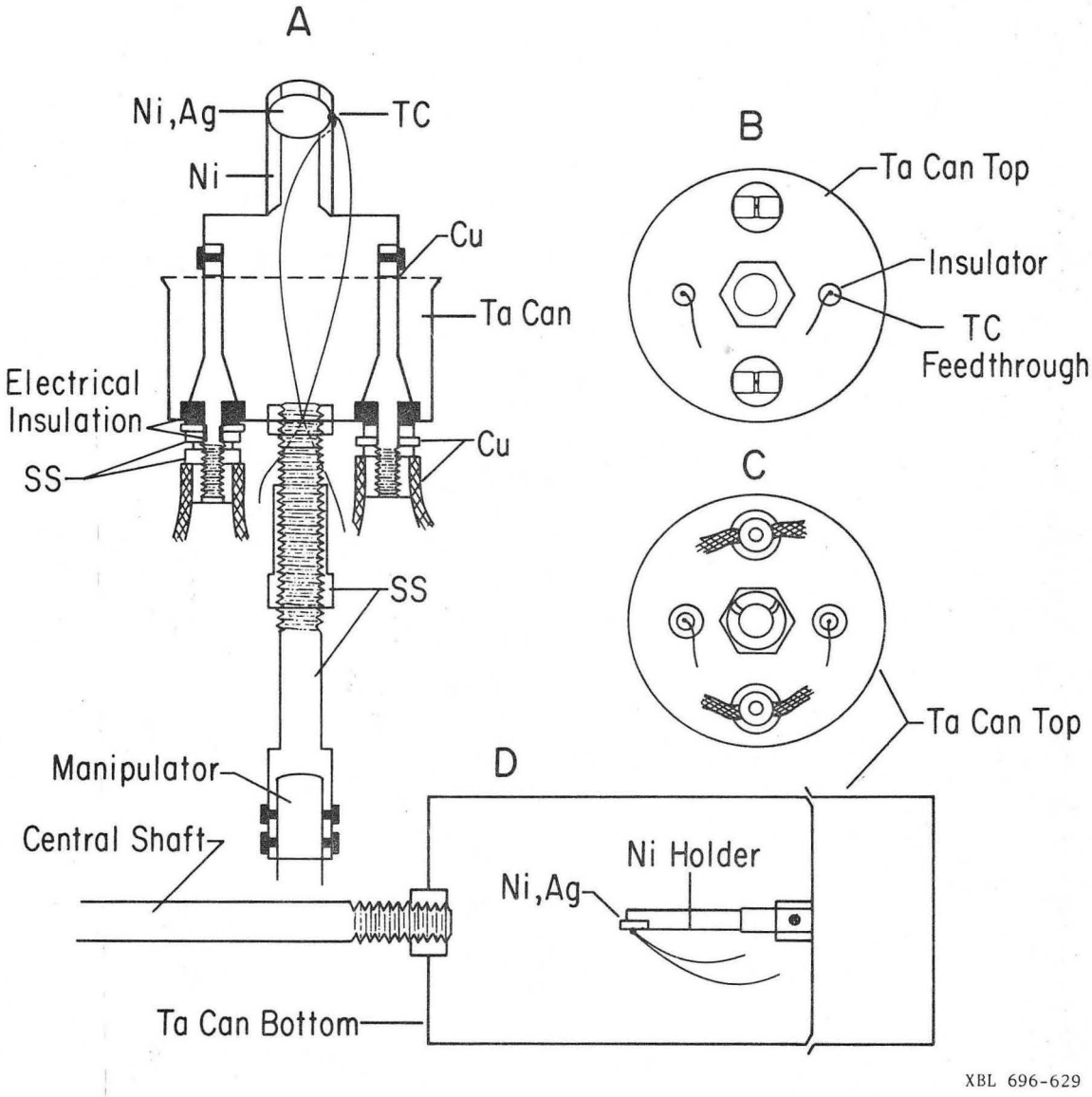

Fig. III-7 Experimental arrangement for the vaporization studies. A: cutaway view of crystal holder and tantalum can top. B and C: bottom and top views, respectively, of tantalum can top. D: side view (partial cutaway) of tantalum cans closed for vaporization of nickel or silver crystals.

TABLE III-II

Bulk impurities in samples (ppm)

Ag(99.995%)*	Au(99.97%)*	Pd(99.0%)*	Ir (99.7%)*
Fe 50	Ag 3000	Au 180	Cr 10
Cr 15	Al 15	Cu 3000	Fe 10
	Cr 30	Fe 150	Mo 20
	Cu 50	Mn 2000	Ru 50
	Fe 400	Ni 20	Si 20
	Mg 120	Pt 5000	Ta 100
	Ni 40	Ru 60	W 3000
	Si 40	Si 10	Rh 20
		Sn 30	
		W 20	
		Rh 100	

Pb(99.99%)**	Bi(99.999%)**	Sn(99.995%)**	Ni(99.997%)**
Cu 10-1000			C 17
Fe 10-1000			Fe 12
Sn 10-1000			
	None reported	None reported	

* Purity obtained by neutron activation analysis of actual crystal samples used.

** Manufacturer's quotation of purity-no independent analysis performed.

polished and etched, the final chemical (or electrochemical) polishing coming immediately before placement of the sample on the crystal holders and the placement of the holder assembly into the diffraction chamber. The chamber was then closed, pumped down, and baked out at 175°-250°C to obtain ultra-high vacuum conditions. As indicated above, the crystals were cleaned in situ by ion bombardment and heating cycles and reproducibly clean, ordered single crystal surface obtained.

2. Crystal Cutting and Polishing (Etching)

Three types of crystals can be distinguished based upon the requisite methods used for cutting and polishing them. These are: (1) very soft crystals such as lead, tin, and bismuth which are readily spark-cut but too soft to be mechanically polished without introducing large-scale bulk damage. (2) Harder metals as palladium, silver, gold, or nickel which are soft enough to be spark-cut but hard enough to be mechanically polished. These materials were usually mechanically polished to smoothness with grit as fine as 1μ diamond paste prior to chemical etching. (3) Very hard, brittle materials as iridium which are best cut with a diamond saw and must be mechanically polished.

In general, spark cutting has been found to be the fastest and most useful tool for cutting and orienting most metal single crystals. For the very soft metals it introduced only limited damage and no contamination from imbedded grit. The surfaces are macroscopically level with large irregularities (> 100μ in diameter). The main disadvantage is the inability to get reproducibly accurate orientation to better than ±2° of desired orientation. For most metals, the mechanical polishing easily corrected such small deviations from the desired orientation.

Table III-III lists the chemical etches used on crystals and holder materials in these studies. In general, the very soft metals developed undulating, but smooth and lustrous surfaces after etching. The other metals etched almost mirror smooth and clean, though the degree of luster was often a function of orientation due to preferential etching of certain faces.

3. In Situ Crystal Cleaning

After the crystal has been placed into the LEED chamber and the system suitably pumped down and baked out all residues from chemical etching solutions, adhering oxides or halides, etc., left on the crystal surfaces from the etching (as well as bulk contaminants) are removed by repeated ion bombardment and heating cycles. Table III-IV lists the minimum heating temperatures and ion bombardment conditions which have been found necessary to obtain reproducibly, clean, ordered single crystal surfaces.

TABLE III-III

Chemical (and electrochemical) etchants

Element	Etchant	Remarks*
1. Lead	2 parts HOA_c (glacial) 1 part H_2O_2(30%)	30-60 seconds, pits all faces equally
2. Tin	STEP ONE: conc. HCl (rinse in H_2O)	10-20 seconds, removes passive layer but leaves coating
	STEP TWO: 1 part HNO_3(conc) 3 parts HOAL(glacial) 5 parts glycerol	20-40 minutes, 40°C, removes coating and gives shiny surface only tried on (110) orientation
NOTE: Several etchants listed in reference books were tried, but gave less consistent results than the above etch. One example is:		
	STEP ONE: 1 part HCl(conc) 3 parts HNO_3(conc) 4 parts H_2O	30-60 seconds, stirring seems to deter results -- must be immediately moved to step two;
	STEP TWO: 1 part HCl(conc) 4 parts H_2O	10-20 seconds (i.e. after bubbling stops)
3. Bismuth	Conc HNO_3	5-15 seconds, must be especially well stirred or it will leave very large pits
4. Nickel (Ex. 1)	22cc H_2SO_4(conc) 12cc H_2O_2(30%) 66cc H_2O	electropolish: 100 ma/cm^2 leaves pits on (100) face but gives very smooth (111) surface
(Ex. 2)	65cc HOA_c(glacial) 35cc HNO_3(conc) 0.5cc HCl(conc)	1-2 minutes; less consistent than electropolish given above
NOTE: For some experiments plating Ni on Copper was used as a crucible material, the process is described below.		

TABLE III-III (Continued)

Element	Etchant	Remarks*
For plating nickel on copper	WATTS BATH: 33.8 g/l boric oxide 45 g/l $NiCl_2 \cdot 6H_2O$ 225 g/l $NiSO_4 \cdot 6H_2O$	50°C, 100ma/cm^2, pH 3.5 inconsistent results due to current gradients
5. Copper	55cc HOAc(glacial) 30cc HNO_3(conc) 15cc H_3PO_4(conc)	20-40 seconds; shines all faces equally
6. Silver	1 part HNO_3(conc) 1 part H_2O	20-40 seconds; shines all faces equally
7. Gold	3 parts HCl(conc) 1 part HNO_3(conc)	20-60 seconds, shines all faces equally
8. Palladium	STEP ONE: 1 part HCl(conc) 5 parts HNO_3(conc) 20 parts H_2O	1-3 minutes, do not stir crystals, must be removed when brown film flows off crystal, do step two immediately
	STEP TWO: 1 part HNO_3(conc) 20 parts H_2O	Secures bright finish, ~5-10 seconds
9. Iron	3 parts HNO_3(conc) 7 parts HF (Conc) 30 parts H_2O	70°C, 1-3 minutes, must not be stirred remove and rinse in H_2O immediately after brown film flows off
10. Tantalum	2 parts HNO_3(conc) 2 parts HF (conc) 5 parts H_2SO_4(conc)	5-10 seconds, must be quickly agitated to prevent large pitting (or even destruction)
11. Molybdenum	STEP ONE: 1 part HNO_3(conc) 1 part H_2O STEP TWO: conc HCl	30-60 seconds, pits
Or	1 part NH_4OH 1 part H_2O_2(30%)	3-5 minutes, pits less- inconsistent in shininess

TABLE III-III (Continued)

Element	Etchant	Remarks*
12. Silicon	STEP ONE: 2cc Cu_2SO_4 1cc HF 100cc H_2O	Decorates Si with copper, 1-2 minutes
	STEP TWO: use Cu polish(No.5)	Removes Cu coating and passive layers, 1-2 minutes
	STEP THREE: 1 part HF(conc) 20 parts HNO_3(conc)	20-40 minutes, produces bright mirror on all faces
13. Iridium	References list boiling aqua regia (No. 7), but I tried only hot aqua regia which did little etching.	

*It is assumed etching is performed: at room temperature, in glass(or polyethylene for HF etches) beakers with gentle stirring; followed by brisk washing in H_2O for several minutes and drying in methanol and blowing with dry N_2. Times indicate those necessary to remove macroscopic (> 100μ) amounts of material.

TABLE III-IV

Minimum heating ion bombardment conditions required to obtain clean, ordered crystal surfaces

Crystal	Heating temperatures	Ion bombardment*
Pb	100°C	.5-2 hours Xe^+ (Ar^+ ineffective)
Sn	100°C°	1-3 hours Ar^+ or Xe^+
Bi	100°C	10-60 min Ar^+ or Xe^+
Ag	500°C	10-30 min Ar^+ or Xe^+
Au	200°-400°C	30-60 min Ar^+ or Xe^+
Pd	500°C†	10-30 min Ar^+ or Xe^+
Ni	800°C	10-30 min Ar^+ or Xe^+
Ir	~1200°C	30-60 min Xe^+ (Ar^+ less effective)

* 1-4 10^{-5} torr gas pressure, 0.5-2μ amp ion current, 140-350 V accelerating potential

† As indicated in section IV a surface structure forms on Pd (100) which has not been definitely characterized as yet.

IV. ORDER-ORDER SURFACE PHASE TRANSFORMATIONS

Experiments on the (100) faces of gold and platinum using LEED indicate the presence of surface structures yielding diffraction patterns not characteristic of a surface layer of the bulk structure.[25,41] Such a surface layer of the bulk structure is designated as a (1×1) surface structure. However, the platinum and gold surfaces transform to Pt(100)-5×1[25] and Au(100)-5×1[41] structures. Assuming these surface structures are characteristic of the clean metal surface, we shall call the phenomena describing such surface reconstruction as order-order surface phase transformations. Table IV-I lists many examples of such order-order surface phase transformations observed on semi-conductor and insulator surfaces. The discovery of these order-order surface phase transformations has sparked much discussion in the literature as to the possible origin of these phenomena. It is my conviction that many of these transformations are indeed characteristic of the clean surface; Section IVA reviews several models which have been proposed to explain the existence of surface phase transformations.

A. Theoretical Models Describing Order-Order Surface Phase Transformations

Recent work published by Jura and Burton[15] indicates that the (100) and (110) surfaces of face-centered cubic crystals could undergo surface structural changes similar to those found in LEED studies if the surface atoms became displaced out of the surface plane. The basic reason for the existence of such displacements is that the extra entropy acquired by the surface due to atoms shifted into these new out-of-plane

Table IV-I. Surface structures found on clean semiconductor or insulator surfaces

Material	Surface Structures Found*	Reference
	Semi-Conductors	
Si	(100) 4×4, (111) 7×7	53
Ge	(100) 4×4, (111) 8×8, (110) 2×2	53
GaAs	(111) 2×2, (110) 1×1, (100) R	53,54,64
GaSb	(111) 2×2, (110) 1×1	53
InAs	(110) 1×1	53
InSb	(100) 2×2, (111) 2×2, (110) 1×1	53
CdTe	(110) 1×1	55
Bi_2Te_3	(0001) 1×1	53
PbS	(100) 1×1	53
PbSe	(100) 1×1	53
PbTe	(100) 1×1	53
C (graphite)	(0001) 1×1	53
α-SiC	(0001) R	56
CdS	(0001) R	64
	Insulators	
LiF	(100) 1×1	53
NaCl	(100) 1×1	58
MgO, ZnO	(100) 1×1, (100) 1×1	53
C (diamond)	(100) 2×2, (111) 2×2	53
α-Al_2O_3	(0001) $\sqrt{31} \times \sqrt{31}$	12
SiO_2 (quartz)	(0001) 1×1	58
Mica (muscovite)	(100) 1×1	53

* Those surfaces not listed have probably not been reported in the literature.

R - Reconstructed, not readily indexed, surfaces.

positions, more than compensates for the slight increase in energy required to transform into the new "buckled" structure. Their quantitative calculations involve the use of a Lennard-Jones 6-12 potential suitable for argon. However, their qualitative conclusions would remain valid even for metals. They conclude that it is possible for the normal (1×1) structure of the Ar(100) surface to transform to a C(2×1) structure below the melting point of the solid. The transformation temperature, however, should be very sensitive to the presence of impurities and vacancies. Thus, it is likely that surface atoms, lacking neighbors above the surface plane, could "relax" into new ordered structures by a periodic displacement of certain surface atoms out of the surface plane. This periodic displacement of atoms outward would give rise to new diffraction features and the displacements could be regarded as order-order surface phase transformations.

Fedak and Gjostein[59] have been quite successful in explaining the properties of the Au(100)-5×1 structure by assuming the top atomic layer is a hexagonal arrangement of atoms on top of the normal (or bulk) Au(100)-1×1 arrangement. The (5×1) diffraction pattern is thus generated by the coincidence of every sixth atom in the close-packed hexagonal over-layer with every fifth atom in the "(100) substrate." Thus, the transformation of the gold and platinum (100) surfaces from a (1×1) → (5×1) can be regarded as an order-order surface phase transformation from face-centered cubic to a close-packed hexagonal surface structure. Rhodin[60] indicates that a possible justification for postulating such a phase transformation is provided by the possibility of a different (and lower) effective valence for gold atoms on a crystal surface. Such a suggestion would be a logical extension of the Hume-Rothery rules[61]

(as expanded by Brewer[62]) from bulk phases to surface phases. In the modification suggested by Brewer, the number of s and p bonding electrons per atom determines the bulk structure, i.e., 1 to 1.5 s and p bonding electrons leads to bcc structure, 1.7-2.1 implies hcp, 2.5-3.0 implies the fcc structure; and about 4 implies the diamond structure. For gold or platinum, therefore, if as postulated, the number of bonding electrons per atom is less than in the bulk, then a transition from a fcc to a hcp structure-at the surface-would be possible. Surveys of other metals indicates that this possible lower valence for surface atoms is exclusive to Au (and possibly Pt) and is not generally possible for most other metallic elements.

One final possible mechanism for surface structural changes is based on the concept of surface strains relieved by surface rearrangements of atoms. Faceting of crystal surfaces may be one manifestation of this effect.[53] It is believed that large thermal gradients may provide sufficient driving force for such surface rearrangements. In addition, mechanical strains often a result of crystal preparation could lead to surface rearrangements and would be very difficult to duplicate and thus could lead to irreproducibility. It should be noted, however, that the ordered surface structures which are listed in Table IV-I have been found to appear reproducibly in many different laboratories.

B. Definition of a Clean Surface

From the previous discussion it can be concluded that some surfaces may undergo surface phase transformations. However, proving that any particular surface structure is a property of the clean crystal surface is a difficult task. The following experimental facts will serve to illustrate some of the difficulties:

1. As reported in Fig. IIC-1,[40] even one-tenth of a monolayer of disordered silicon atoms deposited on a Si(111) substrate, most likely in a very uniform coverage, reduced diffraction intensities significantly.

2. Lawless[63] found that exposure of a copper surface to roughly 10^{-1} torr-sec of oxygen produced large copper oxide "pyramids" visible by electron microscopy, but did not obliterate fully the diffraction spots characteristic of the copper. This is likely the result of the oxide clustering in islands leaving areas of the copper surface free of oxide - hence, still capable of producing a LEED pattern characteristic of a copper surface.

3. In my experiments I found that even 10^{-7} torr-sec exposure of a Ni(111)1x1 surface to ambient gases (see Fig. III-1) occasionally produced perceptible changes in the diffraction pattern, but that even 10^{-3} torr-sec exposure of a Pb(111)-1x1 surface to ambient produced no significant changes in diffraction pattern or intensities, indicating that differences in sticking coefficients of the ambient gases varies tremendously on different metal surfaces. Thus, no definitive experimental criterion for cleanliness is possible. However, if the criteria which are discussed in Section III-A are met, and if the result is reproducible in several laboratories and complementary experimental techniques such as flash desorption using mass spectrometers, Auger spectroscopy, or ellipsometry do not suggest the presence of impurities, then it is assumed the observed surface structure is characteristic of a clean surface. There is one final reservation: impurities below the detection limit of any presently available technique may still act catalytically favoring or inhibiting certain phase transformations though the impurities are not themselves contributing to the new surface structure.

C. Ordered Surface Structures

Surface structures on the (100) surfaces of Ag, Au, Pd, and Pt have been previously reported from this laboratory.[13,31] The technique for investigation of the surfaces has already been described and entails a systematic search for changes in the diffraction pattern as a function of temperature while consistently maintaining "clean" conditions. The following results were obtained.

Au(100)-5×1	in temperature range	200°-400°C
" 6×6	in temperature range	350°-550°C
ring structure	at temperature above	750°C
Ag(100) C(2×2)	in temperature range	600°-750°C
ring structure	at temperature above	750°C
Pd(100)-2×1	in temperature range	200°-300°C
" 2×2	in temperature range	250°-550°C
" C(2×2)	at temperature above	550°C

Since the first reports on these structures,[13] an extensive amount of work has been performed both in this laboratory and other laboratories on the nature of these structures. Extensive work, especially Auger spectroscopy seems to support the Au(100)-5×1 structure as characteristic of the Au(100) surface even at room temperature.[22] On the other hand, the 6×6 structure has not been duplicated in other laboratories. Work reported in Section X indicates that neither the Ag(100)-C(2×2) nor the ring structure are characteristic of the clean, strain-free silver surface. An explanation for the discrepancy in these findings and others will be discussed below. The Pd(100)-2×2 and C(2×2) structures (and

intermediate structures characterized by streaking as in Fig. IIC-5) have been totally reproducible in several laboratories in about the temperature ranges listed above, while the 2×1 structure has not been reproducible. However, Auger spectroscopy, both in this laboratory and others, sheds some doubt on the cleanliness of the Pd surface. As reported in Table III-II, the palladium was impure and possible surface contamination from such bulk impurities is not altogether surprising. The table below lists all of the surface structures found on metal surfaces which are still believed to be characteristic of clean surfaces.

Table IV-II

Au(110)-2×1		
Au(100)-5×1	Room temperature → 500°C	Both completely verified, including Auger spectroscopy
Pt(100)-5×1	Room temperature → 1400°C	
Pd(100)-2×2	250°-550°C	With possible reservations expressed above
Pd(100) C(2×2)	550°C → 850°C	
Bi(11$\bar{2}$0)-2×10	Room temperature → melting point	Found by Jona[64] but not verified in any other laboratory
Sb(11$\bar{2}$0)-6×3	Room temperature → 250°C	

In addition to studies on metals surfaces, semi-conductor and insulator surfaces have been investigated by LEED and several structures have been found on different surfaces. Table IV-I and II lists all surface structures found on semi-conductor, insulator and metal surfaces which are believed to characterize clean surfaces. The number of metal

surfaces studied already includes at least one low index face of the following: Be, Al, Ti, V, Fe, Ni, Cu, Nb, Mo, Rh, Pd, Ag, Sn, Sb, Ta, W, Re, Ir, Pt, Au, Pb, and Bi.

D. Irreproducibility and Surface Structural Changes

Some explanation is in order for the detection of surface structures on "clean" surfaces which have proven to be irreproducible. Two possibilities impress this author as being the most reasonable:

1. As discussed in Section IV-A, minute quantities of impurities may actually retard the surface structural changes - the inability of early experimentalists to discover the Au(100)-5×1 surface structure may have been a result of this effect. Small amounts of carbon, for example, retard the formation of the Pt(100)-5×1 surface structure.[9]

2. Mechanical damage introduced in crystal preparation or holder mounting or thermal effects caused by large thermal gradients in the crystals may lead to surface structural changes previously reported but which were not reproduced in later experiments. For example, the same silver crystal rod used for early studies of surface phase transformations was used in one of the later vaporization studies and thus it is doubtful that bulk impurities were the original cause of the formation of the Ag(100)-C(2×2) structure.

In discussing surface structural changes, it must be emphasized that minute quantities of impurities could affect surface free energies sufficiently to make a previously unstable structure the stable one. Such catalytic effects by impurities is consistent with the model proposed by Jura and Burton[15] and the small amounts necessary would not necessarily be detectable by analytical tools now available.

V. MEAN DISPLACEMENT SURFACE ATOMS

A. Experimental

In Section II-B above the theory describing the thermal effects in LEED was discussed. Experimentally, the procedure for determining the surface Debye temperature is quite simple: at room temperature an intensity scan is made and a maximum in the $I_{00}(eV)$ curve is taken as the reference. The telephotometer is focused on the 00-spot at the voltage corresponding to the maximum intensity. The crystal is heated (e.g. for Pd to about 650°C) and the power is turned off. The telephotometer output signal (monitoring the spot intensity) is plotted as ordinate; the thermocouple reading as abscissa, producing a curve as shown in Fig. V-1. In this way there is no interference from fields caused by the heater current. Generally it takes 1-5 minutes for a crystal to cool to below 100°C. The lower (essentially horizontal) curve in Fig. V-1 is obtained by rotating the 00-spot into the center of the screen and recording the intensity of the "background" at the same voltage as the previous intensity curve. To obtain the effective Debye temperatures, the intensity of the diffraction spot is read off the curve at different temperatures; the background value is subtracted from this value and the $\log_{10}(I_{00}-I_{BKGRD})$ calculated as in Table V-I is plotted vs T(°K) obtained by converting the thermocouple readings using standard thermocouple calibration charts. Figure V-2 is a plot of $\log_{10}(I_{00}-I_{BKGRD})$ vs T obtained from Fig. V-1. Using Eq. IIB(3) and (10), $\log_{10}(I_{00}-I_{BKGRD}) = |F_{hk\ell}|^2 e^{-2W} + f_o^2/4\, e^{-2W}[2WI_0(\Delta\underset{\sim}{k} \pm q)]$ where $2W = KVT\cos^2\phi/M\Theta_D^2$ as in Eq. IIB(6). Table V-II indicates, for different values of "2W" at temperatures corresponding to room temperature = 300°K, what effect

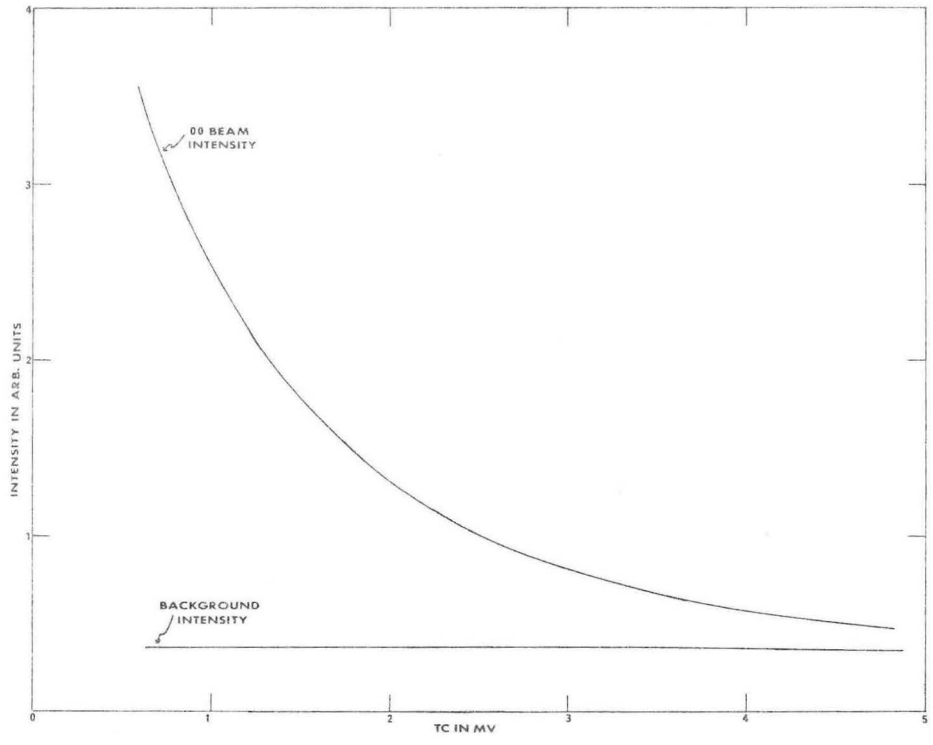

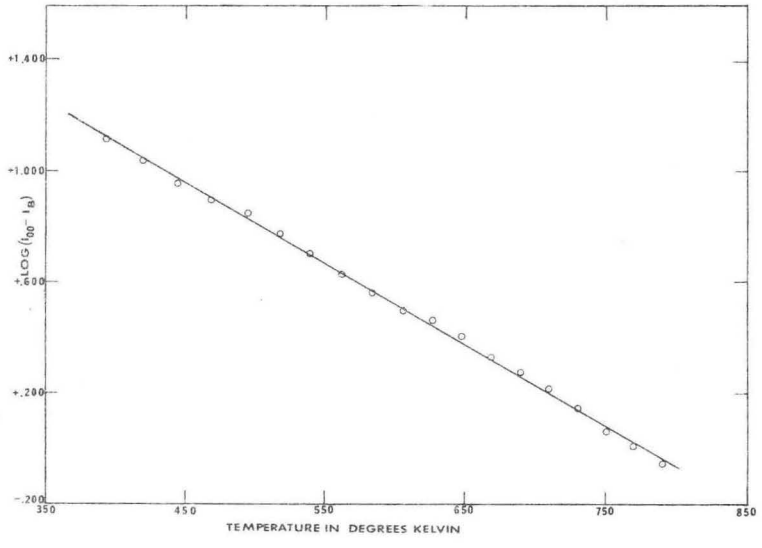

XBL 696-642

Fig. V-1 (Top) Temperature dependence of the intensity of the (00) reflection and background scattering from Pd(100) surface at 315 eV.

Fig. V-2 (Bottom) Derived log $(I_{00}-I_B)$ vs T from Fig. V-1

Table V-I Data from Fig. V-1. Data in last two columns are plotted in Fig. V-2.

Tc (MV)	I_{00}	I_B	$I_{00}^* \equiv I_{00}-I_B$	log I_{00}^*	T(°K)
0.6	17.5	1.8	15.7	1.195	369
0.8	14.8	1.8	13.0	1.114	394
1.0	12.7	1.9	10.8	1.033	420
1.2	10.9	1.9	9.0	0.954	445
1.4	9.7	1.9	7.8	0.892	469
1.6	8.5	1.9	6.6	0.819	492
1.8	7.5	1.9	5.6	0.748	515
2.0	6.6	1.9	4.7	0.672	538
2.2	5.9	1.9	4.0	0.602	560
2.4	5.3	1.9	3.4	0.531	582
2.6	4.8	1.9	2.9	0.462	604
2.8	4.4	1.9	2.5	0.397	626
3.0	4.1	1.8	2.3	0.362	647
3.2	3.8	1.8	2.0	0.301	668
3.4	3.5	1.8	1.7	0.230	689
3.6	3.3	1.8	1.5	0.176	710
3.8	3.1	1.8	1.3	0.114	730
4.0	2.9	1.8	1.1	0.041	751
4.2	2.7	1.8	0.9	-0.046	771
4.4	2.6	1.8	0.8	-0.097	791
4.6	2.5	1.8	0.7	-0.155	811

Table V-II. Effect of Thermal Diffuse Scattering

Total $I = I_{00} + I_{TDS}$, where $I_{00} = e^{-2W} I_0$ = the diffraction intensity in the specular beam, excluding the thermal diffuse scattering. I_0 is the interference function at absolute zero. $I_{TDS} = (2W/4)\, e^{-2W} I_0$ = thermal diffuse scattering according to the approximation of Webb,[36] et al. The table below indicates the effect of the thermal diffuse scattering on the Debye-Waller factor measurements as reported in Tables V-III to V-VI below.

$T(^\circ K)$	I_{00}(units of I_0)	I_{TDS}(units of I_0)	I_{Total}(units of I_0)	$\log_{10} I_{total}$	$\frac{\Delta \log I_{Tot.}}{\Delta T}$	average $\frac{\Delta \log I_T}{\Delta T}$
If at 300°K, 2W = 0.10, then at:						
300	.905	.023	.928	- .033	1.07×10^{-4}	
600	.820	.041	.861	- .065		1.1×10^{-4}
900	.741	.056	.797	- .099	1.13×10^{-4}	
If at 300°K, 2W = 1.00, then at:						
300	0.368	0.092	0.460	- .338	1.18×10^{-3}	
600	0.135	0.068	0.203	- .692	1.20×10^{-3}	1.19×10^{-3}
900	0.050	0.038	0.088	-1.052		
If at 300°K, 2W = 10.0, then at:						
300	4.6×10^{-5}	1.15×10^{-4}	1.61×10^{-4}	-3.79	0.0137	
600	2.1×10^{-9}	1.05×10^{-8}	1.26×10^{-8}	-7.90	0.0139	0.0138
900	1.0×10^{-13}	2.75×10^{-13}	8.5×10^{-13}	-12.07		

the Debye-Waller factor would have on the intensity. The four tables, V-III through V-VI show the experimental values for the slope ($\Delta \log I_T/\Delta T$), obtained from materials studied in the course of this research. Comparing five tables, these conclusions follow:

1. In no experiment was a slope $\Delta \log (I_{00}-I_B)/\Delta T$ smaller than 3.00×10^{-4} found. As shown in Table V-II this corresponds to a maximum error of 2% in θ_D due to the thermal diffuse scattering.

2. Most values for the slope are on the order of 3.00×10^{-3} which would correspond to a maximum error of about 1% in θ_D due to the thermal diffuse scattering.

Thus, as long as the intensity of the diffuse background I_B is taken into account, the effect of thermal diffuse scattering on Debye-Waller experiments is negligible. As discussed in Section IIB several other effects (as, for example, multiple scattering and anharmonicity) could lead to departures from the simple Debye-Waller model. Their effects will be discussed in Section X-B. However, there are several experimental errors which need to be discussed at this point.

In Eq. IIB(6) there are three factors which require experimental measurement, namely the beam voltage, V; sample temperature, T; and angle of incidence, ϕ. The actual beam voltage "seen" by the crystal surface has proven to be a very difficult quantity to establish. Differences in work function between cathode and grid surfaces, inner potential corrections, and the electron energy spread in the emitted incident electron beam contribute to the uncertainty. This uncertainty may be as much as 2-10 eV (lower at lower voltages) according to results obtained from my equipment. However, the uncertainty in the beam voltage, even if it were as large as 10 eV, would only effect the magnitude of $\theta_{D_{EFF}}$

as $(V + \Delta V)^{1/2}$ where ΔV would be the uncertainty. Thus if $\Delta V = 10$, $V = 200$, error in θ_D would be about $(200 \pm 10)^{1/2}$ or 3%, approximately. The difficulty in measurement of temperature is generally due to the following factor: to avoid surface contamination, thermocouples were generally placed on the crystal holders. This can lead to temperature measurement errors of two kinds: 1) temperature offset whereby the thermocouple reads a temperature consistently different from the actual surface temperature; 2) more likely, the thermocouple will read a temperature different from the crystal surface, this difference decreasing as the crystal cools. If only 1) were the case, absolutely no effect would be observed since displacing the linear temperature scale will in no way affect the slope of the $\log_{10} (I_{00}-I_B)$ vs T curve. However, if 2) is the case and the initial temperature difference were large, then appreciable curvature could be introduced into the "Debye-Waller plot." Indeed, especially in the Ir curves, there was appreciable curvature at higher temperatures and the lower temperature portion of the Ir vs T curve was used to obtain the effective Debye temperatures listed in the table. The problem in determining the angle ϕ is not great. Since ϕ is generally near 0° and enters the Debye-Waller formula as $\cos^2\phi$, accuracy is sufficient to give less than 1% error in θ_D easily. The most significant errors in most of my experiments arose from the measurement of the spot intensity. The main difficulty was the instability in the electron optics, recorder, etc. Mostly these instabilities introduced noise on the intensity curves (which caused scatter on the Debye-Waller plots), however, occasionally systematic drifts (as in recorder zero) might go undetected which would introduce large errors and which could show up on the Debye-Waller plots as curvature. It must be emphasized that all these experimental

uncertainties are in addition to those involved with the interpretation discussed in Section IIB.

Despite the experimental difficulties outlined above, a curve as shown in Fig. V-2 was not unique and perhaps half the experimental curves were as straight, though often with more scatter. The slope of the curve was determined and a value of $\theta_{D,EFF}$ for that voltage was determined from the formula

$$\frac{\Delta \log(I_{00}-I_B)}{\Delta T} = \frac{-KV\cos^2\phi}{M\theta^2_{D,EFF}} \qquad VA(1)$$

The same experiment was repeated at different voltages and the results tabulated as in Tables V-III to V-VI. If the values of $\theta_{D,EFF}$ are plotted as a function of electron energy a curve as shown in Fig. V-3 is obtained. As discussed in Section IIB and in publications from this laboratory,[11,25] these curves always show lower value of $\theta_{D,EFF}$ at lower electron energies. The extrapolated value at zero electron volts is taken as $\theta_{D,SURF}$ and the surface mean square displacement can be determined from Eq. IIB(4) as is calculated in Table V-III. The value corresponds to the mean square displacement at 300°K, taken here as room temperature. The rest of this section discusses the results found on four materials; Pd, Pb, Bi, Ir and the interpretation of these results.

B. Results on Palladium, Lead, Bismuth and Iridium

Table V-III and Fig. V-3 summarize the results for the Pd(100) and Pd(111) surfaces. For both surfaces, within experimental uncertainty, $\theta_{D,SURF} = 142°K \pm 15°K$. This leads to a root mean square displacement (normal to the surface) of 0.143Å at T = 300°K. Since the atomic radius in crystalline palladium at 300°K = 1.37Å, this surface mean displacement

Table V-III. Raw data from Debye-Waller plots for palladium surfaces

Pd(100) Surface

Exp. No.	Beam voltage	ϕ, deg	$\frac{\Delta \log (I_{00}/I_B)}{\Delta T}$	$\theta_{D,EFF}$ (°K)	Estimated error (°K)
5	64	5	1.06×10^{-3}	194	± 6
α 1	16	5	4.97×10^{-4}	142	±14
α 2	53	5	1.33×10^{-3}	158	±16
α 4	76	5	1.20×10^{-3}	199	±10
α 5	42	5	8.38×10^{-4}	177	± 9
α 6	146	5	1.88×10^{-3}	220	±11
α 7	232	5	3.07×10^{-3}	218	±22
α 8	320	5	3.56×10^{-3}	237	±18
β 5	234	3	2.50×10^{-3}	242	±10
β 6	315	2.5	2.94×10^{-3}	258	± 5
β 7	15	2.5	3.6×10^{-4}	161	±16
β 7'	459	2.5	3.24×10^{-3}	298	±30

Table V-III (continued)

Pd(111) Surface

Exp. No.	Beam Voltage	ϕ, deg	$\frac{\Delta \log(I_{00}/I_B)}{\Delta T}$	$\theta_{D,EFF}$ (°K)	Estimated error (°K)
3	21	6	6.14×10^{-4}	145	± 7
6	57	6	1.37×10^{-3}	160	± 7
7	98	6	2.76×10^{-3}	148	± 8
8	116	6	2.42×10^{-3}	172	± 9
9	176	6	2.88×10^{-3}	194	±19
10	241	6	2.61×10^{-3}	239	±15
11	331	6	2.80×10^{-3}	270	±27
13	73	6	2.12×10^{-3}	146	± 7
15	240	6	3.08×10^{-3}	220	±10

From Eq. IIB(4): $\langle u^2 \rangle = \frac{3N\hbar^2}{Mk} \frac{T}{\theta_D^2}$; therefore, $\langle u_\perp^2 \rangle_{SURF}^{1/2}$ = 0.143Å at 300°K from Fig. V-3.

Table V-IV. Raw data from Debye-Waller plots for lead surfaces

Exp. No.	Beam voltage	ϕ, deg	$\frac{\Delta \log(I_{00}-I_B)}{\Delta T}$	$\theta_{D,EFF}$ (°K)	Estimated error (°K)
			Pb(111) Surface		
15	15	5	1.24×10^{-3}	61	± 4
17	10	6	1.55×10^{-3}	44	± 3
18	12.5	6	1.12×10^{-3}	59	± 5
19	33.5	6	2.31×10^{-3}	67	± 3
21	40	6	1.98×10^{-3}	79	± 8
23	71	4	3.75×10^{-3}	82	±10
24	71	4	4.11×10^{-3}	77	± 5
From Fig. V-4; $\langle u_{\perp}^2 \rangle_{SURF}^{1/2} = 0.298$Å at 300°K					
			Pb(110) Surface		
1	25	14	3.73×10^{-3}	45	± 2
2	43	14	3.36×10^{-3}	62	± 6
4	36	8	3.93×10^{-3}	54	± 5
5	68	8	3.55×10^{-3}	78	± 8
6	168	8	7.55×10^{-3}	84	± 9
From Fig. V-4; $\langle u_{\perp}^2 \rangle_{SURF}^{1/2} = 0.395$Å at 300°K.					

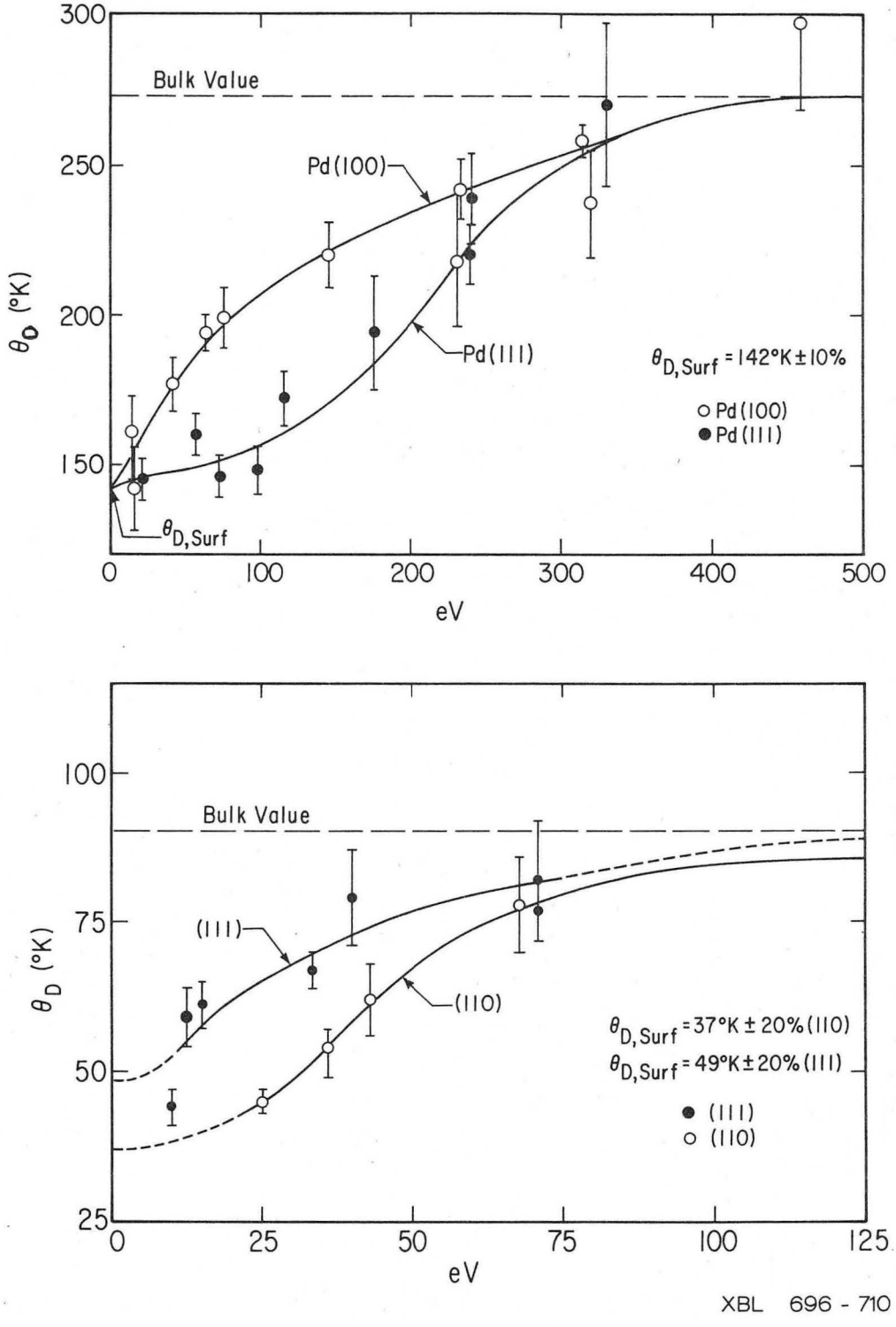

XBL 696 - 710

Fig. V-3 (Top) $\theta_{D,EFF}$ vs eV for palladium surfaces.

Fig. V-4 (Bottom) $\theta_{D,EFF}$ versus eV for lead surfaces.

corresponds to a displacement about 5% of the nearest neighbor distance. At the bulk melting point $\langle u^2 \rangle^{1/2} \sim 0.233$Å for palladium from x-ray Debye-Waller experiments. From Fig. V-3 the shape of the curves for the two surfaces is different. The curve for the (111) surface suggests that the surface value is approached at a higher electron energy indicating less surface penetration of electrons along this direction than along the (100) direction. The denser packing in the (111) plane may account for this effect which was also found for platinum and silver surfaces.[25,33] The values of $\langle u_\perp^2 \rangle_{SURF}^{1/2}$ for palladium follow similar trends as for other fcc metals, i.e., $\langle u_\perp^2 \rangle_{SURF}^{1/2}$ is 1.5 to 2.0 times larger than $\langle u^2 \rangle_{BULK}^{1/2}$.

Table V-IV and Fig. IV-4 summarize the results for the Pb(111) and Pb(110) surfaces. For (111) surface, $\theta_{D,SURF} = 49°K \pm 10°K$ and $\langle u_\perp \rangle_{SURF} = 0.298$Å. For the (110) surface, $\theta_{D,SURF} = 37°K \pm 8°K$ and $\langle u_\perp \rangle_{SURF} = 0.395$Å. Since the atomic radius = 0.175Å, the mean displacement represents 8.5% of the nearest neighbor distance for the (111) surface and 11.3% of nearest neighbor distance for the (110) surface. Interestingly, at the melting point for lead, $\langle u^2 \rangle^{1/2} = 0.177$Å in the bulk from x-ray Debye-Waller measurements. Thus, assuming the Debye-Waller formalism is an accurate representation of the lattice dynamics, surface atoms in lead are vibrating with larger displacement at room temperature than bulk atoms are at the melting point. It should be noted that the data on the (110) surface were obtained using a low temperature holder and recording the diffraction intensity from about 0°C to -100°C. This made it possible to study the Debye-Waller effect at 168 eV where spots are invisible at room temperature for any lead surface. Table V-VII gives the value for the Debye-Waller factor (e^{-2W}) from results obtained in Figs. V-3, V-4, V-5, and V-6. Empirically, when e^{-2W} is smaller than 0.005, the diffraction spot is

Table V-VII. Table of Debye-Waller Factors

	Pd(100)						Pd(111)					
eV	25	50	100	200	400	800	25	50	100	200	400	800
$\theta_{D,EFF}$ (°K)	163	182	207	234	268	274	146	148	157	197	270	274
$\exp_{10}(-2W)$, T=300°K	.67	.52	.37	.21	.091	.010	.60	.37	.17	.11	.094	.010
$\exp_{10}(-2W)$, T=75°K	.90	.85	.78	.67	.55	.32	.88	.78	.64	.57	.55	.32
$\exp_{10}(-2W)$, T=900°K	.30	.14	.049	.0088	*	*	.22	.053	.0051	.0013	*	*

	Pb(110)						Pb(111)					
eV	12.5	25	50	100	200	400	12.5	25	50	100	200	400
$\theta_{D,EFF}$ (°K)	39	45	67	85	90	90	57	65	77	86	90	90
$\exp_{10}(-2W)$, T=300°K	.16	.065	.081	.046	.0042	*	.43	.27	.15	.050	.0042	*
$\exp_{10}(-2W)$, T=75°K	.63	.50	.54	.46	.25	.065	.81	.72	.63	.47	.25	.065
$\exp_{10}(-2W)$, T=600°K	.026	.0042	.0072	.0022	*	*	.18	.073	.023	.0025	*	*

	Bi(01$\bar{1}$2)						Bi(0001)					
eV	12.5	25	50	100	200	400	12.5	25	50	100	200	400
$\theta_{D,EFF}$ (°K)	49	53	66	99	117	117	57	65	79	107	117	117
$\exp_{10}(-2W)$, T=300°K	.32	.14	.080	.11	.040	.0016	.43	.27	.17	.15	.040	.0016
$\exp_{10}(-2W)$, T=75°K	.75	.61	.53	.57	.45	.20	.81	.72	.64	.62	.45	.20
$\exp_{10}(-2W)$, T=600°K†	.10	.020	.0064	.011	.0016	*	.18	.074	.028	.021	.0016	*

Table V-VII (continued)

	Ir(100)					
eV	25	50	100	200	400	800
$\theta_{D,EFF}$ (°K)	178	180	190	220	270	270
$\exp_{10}(-2W)$, T=300°K	.83	.69	.52	.38	.27	.073
$\exp_{10}(-2W)$, T=75°K	.95	.91	.85	.79	.72	.52
$\exp_{10}(-2W)$, T=900°K	.57	.33	.14	.056	.020	*

† Bismuth melts at 544.5 K; the figures in this row represent values it would if it were still solid.

* Values for which $\exp_{10}(-2W) < .001$, totally invisible in LEED.

impossible to see and if e^{-2W} is about 0.02, the spot is visible, but too dim to measure quantitatively. For Pb(111) at room temperature, therefore, no pattern above about 150 eV is visible. What is especially striking about the results on lead, is that even at about 75 eV, the effective θ_D measured is very close to the bulk value. This result contradicts those discussed above for Pd, Pt, and Ag and suggests the surface potential for lead, even on the densely-packed (111)-surface, is extremely "soft" relative to the other fcc metals studied so that electron penetration is high even at relatively low energies.

Table V-V and Fig. V-5 summarizes the results on the Bi(0001) and $(01\bar{1}2)$ faces. As is discussed in Section VII,[64] the bismuth lattice can be approximated as a simple cubic lattice whereby the (0001) face can be designated as the pseudo-cubic (111) face and the $(01\bar{1}2)$ face as the pseudo-cubic (100) face. The results are $\theta_{D,SURF} = 48°K$ for both surfaces and $\langle u_\perp^2 \rangle_{SURF}^{1/2} = 0.302\text{Å}$. Because of the rhombahedral crystal structure, assigning an atomic radius is difficult, however, a value of 1.70Å, is widely accepted. This root mean square displacement represents 8.9% of the nearest neighbor distance at T = 300°K. At the melting point, $\langle u^2 \rangle_{BULK}^{1/2} = 0.092\text{Å}$, so that surface atoms in bismuth are vibrating with a mean displacement normal to the surface at room temperature much larger than that of bulk atoms at the melting point. The θ_D (eV) curves for bismuth are similar to lead, except the bulk value is not approached until slightly higher electron energies. On Fig. V-5 there are three curves; two of the curves are from the same (0001) surface, one at $\phi \sim 4\text{-}1/2°$, the other at $\phi \sim 22°$. The general trend is for the curve for $\phi \sim 22°$, to lie below that at 4-1/2°. Excluding the possible experimental errors discussed in Section 1 above, this is not unreasonable.

Table V-V. Raw data from Debye-Waller plots for bismuth surfaces

Exp. No.	Beam voltage	ϕ, deg.	$\frac{\Delta \log(I_{00}-I_B)}{\Delta T}$	$\theta_{D,EFF}$ (°K)	Estimated error (°K)
Bi(0001) Surface					
1	109	4.5	3.72×10^{-3}	105	±10
2	86	4.5	1.94×10^{-3}	128	±18
3	48	4.5	3.38×10^{-3}	73	± 3
4	33	4.5	2.50×10^{-3}	70	± 3
5	17.5	4.5	1.69×10^{-3}	62	± 2
7	81	22	4.68×10^{-3}	75	± 3
8	44	22	5.24×10^{-3}	52	± 5
9	27	22	2.36×10^{-3}	61	± 6
10	11.5	22	2.30×10^{-3}	40	± 4
Bi(01$\bar{1}$2) Surface					
1	19	6	2.54×10^{-3}	53	± 3
2	46	6	3.97×10^{-3}	66	± 4
3	74	6	3.83×10^{-3}	85	± 5
4	78	6	7.04×10^{-3}	78	±12
1a	25	5	$\sim 3.7\times10^{-3}$	51	±10
2a	44	5	4.7×10^{-3}	60	± 6

From Fig. V-5, $\langle u_{\perp}^2 \rangle_{SURF}^{1/2} = 0.302$Å at 300°K.

Table V-VI. Raw data from Debye-Waller plots for iridium (100) surface

Exp. No.	Beam voltage	ϕ, deg.	$\frac{\Delta \log(I_{00}-I_B)}{\Delta T}$	$\theta_{D,EFF}$ (°K)	Estimated error (°K)
1	481	4	2.10×10^{-3}	281	± 20
2	389	4	1.98×10^{-3}	260	± 10
3	360	4	1.57×10^{-3}	281	± 30
4	333	4	1.64×10^{-3}	264	± 25
5	276	4	1.65×10^{-3}	238	± 25
6	227	4	1.27×10^{-3}	248	± 25
7	176	4	1.05×10^{-3}	240	± 30
8	150	4	1.14×10^{-3}	213	± 20
9	131	4	1.03×10^{-3}	210	± 20
10	95	4	8.65×10^{-4}	195	± 20
11	73	4	5.05×10^{-4}	223	± 30
12	41	4	3.00×10^{-4}	216	± 25
1a	465	11	1.89×10^{-3}	286	± 35
2a	391	11	1.98×10^{-3}	257	± 25
3a	350	11	1.80×10^{-3}	254	± 25
4a	265	11	1.89×10^{-3}	216	± 25
5a	226	11	1.29×10^{-3}	242	± 35
6a	177	11	1.29×10^{-3}	214	± 20
7a	140	11	9.60×10^{-4}	220	± 30
8a	107	11	1.28×10^{-3}	167	± 35
9a	72	11	7.01×10^{-3}	185	± 25
10a	48	11	7.95×10^{-4}	142	± 15

From Fig. V-6:

$$\langle u_{\perp}^2 \rangle^{1/2} = 0.086\text{Å at } 300\text{°K}$$

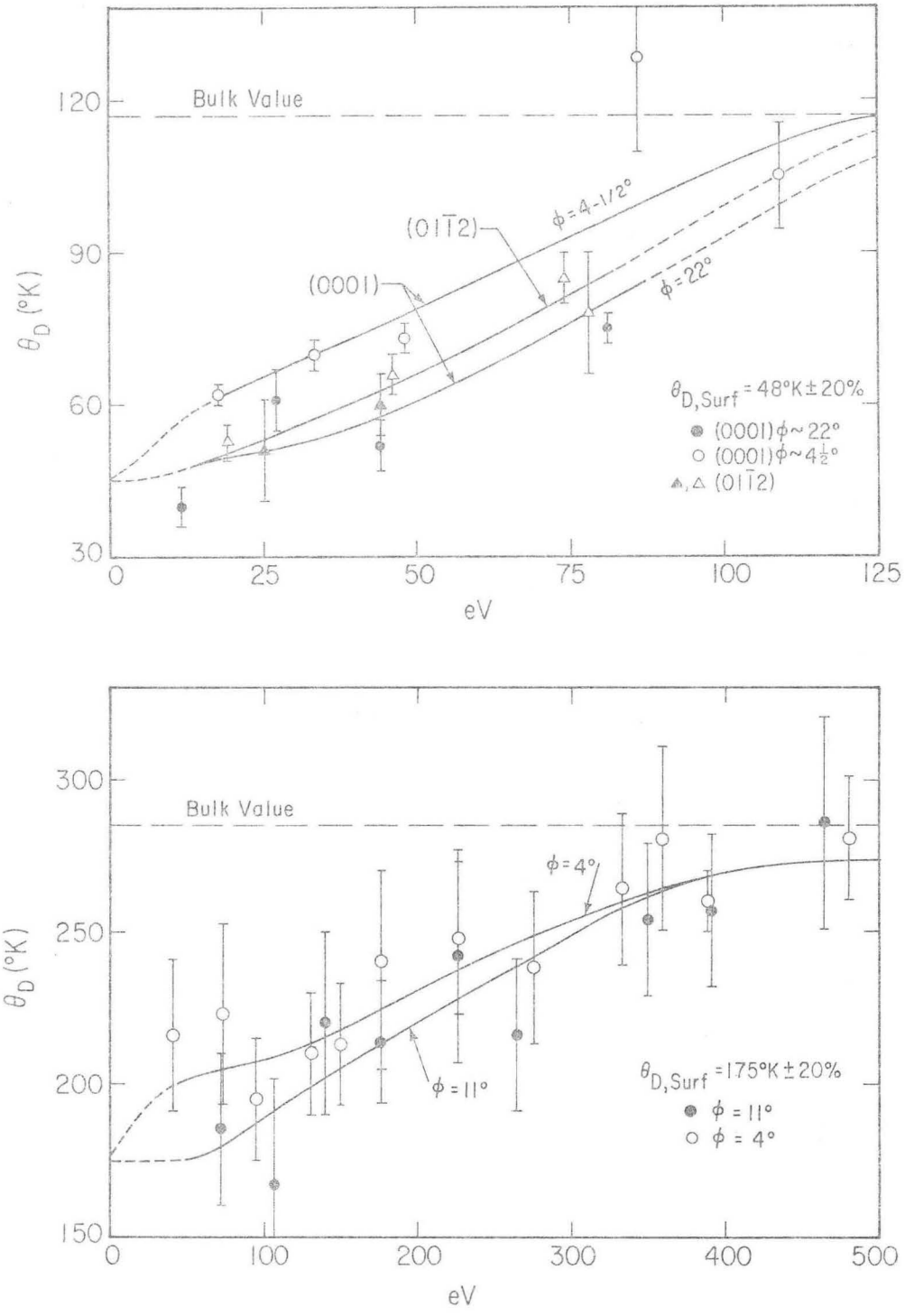

XBL 696-711

Fig. V-7 (Top) $\theta_{D,EFF}$ versus eV for bismuth surfaces.

Fig. V-8 (Bottom) $\theta_{D,EFF}$ versus eV for iridium (100) surfaces.

For, as the impinging electron beam shifts more and more towards grazing incidence, the electrons should penetrate less than at normal incidence. As a result, for any moderate electron energy, a value closer to the surface value will be obtained for grazing incidence than near normal incidence. Finally, of note are the two solid triangular points on Fig. V-5. These were obtained from measurements of diffraction intensity from the melting point down to about 100°C. First, within experimental error, they lie on the θ_D (eV) curve deduced from other measurements. Second, the log $(I_{00}-I_B)$ vs T curve did show some curvature at the highest temperatures suggesting that at the highest temperatures (near Tm) the surface atoms could vibrate with larger amplitude perhaps due to large surface vacancy concentrations.

Table V-VI and Fig. V-6 summarize the results on the Ir(100) face. The results are $\theta_{D,SURF} = 175°K \pm 35°K$ and $\langle u_\perp^2 \rangle^{1/2}_{SURF} = 0.086\text{Å}$. The atomic radius is 1.38Å, so mean displacement is only 3.1% of the nearest-neighbor distance. At the melting point, $\langle u^2 \rangle^{1/2}_{BULK} = 0.238\text{Å}$. Two curves are plotted in Fig. V-6, however, the scatter in the data makes it difficult to decide if there is indeed a difference between them. As indicated in Section III, no suitable etch was found for the Ir(100).

C. Mean Displacement of Atoms Parallel to Crystal Surface

Figure V-7 represents the general LEED situation useful for calculating the Debye-Waller factor for the parallel component of the mean displacement of surface atoms. From Fig. V-7 we obtain that:

$$|\Delta k'|^2 = 4|\underset{\sim}{k}_0|^2 \cos^2(\theta-\phi) = |\Delta \underset{\sim}{k}'_{\perp}|^2 + |\Delta \underset{\sim}{k}_{\parallel}|^2 \qquad \text{VB(1)}$$

where $|\Delta \underset{\sim}{k}'_{\perp}| = |\Delta \underset{\sim}{k}'| \cos\theta$ and $|\Delta \underset{\sim}{k}_{\parallel}| = |\Delta \underset{\sim}{k}'| \sin\theta$. For any isotropic surface [i.e. (100) or (111), but not (110) for fcc crystals] we can write

$$\langle u^2 \rangle_{SURF} = \langle u_{\parallel}^2 \rangle_{SURF} + \langle u_{\perp}^2 \rangle_{SURF} \qquad \text{VB(2)}$$

which can be substituted into IIB(5) to give:

$$\exp -|\Delta \underset{\sim}{k}'|^2 \langle u^2 \rangle = \exp -\left[|\Delta \underset{\sim}{k}'_{\perp}|^2 \langle u_{\perp}^2 \rangle + |\Delta \underset{\sim}{k}'_{\parallel}|^2 \langle u_{\parallel}^2 \rangle \right] \qquad \text{VB(3)}$$

for the Debye-Waller factor. Substituting Eq. VB(1) into VB(3) and letting $\underset{\sim}{k}_0 = 2\pi/\lambda$ gives:

$$\exp[-2W'] = \exp -\left[4\left(\frac{2\pi}{\lambda}\right)^2 \cos^2(\theta-\phi) \cos^2\theta \langle u_{\perp}^2 \rangle + 4\left(\frac{2\pi}{\lambda}\right)^2 \cos^2(\theta-\phi) \sin^2\theta \langle u_{\parallel}^2 \rangle \right] \qquad \text{VB(4)}$$

simplifying,

$$\exp[-2W'] = \exp -\left\{ \frac{16\pi^2 \cos^2(\theta-\phi)}{\lambda^2} \left[\langle u_{\perp}^2 \rangle \cos^2\theta + \langle u_{\parallel}^2 \rangle \sin^2\theta \right] \right\} \qquad \text{VB(5)}$$

Using IIB(4) and changing to LEED variables as in IIB(6), (5) becomes

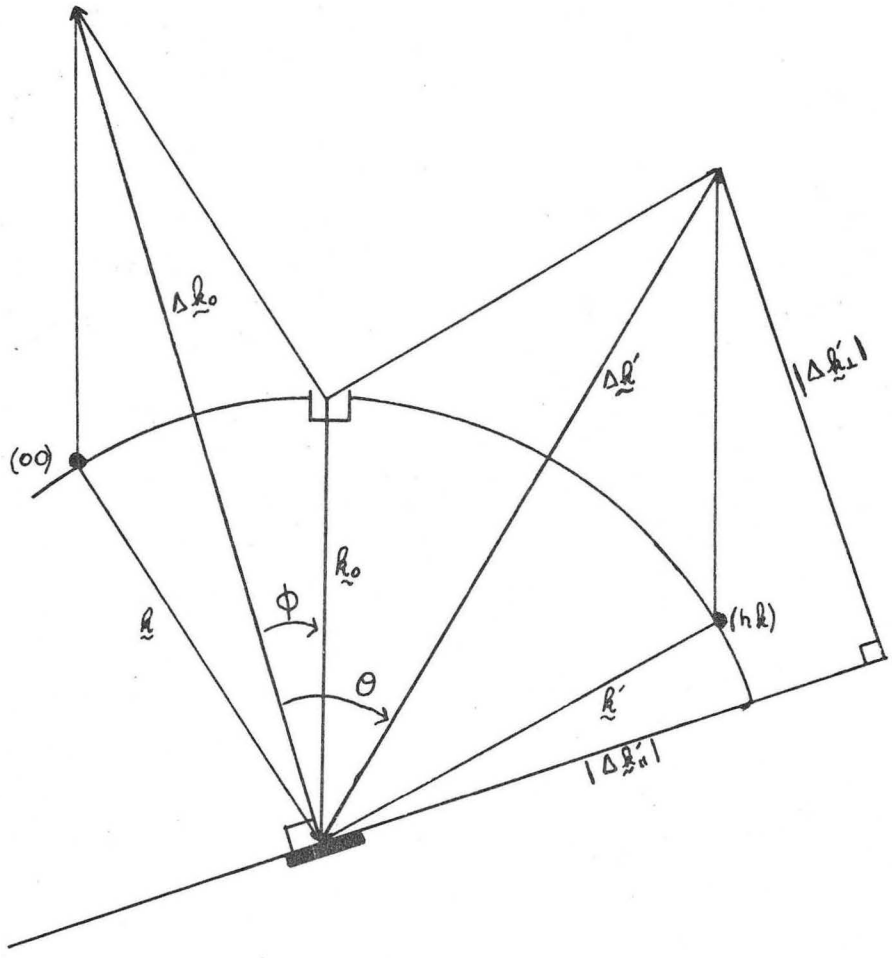

$$|\Delta k'|^2 = |k_o|^2 + |k_o|^2 - 2\, k_o \cdot k_o = 2|k_o|^2 - 2|k_o|^2 \cos[\pi - 2(\theta-\phi)]$$

$$|\Delta k'|^2 = 2|k_o|^2 \left[1 - \cos\{\pi - 2(\theta-\phi)\}\right]$$

$$|\Delta k'|^2 = 2|k_o|^2 \left[1 + \cos 2(\theta-\phi)\right] = 2|k_o|^2 \left[1 + 2\cos^2(\theta-\phi) - 1\right]$$

$$|\Delta k'|^2 = 4|k_o|^2 \cos^2(\theta-\phi)$$

XBL 696-701

Fig. V-7 Determination of scattering vectors for non-specular (h k) and specular (00) diffraction beams.

$$\exp_{10}[-2W'] = \exp_{10}\left\{-KVT\cos^2(\theta-\phi)\left[\frac{\cos^2\theta}{\theta^2_{D\perp}} + \frac{\sin^2\theta}{\theta^2_{D\parallel}}\right]\right\} \quad \text{VB(6)}$$

where K is the same constant as in IIB(6) and $\theta_{D\perp}$ is the effective Debye temperature describing thermal motions normal to the surface; $\theta_{D\parallel}$ is the effective Debye temperature for thermal motions in the plane of the surface. $\theta_{D\perp}$ is the quantity determined from the previously described measurements on the specular reflection. The extension to non-isotropic surfaces would require the definition of an aximuthal angle and the splitting of $\langle u_{\parallel} \rangle$ into components along the main surface coordinates. This will not be discussed here in that no experiments were conducted on nonisotropic surfaces.

The most obvious characteristic to observe about VB(6) is that $\theta_{D\parallel}$ can only be determined by the difference in two experimental determinations of $\log_{10}(I_{hk})$ vs T. Further, since in conventional back-reflection LEED systems, ϕ cannot exceed 24° or θ exceed 48°, the two experimental slopes $\left(\frac{\Delta \log I_{hk} - I_B}{\Delta T}\right)$ will be of comparable magnitude. In practice it has been found that an uncertainty in either experimental determination of slope propagates in determining a value for $\theta_{D\parallel}$ about ten-fold, so that an uncertainty in $\theta_{D\perp}$ of 5% produces a 50% uncertainty in $\theta_{D\parallel}$ making extrapolations of $\theta_{D\parallel}$ (eV) curves virtually impossible. As a result, no information on these measurements (performed on Pd(100) and Bi(0001) surfaces) is presented except to state that results suggest the parallel component is of about the same magnitude as the normal component, though the uncertainty in the determinations was generally about ±25%.

D. Correlation of Surface Mean Displacements to Premelting at the Surface

In discussing the results on lead and bismuth surfaces, it has been indicated that the mean displacement of the surface atoms normal to the surface was significantly larger at room temperature than the mean displacements of bulk atoms at the bulk melting point. Using the Lindemann model described in Appendix C, one would expect a correlation to exist between the mean displacement of atoms and the melting transition, i.e., when the mean displacement is of sufficient magnitude the solid melts. Assuming the applicability of this model to surface states, then the surfaces of lead the bismuth might be expected to premelt. Experiments to test this expectation were performed on lead and bismuth surfaces. Results and discussion of these experiments are discussed in Section VI.

VI. THE NATURE OF MELTING AND STUDIES OF POSSIBLE SURFACE PRE-MELTING

A. General Considerations[65]

Melting is a first order transition between the solid and liquid states. Thermodynamically, melting occurs at a temperature, T_m = melting point, such that the free energy of the liquid phase is less than that of the solid phase. Any theory of melting should present a plausible model for liquids which is also in agreement with the following key experimental results: 1) liquids have short range order; solids have long range order, 2) liquid metals have resistivities, thermal conductivities, and densities of about the same magnitude as solids at the melting point, 3) liquids possess relatively no resistance to low frequency shearing forces compared to the large resistance to shearing exhibited by solids. Further, a melting theory should lead to a reasonable explanation for the observed results of experiments on the kinetics of melting which indicate different melting rates along different crystallographic directions. Lastly, the ease of nucleation of the liquid phase must be contrasted with the difficulty of nucleating the solid phase (i.e., why super-heating of solids is very difficult, while undercooling liquids is routinely performed). Appendix C contains several theories of melting which have been proposed; it is not a complete list of all possible theories but is taken as suitably representative of all theories proposed to this time.

B. Experimental Technique

The experimental arrangement was identical to that shown in Figs. III-4, III-5, and III-6. In about one-half of the studies on lead the crystals were heated resistively to about 260°C and heated from there to the melting point (327°C) and above by thermal imaging. In this way the surface could be made the hottest part of the crystal. In all the other studies the crystal was heated only resistively. However, by changing the placement of the heater leads on the crucibles in different experiments, either the sides or the bottom of the crystals could be made the hottest region. All the samples used were cylinders 6 mm in diameter and 4 to 8 mm in height except for two larger lead samples which were 2 cm in diameter and 4 mm in height. As indicated in Fig. III-4 the crystals were maintained in metal "crucibles" (in high purity iron for Bi and Pb; and in high purity silicon and molybdenum for Sn). The crucibles were machined to fit each crystal to a tolerance of about .002 in. for crucible i.d. The crystals were prepared and mounted as described earlier and placed in the LEED chamber where the procedure described in Section III-B was used to produce sharp, clean diffraction patterns. Leaving the optics on and focusing the electron beam on a well-ordered crystal site at a voltage corresponding to a low eV diffraction maxima [generally in the first order (or 10) beams], the heating was started (temperature and pressure continuously monitored as depicted in Fig. VI-1) and continued until the temperature record indicated that the entire crystal had melted. Visual observation of the diffraction pattern during melting proved to be the most reliable method of observation. The results of these visual observations recorded in the notebook during the experiments

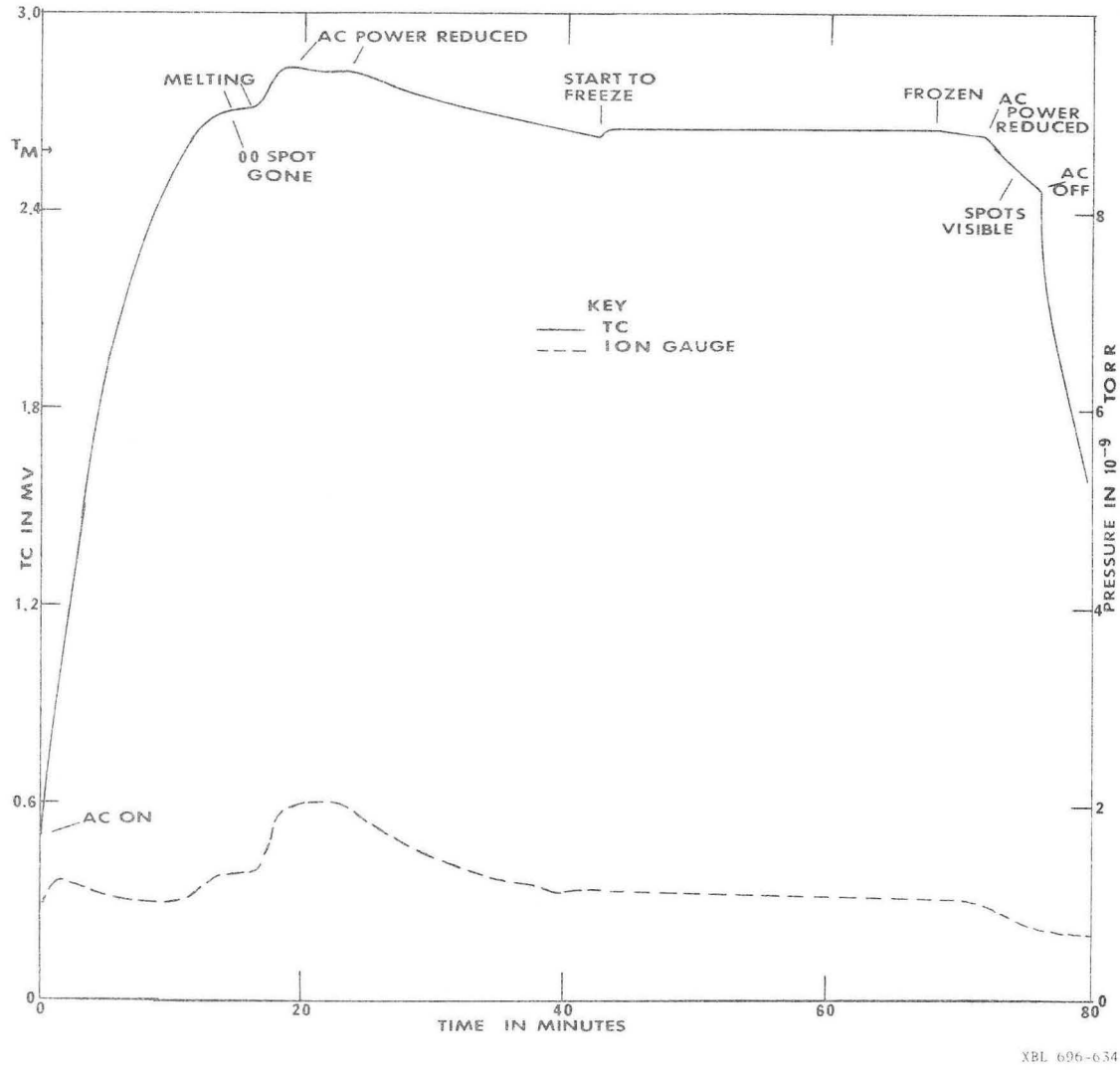

Fig. VI-1 Temperature (solid curve) and chamber pressure (dashed curve) vs time for melting run on lead. AC refers to line power used to heat sample (actual current through sample is DC).

are recounted in Section VI-C below. The heating rate was varied and likewise the cooling rate of the melt (and recrystallization) were varied while continuously observing the diffraction pattern. The diffraction results on the molten metal surfaces and the recrystallized solid surfaces are reported in Sections VII and VIII below;in this section the results concerning possible pre-melting are described.

The materials used in these experiments had to fit several criteria: 1. Must be available in ultra-high purity single-crystal form. 2. Have vapor pressures at the melting point below 10^{-8} torr. 3. Have melting points between room temperature and about 600°C. Lead was the most extensively studied material because its fcc crystal structure made indexing of recrystallized patterns and correlations with theoretical predictions fairly easy.

C. Theoretical Predictions of Surface Pre-Melting

The purpose of these studies was to determine if surfaces would pre-melt, i.e. if the diffraction pattern from a crystal surface would disappear prior to the melting of the bulk. This was my working definition of surface pre-melting. The results of the Debye-Waller measurements suggest that surfaces may be expected to disorder below the melting point, if the Lindemann model[66] were correct. On a different basis, Frank[67] postulated that the (100) and (111) surfaces of fcc metals should not surface pre-melt (indeed, he predicts these surfaces should remain free of equilibrium kinks and ledges up to the melting point), but that the (110) and other "open faces" should experience a surface roughening at temperatures well below the melting point. For the (110) surface he predicts surface roughening above Tm/2. This surface roughening ("pre-

melting of the second order bond," to use Frank's words) should be manifest in LEED either by linear disorder diffraction patterns or by the creation of extra facets giving rise to extra diffraction spots. Stranski's[68] model would indicate a similar expectation, namely, that the (100) and (111) surfaces of fcc crystals belong to the equilibrium form and are not wetted completely by their melts, but that the (100) being a "high-index" face wetted by the melt might pre-melt. Experiments on the three low-index faces (100, 111, 110) of lead can be used to test these predictions; the results reported below support none of these predictions. Experiments on Sn and Bi were begun to test the validity of our findings on lead for non-cubic systems. Indeed, the experiments on vaporized surfaces (reported in Section IX) were performed to see if the low vapor pressure at the melting point of Pb, Bi, Sn metals might influence their surface melting behavior. Where any definite conclusion could be reached, the results all support the view that no pre-melting occurs on the metal surfaces.

D. Results on Lead, Bismuth, and Tin

Lead was the metal most extensively studied. A total of five crystals gave reproducible results described in this section. In addition, because of the ability to regrow the crystals in situ, i.e. to regrow crystals after melting in the LEED chamber, the total number of experimental observations of surface melting was more than thirty, including at least three runs on each low index face of lead. Eight experiments using thermal imaging led to the following results as depicted, for example, in Fig. VI-1 and Fig. VI-2. The temperature monitored by the thermocouple increased during heating until a value corresponding to the bulk melting point of lead (327°C) was reached at which point the temperature curve

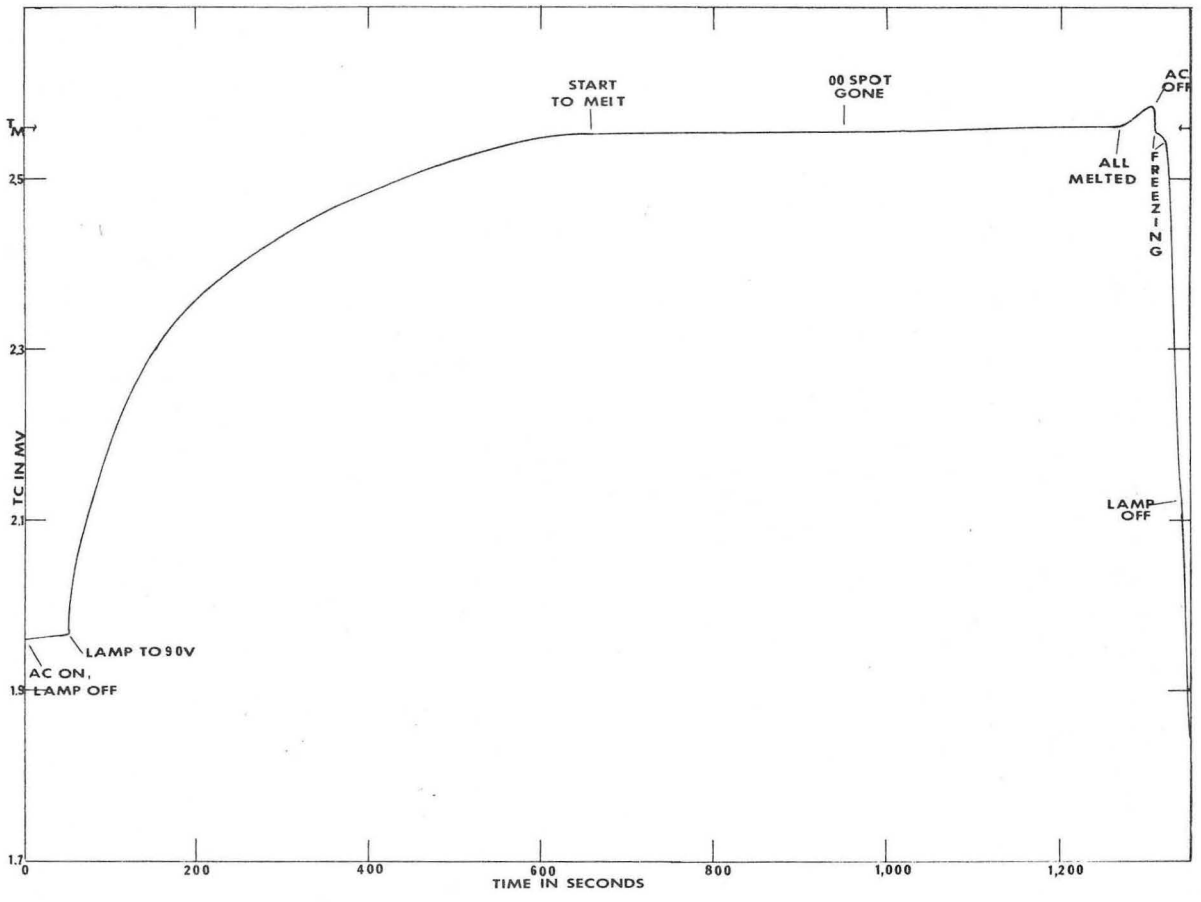

XBL 696-648

Fig. VI-2 Temperature vs time record for melting run on lead. AC refers to line power used to heat sample (actual current through sample is DC); lamp refers to thermal imaging lamp.

remained at this constant value until the sample was completely melted at which time the temperature increased. The thermocouple calibration was generally within ±1°C and the range of temperature during melting was usually less than 1°C. In all experiments the diffraction spots characteristic of the solid surface were visible until the bulk melting point was reached; the spots disappeared suddenly during the period that the temperature curve was constant. The exact time for the disappearance of the spots was a function of the thermal gradients, i.e., when the surface was directly heated the spots wouldd disappear right after the thermocouple began to register the bulk melting temperature, however, when the sides of the crystal were heated most directly, then the diffraction spots would stay visible until just before the thermocouple reading began to increase above that corresponding to the bulk melting point. The large disc-shaped crystals were only heated resistively. However, in these experiments the results were consistent; in fact, because of the size of the crystal, the propagation of the liquid front along the crystal surface could be easily observed visually during the course of the experiment. The results showed that the (110) surface melted at the bulk melting point. Very good crystalline regions of (100) and (111)-oriented crystallites formed upon recrystallization of the molten lead (see Section IX) and thus the lack of pre-melting was observed for all three low-index orientations on the same crystal. Figures VI-3,4,5 show photos of diffraction patterns obtained for all three orientations from one sample. In order to increase the information on the liquid surface and to recheck the results on the (110) orientation, several more samples were investigated, including a study using a low-temperature holder. As regards pre-melting, no result found has ever contradicted the finding that the (111), (100) or (110)

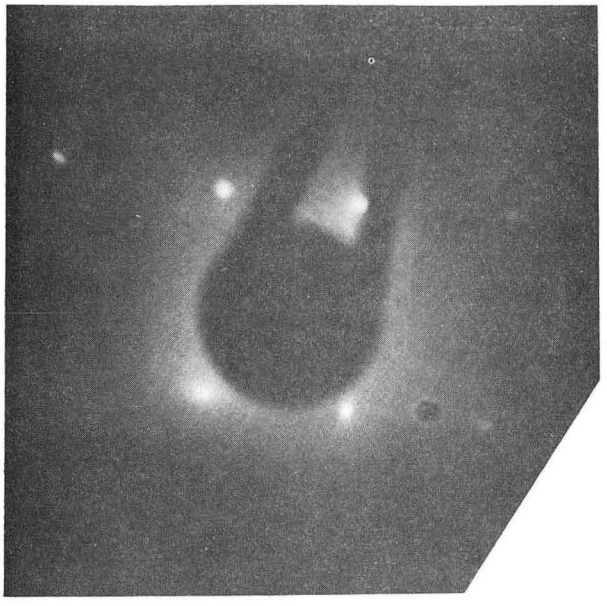

XBB 695-3222

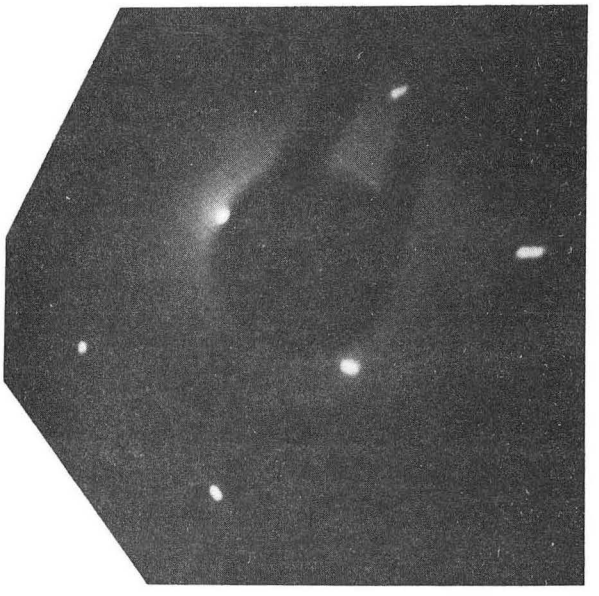

XBB 695-3221

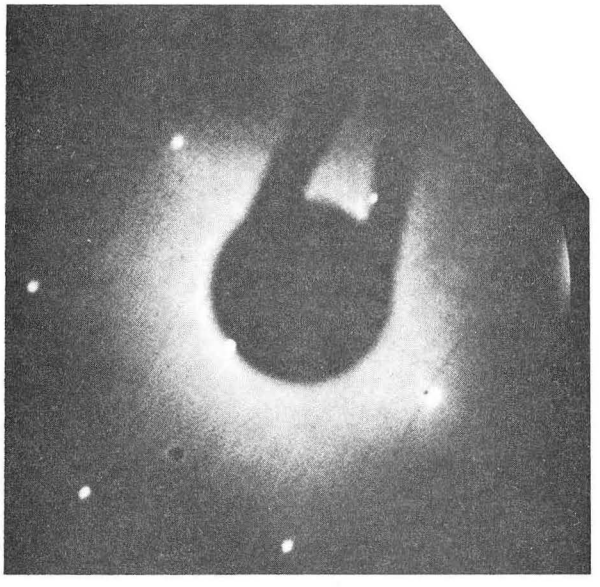

XBB 695-3223

Fig. VI-3 (Top) LEED pattern from Pb(110)-1×1 surface at 48 eV.

Fig. VI-4 (Middle) LEED pattern from recrystallized Pb(100)-1×1 surface at 53 eV.

Fig. VI-5 (Bottom) LEED pattern from recrystallized Pb(111)-1×1 surface at 64 eV.

surfaces do not lose their ordered structure, i.e. within the definition in Section VI-C above.

The bismuth studies were performed exactly as described in Section III using resistance heating. Two crystals were used in these studies with a total of ten experimental runs. Similar to lead, it was possible to regrow two different orientations of bismuth and thus allowing a check on the possible pre-melting for these two orientations. Bismuth has a rather complex rhombic structure, however, as pointed out by Jona,[64] the structure fits quite closely to a distorted simple cubic lattice. The results are for either the pseudocubic (111) [rhombic (0001)] face or the pseudocubic (100) [rhombic $(01\bar{1}2)$]. There is no surface pre-melting, the diffraction spots were quite visible right to the bulk melting point and, in fact, because in one study heating was from below, the solid surface could be seen "floating" on the denser liquid beneath and the spots on the screen moved accordingly. It should be added that both these faces displayed excellent diffraction features and could be very easily cleaned. They were also unreactive towards ambient gases in complete agreement with the observations of Jona. That fact that bismuth expands on freezing (while lead contracts) did not seem to influence its melting characteristics.

The melting experiments on tin gave much more ambiguous results than the studies of surface melting on Pb or Bi because of a problem in obtaining a clean, ordered surface. The only surface studied was the (110) orientation which proved to be quite reactive to ambient contamination in the chamber and formed a contaminant surface structure. These structures disordered on heating giving a very dim diffraction pattern. Most of the experiments on Sn were performed in silicon crucibles; the Si is soluble in liquid Sn to a small extent while Si is insoluble in solid Sn.

However, after repeated melting runs the silicon appeared to precipitate on the Sn surface giving a fairly good Si(100) diffraction pattern. Work using the arrangement described in Section III and a Mo crucible were, however, more successful giving the following results: diffraction spots were visible definitely only to about 6°-8°C below the melting point. Recrystallized surfaces (at least four different faces were observed, none of which could be readily indexed with the very complex tetragonal white tin structure) gave diffraction patterns which were observed to the bulk melting point. Figure VI-6 gives an example of a record of one such melting run.

To summarize these results: Pt(110), Pb(111), Pb(100), Bi(0001), Bi(01$\bar{1}$2) surfaces do not premelt; i.e. their melting coincides with the bulk melting point. In addition several recrystallized, but unindexed Sn faces do not show premelting. However, certain problems of contamination of the Sn(110) surfaces prevent unequivocal determination of its premelting behavior.

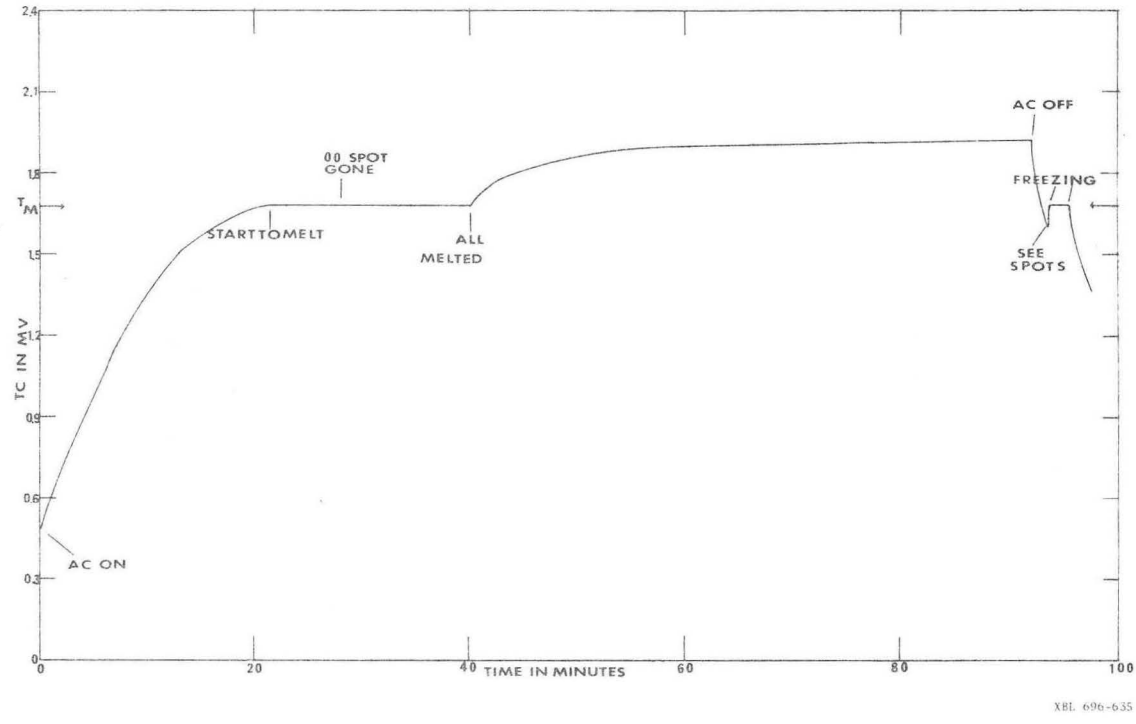

Fig. VI-6 Temperature vs time record for melting run on tin. AC refers to line power used to heat sample (actual current through sample is DC).

VII. STRUCTURE ON MOLTEN METAL SURFACES

A. Results on Pb, Bi, Sn

The technique for the study of surface melting properties can also be easily extended to the study of liquid surfaces. The most crucial property required of a material to be studied in the liquid state by LEED is that it have an equilibrium vapor pressure less than about 10^{-8} at the melting point. This is necessary to avoid contamination of the LEED optics by condensed vapors. The technique for studying liquid surfaces is a simple extension of that discussed in Section VI. After the sample is completely melted, the heat input is adjusted to maintain the liquid at a convenient temperature (usually about 5°C above the melting point). The electron scattering from the liquid surface can be investigated visually, optically (using the telephotometer) or photographically. Figures VII-1,2, and 3 are intensity maps of the scattering from molten lead, tin, and bismuth surfaces obtained by optical measurements. The telephotometer is focussed on a portion of the LEED screen and the voltage is scanned, the intensity at this angle obtained as a function of beam voltage. The photometer can then be focussed at a different screen position and the voltage again scanned. Photographic and visual studies indicate that the resulting patterns have radial symmetry about the electron gun axis. The ordinate on the figures refers to the angle on the screen with respect to the center of the LEED screen. The contours on Figs. VII-1-3 connect isointensity points at the indicated angle and voltage. The intensity units are arbitrary, however they were normalized to the approximate elastic/inelastic ratio so that the results should approximate the experimental situation which should be obtained at constant incident

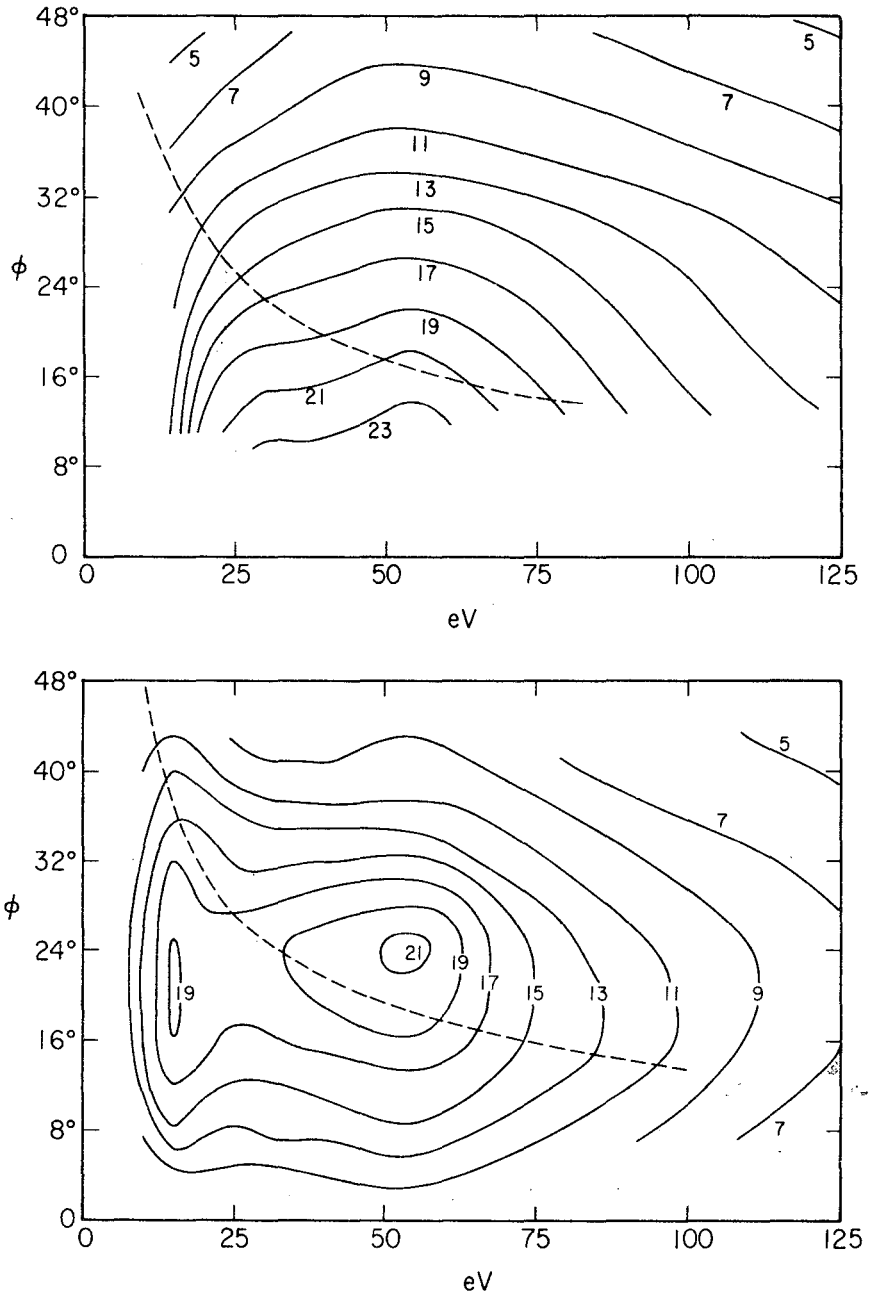

XBL 696-637

Fig. VII-1 (Top) LEED background intensity (contours) vs screen angle, ϕ, and beam voltage, eV, for electron scattering from a molten lead surface.

Fig. VII-2 (Bottom) LEED background intensity (contours) vs screen angle, ϕ, and beam voltage, eV, for electron scattering from a molten bismuth surface.

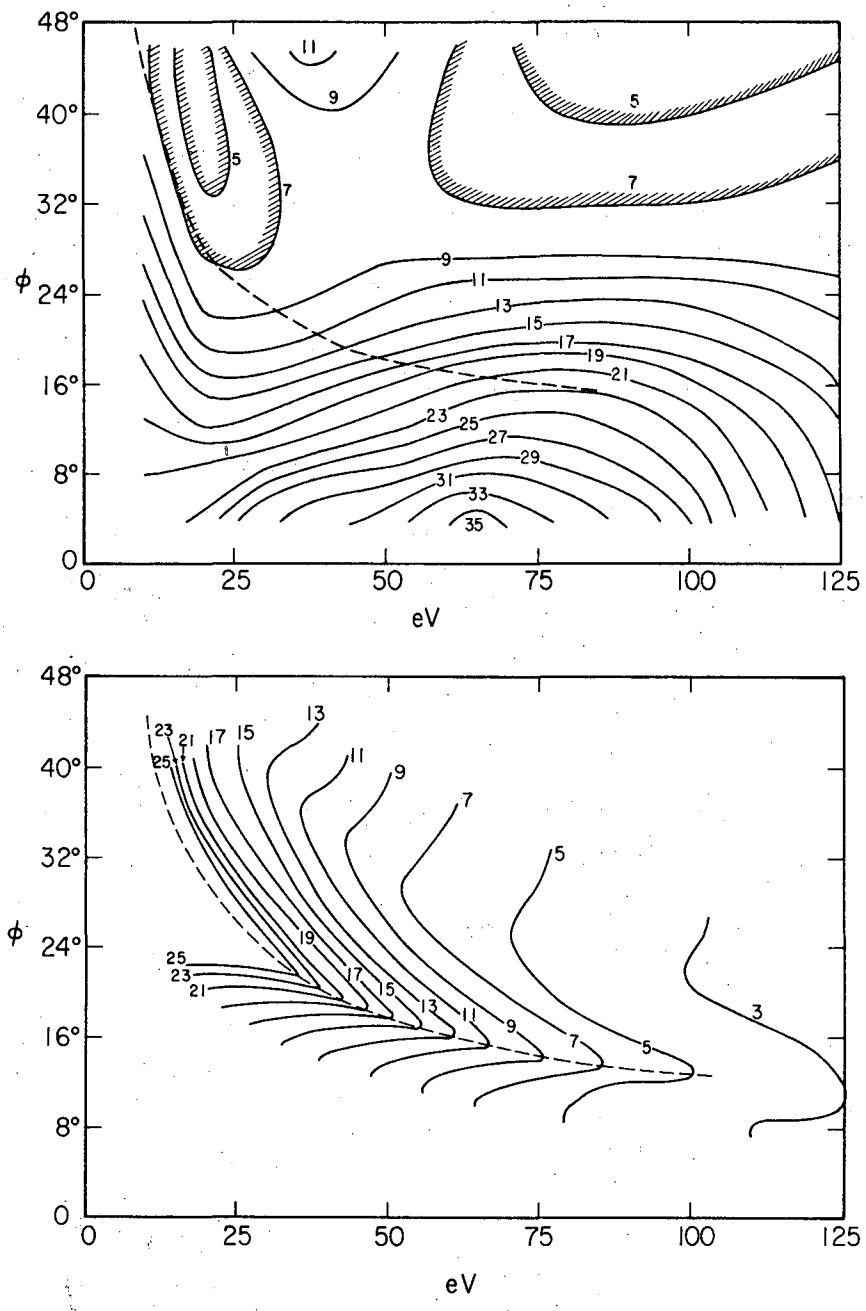

XBL 696-640

Fig. VII-3 (Top) LEED background intensity (contours) vs screen angle, ϕ, and beam voltage, eV, for electron scattering from a molten tin surface.

Fig. VII-4 (Bottom) Predicted LEED background intensity (contours) vs screen angle, ϕ, and beam voltage, eV, from liquid lead.

electron beam intensity. In addition, the intensities of the three curves are in terms of the same arbitrary units.

If the relative positions of atoms in the liquid surface could be described by the same radial density function as the position of atoms in the bulk liquid, then the intensity map would resemble Fig. VII-4 which is taken from the x-ray data of Kaplow[45] on bulk liquid lead. Scattering of high energy electrons from liquid metal surfaces give results similar to x-ray diffraction. The dotted lines in Fig. VII-1, 2, and 3 represent the locus of points for the first intensity maxima predicted from the bulk radial density functions.[45,46] In comparing these figures with Fig. VII-4 it is clear that there is almost no sign of any intensity modulation in the low energy electron scattering curves which correlates with the predictions from high energy electron scattering data on bulk liquid metals. This result will be discussed further in Section X. However, the intensity variations in the three figures is quite striking and should provide a great deal of information on the atomic scattering factor for lead, tin, and bismuth. This is discussed in Section VII-B below.

B. The Atomic Scattering Factor

No method of surface structural analysis using LEED can be completely accurate without the knowledge of the effective potential at a crystal surface for low energy electron scattering. Currently there are several techniques which can be used to calculate the atomic scattering factor from an arbitrary potential. Experimental determination of the atomic scattering factor would provide a very useful check on the utility of different model potentials. However, all previous attempts to determine the atomic scattering factor from measurements of background intensity

have led to ambiguous results because: (1) Diffraction effects from ordered arrays greatly distort the intensity profiles and are almost impossible to eliminate and/or correct for exactly. (2) Kikuchi effects[69] and multiple scattering effects from ordered arrays also lead to uncertainties in determination of background intensities independent of ordering. The only previous work on determination of atomic scattering factors followed the technique of depositing disordered layers on foreign substrates pioneered by Lander and Morrison.[17] However, the possibility of orienting influences and scattering by the ordered substrate materials also creates doubt in the interpretation of their results. Diffraction from the liquid, on the other hand, is not subject to any of these characteristics. The only two possible sources of ambiguity are diffraction features due to the radial distribution function and experimental uncertainties. The former can be approximated and compared to the experimental results which as discussed in Section VII-A indicate very low sensitivity of LEED to the radial distribution function.

There are several experimental factors to be considered. (1) The sample mountings obscure part of the fluorescent screen (as viewed from the window opposite the screen), which especially for the large lead discs used in some of our studies prevented measurements of the background intensity closer than 10° from the electron gun. (2) The screen only extends to about 48°, and thus no data beyond this angular region can be obtained. It should be mentioned that the details of the background intensity should not be a function of the direction of impinging beam if the atomic scattering factor is strictly a single "atom" property unaffected by interactions with neighboring atoms. For small rotations this result was verified experimentally. (3) Interference by non-homogeneous

magnetic fields (as from DC heating current used to heat the crystals, or the ion pump, or trimming magnets) causes the actual direction of impingement of the electron beam to vary as a function of electron energy. (4) The electron beam may strike the crucible material causing spurious intensity variations. These latter two problems can be greatly reduced if the crystal is carefully aligned while still solid and the diffraction spots can be used as a reference to reduce magnetic fields and scattering from crucible materials. (5) Because of the low intensity of the background very sensitive settings and large photometer apertures had to be used. The former resulted in a very large noise amplitude (often 5-10% of signal), the latter leading to imprecision in defining the exact screen angle corresponding to the scan. (6) There is some question whether electron emission is proportional to actual electron flux hitting the crystal: I have normalized the curves to constant emission. (7) Surface contamination can alter the results. (8) Finally, imperfections in the phosphor on the fluorescent screens, or in the grids, observation window, etc., introduces uncertainties in the results. For all these reasons (especially at the lower voltages) I doubt the quantitative accuracy of the intensity maps. But a great deal of visual and photographic checking assures me that the qualitative trends are accurate.

The intensity maps for Pb, Sn, and Bi suggest certain trends. Lead and tin are both metals in group IV^a of the periodic table and show very similar trends for the smaller angles (less than 30°) and higher energies (greater than 30 eV) with a weak ridge at moderate energies (55 eV for Pb, 65 for Sn) and much higher intensities at the smallest angles monotonically decreasing at larger angles. There are also certain similarities between the lead and bismuth at larger angles (greater than 30°)

and higher energies (greater than 40 eV) in that both have a ridge at about 55 eV and monotonically decreasing intensities at larger angles and energies. There is almost no angular region or energy range in which the intensity distribution for scattering low energy electrons from tin and bismuth show similar characteristics. As a general conclusion, therefore, the results suggest periodic behavior, with correlations for materials in the same row or column of the periodic table being greater than those not in the same row or column; the materials in the same group being more similar indicating the greater importance of valence electron configurations relative to total electron concentration. This conclusion is further discussed in Section X.

VIII. CRYSTAL GROWTH AND RESOLIDIFICATION

A. Results on Lead and Bismuth

In addition to the information on surface melting characteristics and the atomic scattering factor, the studies of the surface structure during melting and refreezing of metal crystals provided a great deal of information on crystal growth from the melt. Figures VI-2 and VI-6 show a record of two representative experimental runs for these studies. The record of cooling rates coupled with visual observations of the diffraction patterns upon cooling provide a technique for the correlation of the orientation of the surface of crystals regrown from the melt with cooling rates. In this section reference will be made to the freezing times and cooling rates for different experiments. Freezing times will refer to the time the crystal remained at the melting point during cooling; cooling rates will refer to the initial slope of the temperature vs. time curves immediately after the crystals were completely refrozen. Figures Vi-1 and VI-2 show the two extreme cooling rates possible with the crystal geometries used in the studies. The fastest cooling rate (in Fig. VI-2) was about 2°C/sec; the slowest (in Fig. VI-1) was about .02°C/sec. Orientations of the regrown crystals were checked by locating the specular, or 00-spot, for each prominent crystallite. Where the specular spot for a particular crystallite appeared on the LEED screen, the orientation of the corresponding crystal face was taken as roughly parallel to the crystal surface. For example, if a hexagonal pattern were observed with the 00-spot 11° from the surface normal, that crystallite could be indexed to have its ⟨111⟩ axis oriented 11° with respect to the surface normal. Four important observations were made: 1. For the smaller cylindrical samples surface tension creates a very decidedly

rounded liquid surface. 2. The contraction of lead upon freezing (especially for rapidly cooled samples) tended to create "craters" at the surface of the crystal while, conversely, the expansion of bismuth upon freezing tended to create "pinnacles" on the crystal surface. 3. The crucible surface acted as a source of heteronucleation sites. 4. As a result of 1, 2, and 3 rarely did the recrystallized lead or bismuth give predominantly one single crystal, but rather tended to give a large number of crystallites. However, invariably one crystallite was much larger than the others and gave rise to a sharper and brighter diffraction pattern than any of the other crystallites. It is these largest crystallites which are discussed in this section.

Table VIII-I lists the preferred orientation of these largest crystallites for lead and bismuth as a function of freezing time at the melting point. Correlation of crystal orientation with the time of anneal was good as indicated in the table. In summary, for lead, very short freezing times (less than one min) favor the formation of generally polycrystalline masses with no preferred orientations. Freezing for periods of about 1 to 3 min produced ⟨100⟩-oriented crystallites, generally, giving relatively poor diffraction patterns except in rare cases as shown in Fig. VI-4. Freezing for periods greater than about 3 min produced predominantly ⟨111⟩-oriented crystallites, usually producing very sharp diffraction patterns, especially for the longest "freezes" (10-15 min). In fact, the Debye-Waller measurements were performed on recrystallized Pb(111) surfaces because they gave sharper diffraction patterns than the original ⟨111⟩-oriented single crystals put into the chamber. As an example of how judicious regulation of the freezing times can lead to creation of the different faces of Pb, Figs. VI-3, 4, and 5

Table VIII-I

Lead Growth Characteristics

Freezing time	Total runs	⟨111⟩	⟨100⟩	Polycrystal
0-3 min	17	2	11	4
3-15 min	13	10	3	0

Bismuth Growth Characteristics

Freezing time	Total runs	$\langle 01\bar{1}2 \rangle$	⟨0001⟩	Polycrystal
0-2 min	4	1	3	0
2-12 min	5	4	1	0

were all taken on the same lead disc after successive melting runs; the Pb(110) surface was the original orientation; the Pb(100) surface appeared after a short freezing time (~ 2 min), the Pb(111) surface after about a 14 min freezing. Thus, if one uses a 2 min freezing time as the dividing line, then there is an 80% correlation between predicted surface orientation and that obtained experimentally. No other experimental variable (as estimated temperature gradient variations, crystal size or geometry, etc.) appeared to affect the crystal growth characteristics. However, with respect to the quality or size (as opposed to the orientation) of the recrystallized regions of single crystal, the larger disc-shaped samples produced far better results. It appears that the effect of surface tension in producing rounded liquid surfaces tended to hinder the growth of good quality crystals in all but the large disc-shaped crystals.

Interesting correlations between bismuth and lead were found in this study with respect to their recrystallization orientations. The similarity in crystal preparation, surface Debye temperature, and atomic scattering factor has already been discussed. Since the bismuth crystals had the same geometry as the smaller lead crystals, the available range of freezing times and cooling rates was the same. In fact, of nine cooling runs tried in these studies the "predicted" orientation was observed in seven of them. Again freezing times of about 2 min (corresponding to cooling rates of 0.5°C/sec) seemed to be the dividing lines. Short freezing times favored crystallites oriented with the ⟨0001⟩ axis perpendicular to the crystal surface, while long freezing times favored crystallites with the $\langle 01\bar{1}2 \rangle$ axis oriented perpendicular to the crystal surface. Freezing times near 2 min produced both orientations (in the

two experiments tried). What is most interesting about these results is that the $(01\bar{1}2)$-face is the pseudocubic (100)-face and the (0001) face is the pseudocubic (111)-face. Thus, short freezing times on bismuth produce patterns with hexagonal symmetry while short freezing times on lead produce patterns having square symmetry and conversely for the long freezing times.

No theoretical justification is presented to explain these results, however, several other observations should be mentioned to complete the discussion. In none of the bismuth studies was any undercooling of the liquid observed which frequently occurred in the lead studies and in the results discussed below. Also, because of the crystal geometry, the crucibles should be cooler than the liquid samples and thus the molten metals should freeze first at the sides in contact with the Fe crucible. This fact of freezing at the sides first was verified by visual observation which makes the correlation of orientation with freezing times all the more remarkable.

B. Results on Tin

The results of recrystallization for tin samples are much more difficult to interpret than those for lead or bismuth. Figure VIII-1 shows the crystal structure of tin.[70] Figure VIII-2a depicts the (100)-face which was used at the start for all the tin melting studies. Figure VIII-2b gives the diffraction pattern expected for this surface. The dotted lines show the extra features found in the diffraction pattern, the dotted lines in Fig. VIII-2a representing a possible assignment which would produce the diffraction pattern observed. Whether these extra features are due to a clean Sn(110) surface or to impurities has been discussed in Section VII. However, this surface was regrown from the

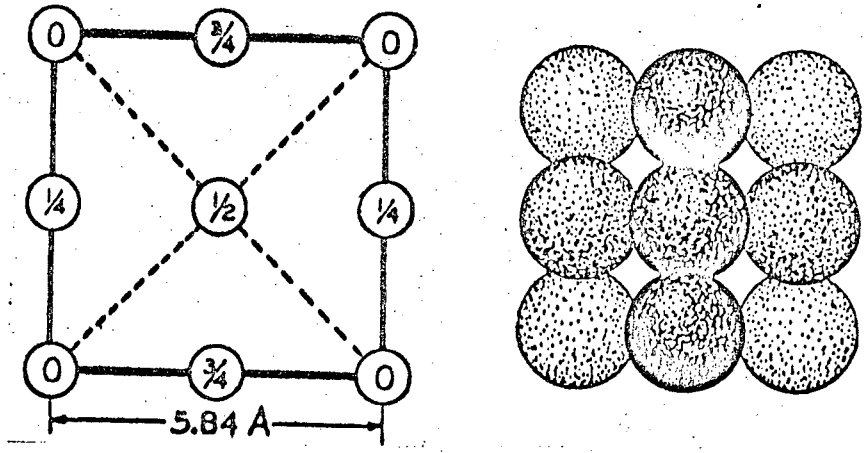

Fig. VIII-1 Crystal structure of white tin with tetragonal unit containing four atoms in special positions: 0 0 0; 0 1/2 1/4; 1/2 0 3/4; 1/2 1/2 1/2 of space group D_{4h}^{19} (I4/amd). The unit, with a_o = 5.82Å and C_o = 3.17Å at 25°C. Figure on left shows the atomic arrangement within the tetragonal unit of white tin projected on the basal, C_o, plane. Figure on right is a packing drawing corresponding to the projection on the left.

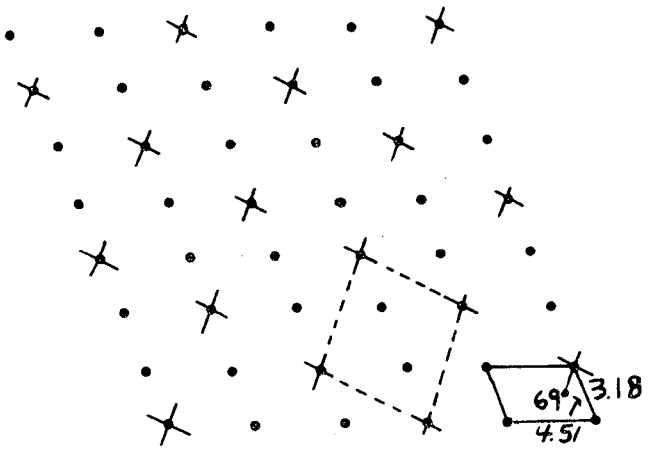

Fig. VIII-2a Crystal structure (dots) representing Sn(110) surface. Crosses indicate possible atom sites occupied to give diffraction pattern shown below. Solid lines give primitive cell for 1x1 structure; dashed lines give unit cell for surface structure.

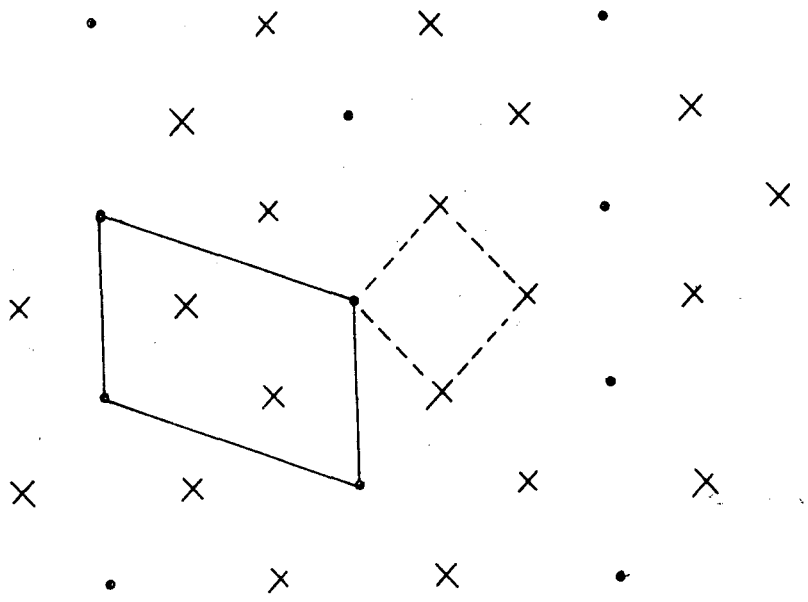

XBL 696-709

Fig. VIII-2b LEED pattern (schematic) obtained from a Sn(110) surface. Dots show spots expected for the 1x1 structure; crosses show extra spots observed. Solid lines show reciprocal lattice unit cell expected for 1x1 surface; dashed lines show reciprocal net found for experimentally observed diffraction pattern.

melt in only one of over a score of recrystallization runs. In general, most recrystallized tin surfaces are characterized by uniaxial or linear disorder, or polycrystallinity. However, four structures could be distinguished which formed in crystallites large enough to give clear diffraction patterns; the surface meshes are drawn in Fig. VIII-3a to d. Further, a structure very similar to that depicted in Fig. VIII-3b appeared, but due to the very high intensity of the spots and similarity to the Si(100) surface (it formed after many melting and recrystallizing runs performed in silicon crucibles as described in Section VI) it was assumed not to be characteristic of the Sn crystal. However, the structures characterized by unit meshes depicted in Fig. VIII-3b and c are very similar to the indexed Si(100) surface unit mesh and "b" was observed after a series of runs performed in a molybdenum crucible. Ordinary chemical analysis would be essentially impossible for the minute quantities which might contaminate the Sn surface. Figure VIII-4 shows an optical micrograph for a recrystallized Sn surface (there was no perceptible difference in micrographs between the Sn surface "contaminated with silicon" and that melted in the molybdenum crucible). None of the unit meshes drawn in Fig. VIII-3 can be indexed to give any of the low index faces of tin; the lack of reproducibility suggests they might be due to contamination from the bulk or crucible impurities segregating as the surface. However, if they were due to diffraction from facetted surfaces or surface structures of high index faces of pure tin, no means were available in these studies to differentiate between these possibilities. No correlation between results and temperature gradients, cooling rates, etc., were found and reproducibility of recrystallized surfaces was very poor.

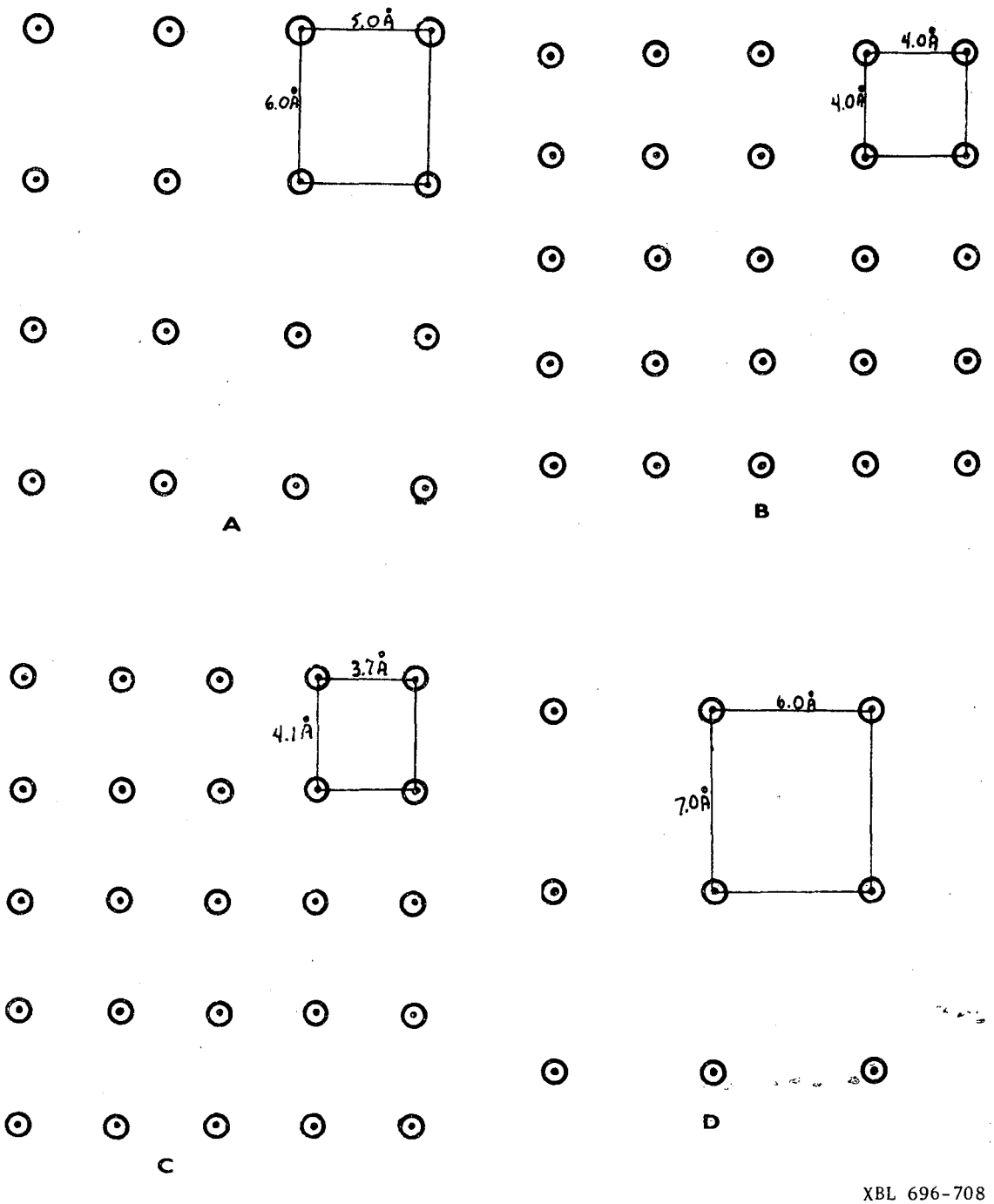

Fig. VIII-3 Possible surface atomic arrangements corresponding to four different LEED patterns obtained from recrystallized tin surfaces.

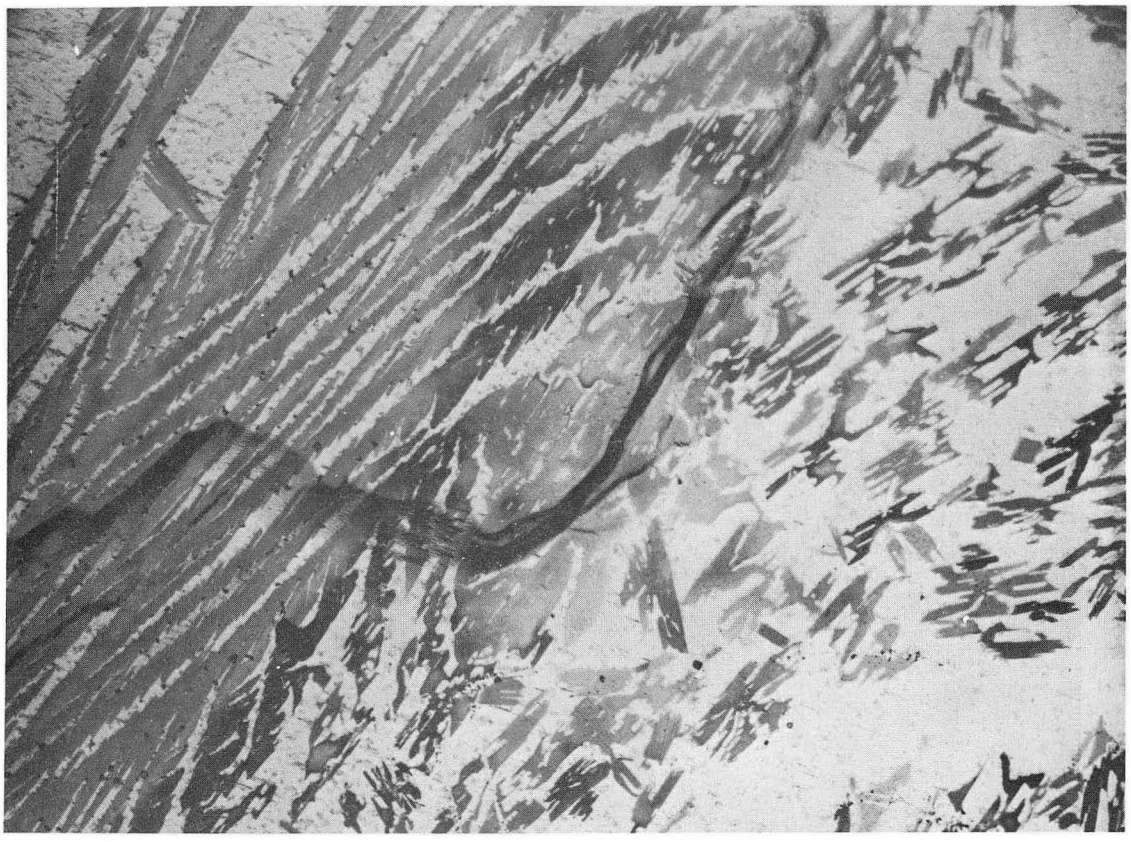

XBB 699-5789

Fig. VIII-4 Optical micrograph of a recrystallized tin surface. Magnification 160×

In summary, therefore, unlike bismuth and lead, no conclusion is drawn regarding the nature of tin recrystallization. However, several general considerations pertinent to all these recrystallization experiments arise from the tin work. First, that the usual contamination problems common to all LEED experiments are magnified many times in these studies because impurities in both the sample and crucible have to be considered and diffusion through the liquid is many times faster than in the solid especially if one allows for convection currents in the liquid. The liquid might be expected to be much more chemically reactive to ambient because of its higher temperature. In addition, the role of nucleation sites on the crucible may affect the results: an interesting observation found by comparing Figs. VI-1 and 6 is that the tin undercooled far more than either the lead or bismuth did, i.e. the temperature was below the melting point before freezing commenced. Further, occasionally diffraction spots were observed from structures on the tin surface seconds before the temperature curve showed that solidification had commenced, i.e. while undercooled. The presence of extensive undercooling (10°-20°C) and the formation of ordered surface structures immediately upon freezing at the melting point were characteristics which made the tin results different from the lead and bismuth results. The effect of impurities on the tin surface could explain the lack of reproducibility of growth characteristics and by implication explain the success in reproducing growth characteristics for the lead and bismuth samples because of their higher purity.

IX. STUDIES ON THE SURFACE STRUCTURE OF METALS AFTER VACUUM VAPORIZATION

A. General Experimental and Theoretical Considerations

Experiments[71] on the vacuum vaporization of metals, especially silver, have found kinetic vaporization rates equal to the ideal equilibrium rates and independent of crystallographic orientation. Several possible mechanisms to explain these results (which differ from results on the sublimation of molecular species as alkali halides[72]) can be postulated. One possibility would be that the surface is disordered (i.e. atoms are in liquid-like states) during vaporization. Hirth and Pound[73] state that where there is a sufficient number of ledge sources the maximum equilibrium vaporization rate is obtainable. The Hirth and Pound model for a "non-roughened" surface, where vaporization is diffusion controlled, gives a vaporization rate which is one-third of the maximum rate. Optical micrography from a vaporized Ag(100) surface, Fig. IX-1, shows a very distinctly irregular surface with many large (order of 1μ) "rounded hillocks" present. [These hillocks were not present prior to vaporization, but the surface did have large numbers of chemical etch pits which might indicate the presence of emerging dislocations (or grain boundaries) which could lead to creation of the hillocks as a result of vaporization.] The optical micrograph is quite similar to a published micrograph of Winterbottom and Hirth.[71] However, the LEED pattern from this surface was a very sharp, intense Ag(100)-1×1 pattern. From Section II-A we concluded that ordered regions of only 10,000 atoms were sufficient to provide sharp, intense diffraction patterns. It is quite likely, therefore, that the regions between the "hillocks" are large enough (if ordered) to produce the sharp diffraction

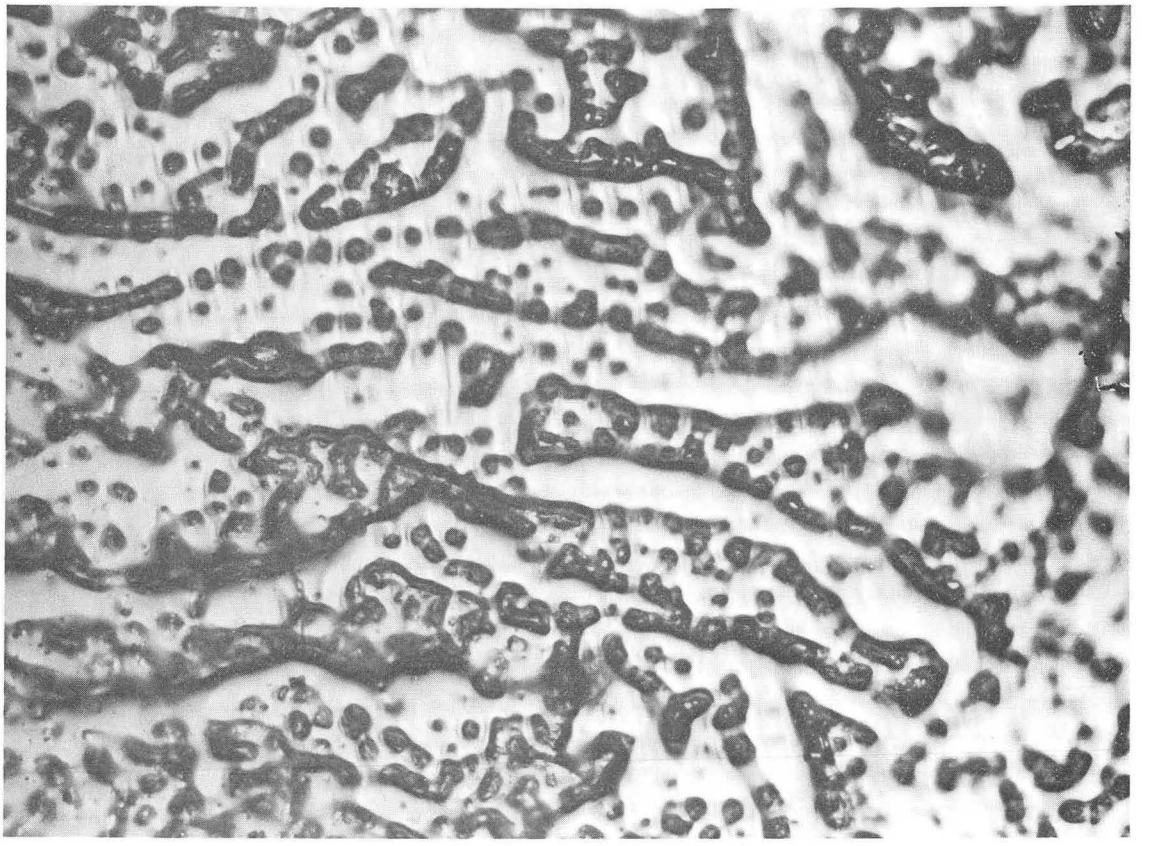

XBB 699-5790

Fig. IX-1 Optical micrograph of a vaporized silver (100) surface. Magnification 480×

patterns observed from the vaporized silver surface.

The purpose of this study was to determine whether the surface did become disordered at an atomic level upon vaporization. To determine if the LEED results are significant in answering this question, the kinetics for the vaporization process must be investigated. For a monatomic solid which vaporizes as a monomer (as is the case for Ag^{74} and Ni^{74}), the overall vaporization is described as:

$$J_T = \frac{J_D J_E}{J_D + J_E} , \qquad \text{IX-(1)}$$

where J_T = total rate, J_D = surface diffusion rate, and J_E = rate at which atoms break away from the lattice (i.e. the rate for equilibrium vaporization).[75] Hirth found that the relative magnitudes of J_D vs J_E are a function of the dislocation (or impurity site) concentration. The concentration of such sites (or dislocations) on metal surfaces is sufficiently large in almost all cases so that the vacuum vaporization is not diffusion controlled and the maximum vaporization rate is observed. Thus, atoms can be considered to be vaporizing "in situ" from ledge sources without being able to diffuse along the metal surface. If these atoms are at equilibrium sites, then the LEED pattern would show a pattern characteristic of very ordered surface. But, if vaporization were diffusion controlled then atoms (upon diffusing on the surface) could assume "disordered" positions. In order to observe a surface as it appears under vaporizing conditions, the crystal would have to be quenched fast enough to prevent the surface atoms from assuming an equilibrium (instead of kinetically controlled) configuration prior to observation in LEED.

The actual vaporizing surface, of course, could not be observed by LEED because the high vapor flux would immediately coat the LEED optics and destroy the equipment. Using a simple model, the root-mean-square diffusion distance on a surface can be derived as[76]:

$$\langle \ell^2 \rangle^{1/2} = \sqrt{D_0 t}\, \exp(-\Delta H_s^{\ddagger}/2RT) \qquad \text{IX-(2)}$$

where $\Delta H_s^{\ddagger}$ refers to the surface activation enthalpy of diffusion, D_0 is diffusion constant for the material, and t can be regarded as a "diffusion time." From previously published data,[77] $\Delta H_s^{\ddagger} \tilde{=} 16$ kcal/mole, $D_0 \tilde{=} 10^{-2}$ cm^2/sec for a Ag(100) surface. LEED experiments on the ion bombarded Ag(100) surface indicate that at about 350°K the surface damage is annealed out in less than five minutes. From this observation an estimate for the amount of time it should take at say 750°C (where vapor pressure is 10^{-5}torr) to anneal out disorder can be calculated. The result is on the order of a millisecond. This is obviously too fast for disorder to be "quenched-in" in the usual LEED design shown in Fig. III-4. Experiments recently performed by Bedair[10] using pulsed laser heating on a nickel surface open the possibility for just the proper conditions for observing the "quenched-in" previously vaporizing surface. However, in his experiments super-hot filaments in the laser beam tended to "burn holes" (as observed by optical microscopy) into the nickel surface and thus the observed resulting LEED pattern (somewhat resembling a lightly ion bombarded surface) may not necessarily be characteristic of the vaporized surface. The results from these studies are discussed below.

B. Experimental Findings for Structure of Nickel and Silver Surfaces after Vacuum Vaporization

The samples were mounted as indicated in Fig. III-7; the thermocouple was calibrated against an optical pyrometer in the nickel studies. The Ni(111), Ni(100), and Ag(100) surfaces were studied. In all experiments the procedures described in Section III B were used to obtain "clean, ordered surfaces." The crystals were heated with the "can" opened to a temperature where vapor pressures were about 10^{-8} torr. (575°C for Ag; 925°C for Ni). For temperatures between these and the melting points (961°C for Ag; 1453°C for Ni) the crystals were heated with the Ta cans closed to prevent contamination of the LEED chamber. This technique was quite successful and no sign of significant metal deposition was found on the interior of the chamber even after six crystals were heated to the melting point (where equilibrium vapor pressure is about 3×10^{-3} torr for both silver and nickel). However, the background pressure in the chamber rose quite a bit in the course of the experiments; frequently above 10^{-7} torr in Ni runs (and likely the pressure was even higher inside the Ta can). Most likely this was due to the very high currents needed to melt the nickel samples (about 85 amps) which also was capable of heating the copper leads quite hot and/or outgassing from the tantalum can caused by radiant heating of the tantalum can. In one study a thermocouple contacted the can and read 400°C which does not seem unreasonable. Due to the heating of the leads, the crystals did not cool below the "annealing" temperatures very quickly - often taking 5 minutes for a nickel crystal to cool to 250°C.

The silver crystals usually cooled to below 100°C within 5 minutes since the lower currents necessary to heat the silver crystals to the melting point (about 60 amps) did not heat the leads very much. In every case the LEED pattern obtained from the crystals after vaporization showed the pattern characteristic of the ideal ordered 1×1 structure (except after several of the Ni runs which showed structures characteristic of the usual ambient gas adsorption structures discussed in the appendix), and, in fact, produced the sharpest such patterns ever observed for these materials in the LEED chamber.

Optical micrographs (Figs IIC-3 and IX-1) correlate very well with those of Winterbottom and Hirth and indicate the vaporized surfaces are quite macroscopically irregular. The Ni(111) surface shows more crystallographically oriented structures than the Ag(100) surface, however, both crystals showed similar behavior in LEED and indicated no significant disorder on an atomic level.

This result indicates that the vaporizing surface cannot be greatly disordered (on an atomic level) or possess liquid-like characteristics. Since I could not "quench" the surfaces fast enough to prevent some annealing of the surfaces (i.e. providing sufficient time for atoms to diffuse along the surface and assume equilibrium sites), there is some possibility that the disordered surfaces may have transformed upon cooling to an ordered state. However, two facts tend to refute that possibility: 1) If, indeed, the surface layers were liquid-like during vaporization, upon cooling some degree of polycrystallinity or uniaxial disorder should be observed: in the vaporizing experiments none was. 2) Inadvertently the silver crystals were heated hot enough to vaporize

(after as high as 700°C) while the optics were on and the tantalum can opened. In fact, a chamber was coated by the vaporized silver; yet, the diffraction pattern remained sharp and clear after vaporization.

In Section IV-C it was pointed out that a Ag(100)-ring structure has been observed on occasion after high temperature experiments. The inability to reproduce this structure after all vaporization experiments suggest that the ring structure will form only under particular conditions and is not the most characteristic state for a Ag(100) crystal surface during vaporization.

X. DISCUSSION AND CONCLUSIONS

A. LEED Studies of Surface Lattice Dynamics

The four metals studied in the Debye-Waller experiments discussed in section V provide a good cross-section of metals for the study of surface lattice dynamics. Iridium is one of the hardest metals known, lead and bismuth are two of the softest. Lead, palladium, and iridium are face-centered cubic, bismuth is rhombohedral. In general, for all the materials studied: surface atoms have a mean square displacement normal to the surface due to thermal lattice vibrations two to five times larger than for the bulk atoms at the same temperature. For the soft metals (and more open crystal faces) the electron beam penetration is greater at moderate energies (25-200eV) than for hard metals or more densely-packed surfaces. However, quantitatively, the results of Debye-Waller measurements using LEED are subject to many experimental and interpretative difficulties. Section II-B outlines many of the difficulties of analysis while section V presents the experimental difficulties. Values of $\theta_{D,\ surf.}$ are known generally only to within an uncertainty of about 10-20%. Further, anharmonicity in lattice vibrations at crystal surfaces and multiple scattering of low energy electrons can lead to even larger uncertainties in $\langle u_\perp^2 \rangle$ SURF. Thus, it is not yet possible for LEED studies to resolve differences in models of surface lattice dynamics.

Theoretically, all reasonable models of metal surfaces lead to the prediction of larger surface mean square displacements than bulk displacements; and also that the bulk value for displacements is approached

rapidly upon penetration of the surface only a few atomic layers. For example, Wallis, et al.[14] predict mean square displacements normal to the surface twice that of the bulk and the value of the mean square displacement is within 5% of the bulk value by the fifth atomic layer from the surface. The only models relating electron penetration to electron energy give results comparable to Eq. IIB(6). My results: $\langle u_{\perp}^2 \rangle_{SURF}$ for palladium is 4 x $\langle u^2 \rangle_{BULK}$ contradicts Wallis' model for face-centered cubic metals and indicates that the assumption of anharmonic effects and/or different force constants for surface atoms is necessary to explain the experimental results.

As a suggestion for future experimental work: Debye-Waller studies of the nonspecular spots is necessary using Faraday collectors at large diffraction angles, θ, [see Eq. VB(6)] in order to obtain information on the parallel component of atomic displacements at the surface. If precision could be improved, then curvature in the log $(I_{00}-I_B)$ vs T Debye-Waller plots could be related to possible disordering or anharmonic effects. Also, closer scrutiny of the θ_D vs eV plots might lead to the detection of effects which are due to multiple scattering. More extensive measurements of the thermal diffuse scattering could lead to a deeper understanding of the phonon spectrum at the surface. LEED has already set the groundwork for understanding surface lattice dynamics: we now know surface atoms have mean square displacements normal to the surface two to five times the bulk atoms; that the bulk value is approached very rapidly with greater electron beam penetration and that such beam penetration is a function of the hardness of the metal and the atomic density of the surface plane.

B. LEED Studies of Surface Phase Transformations

Surface structural changes can occur at temperatures at which the bulk phase remains unperturbed. The two presently most convincing experimental verifications of this supposition are the Au(100)-5×1 and Si(111)-7×7 structures. There is sufficient evidence for their existence as properties of the clean surface that I do not feel obliged to explain them away by involking models of alloy formation, ambient or bulk impurity contamination, etc. The surface free energy can indeed be a minimum for the rearranged surface.[15] The increased mean square displacements and reduced activation energies of diffusion[77] of surface atoms indicate the essential "isolation" of the surface layers as a separate phase. Extension of Brewer's model to surfaces leads to qualitative agreement with the experimental results. The formation of a surface can be looked upon as the splitting of interatomic bonds leading to different valences and bonding states for surface atoms. The correlation of such altered bonding states with changes in surface structure are quite consistent with results bulk phases. What is also clear is that the presence of catalytic quantities of impurities or vacancies can also lead to surface structural changes. Likewise, thermal gradients and mechanical strains can also enhance the rearrangements of surface atoms. Further studies with the addition of analytical monitoring tools as Auger spectroscopy, mass spectrometry, and ellipsometry coupled with the intensity analysis of LEED patterns should lead to a better understanding of the structural chemistry and physics of surfaces.

Melting is a unique structural change which, unfortunately, is

presently very poorly understood. Of the many theories (samples of which are presented in Appendix C) none can explain both its thermodynamical and kinetic characteristics. Information on the structure of liquids, especially at liquid surfaces would be a very significant addition to understanding melting. Unfortunately, for the reasons discussed in Section IIC and verified experimentally as discussed in Section VIII, LEED under presently realizable experimental conditions appears unable to aid in elucidating the surface structure of liquids.

It is a well-known experimental result that recrystallized solid surfaces possess an "equilibrium form." If one postulates that the equilibrium surface is stable with respect to the disordered or liquid surface for all temperatures below the melting point and thermodynamically unstable at all temperatures above the melting point, then melting is the transition from one state to the other, i.e. is a surface phenomena based on surface thermodynamical properties. The tendency for theorists to concentrate on bulk properties rather than surface properties is based on two simple factors: that it is difficult to obtain experimental values for surface properties and the difficulty in superheating solids. Superheating of solids is difficult because nucleation of the liquid phase can be provided by an imperfect or disordered surface site. Emerging dislocations, vacancy clusters, impurity aggregates at grain boundaries, etc. are such sites which are always present on a solid surface. Avoiding problems of surface imperfection by heating from the inside of a solid outward in order to observe super-heating can only succeed where melting leads to an increase in density - the success of Kass and Magun[78] in superheating ice indicates the correctness of this viewpoint. Similarly, my results on the melting of lead and bismuth

surfaces fit these ideas of initiated melting at surfaces precisely. If melting nucleates at disordered sites then the ordered surface regions should remain intact until the melting point is reached. Turbull's[79] analysis of the kinetics of melting (which have been verified for Ga metal[80] as well as for viscous liquids, P_2O_5 [82] and SiO_2 [83] predict very rapid propagation of the melting front on an atomic scale in agreement with my experimental results on lead, bismuth, and tin. To summarize my ideas: the thermodynamic melting point is determined by the stability of the equilibrium surface relative to the disordered (or liquid) surface. Melting is nucleated at disordered regions as around emerging dislocations, vacancy clusters, etc. and propagates from these regions into the bulk qualitatively as described by the models of Stranski[68] and Turnbull.[79] This view of the nature of melting is consistent with all melting experiments. The exact quantitative formula for predicting the thermodynamic melting point for the solid is probably related to some combination of the theories similar to those described in Appendix C if one substitutes values appropriate to the equilibrium surfaces, rather than to the bulk. Interestingly, better correlation to the Lindemann formulae as, for example, Eq. VI-C(4) are obtained if the $\theta_{D,SURF}$ values are used rather than bulk values for those metals studied.

In metals, no discontinuity is found in non-equilibrium vaporization rates at the bulk melting point. In the non-equilibrium vaporization of the Ag(100) surface, Hirth and Winterbottom[71] indicate that the normal concentration of dislocation centers, etc., is sufficient to make the breaking away of atoms from ledges the rate determining step.

As discussed in Section IX this would be consistent with my results that the vaporized surfaces of silver and nickel remain ordered

to very high temperatures (near to Tm). My results, however, can add no information as to whether in the absence of large concentrations of dislocations, etc. a vacuum vaporization rate less than the equilibrium rate would be observed or if such a vaporized surface might be disordered. Studies on such "perfect" solids might provide very interesting data useful in understanding not only the vacuum vaporization mechanism of metals, but of other solids, too.

The crystal growth data are presented in Section VIII merely as additional information. Until a study is made correlating the LEED results for the orientation of the surface atomic layers with x-ray data, no definite conclusion or mechanism can be discussed. The results of my experiments indicate that the orientation of the recrystallized surface is a function of the rate of cooling; the degree of ordering is related to the sample geometry. In all cases only certain low-index faces are regrown in agreement with models by Stranski[68] and Burton, et al.[67] for cubic metal solids.

C. LEED Theory

The specular intensity curves presented in Appendix B and the intensity maps in Section VII provide useful data for correlating with proposed LEED theories. In addition, Fig. B-2 indicates that intensity curves provide a very useful means for monitoring surface structural changes and verifying if a certain pattern symmetry is the result of the same atomic configuration as, for example, had been found in a previous study. The other uses for the specular intensity curves are discussed in a previous publication[84] and will not be discussed further here.

Comparing Figs. VII-1 to 3 with Fig. VII-4 clearly shows the

insensitivity of LEED at normal incidence to the possible radial distribution function for the liquid surface. As a result these figures may be regarded as "maps" of the atomic scattering factor unperturbed by diffraction effects. One important result is that there is more similarity between the tin and lead and bismuth than between the tin and bismuth curves. In proceeding up the group 4a column from tin to lead the main change is a leveling of features, i.e. lead shows less "steepness" of the downslope with increasing angle and does not have a saddle-point at about 45 eV and $\phi \sim 32^\circ$ as is present on tin. In proceeding along the 6th row from lead to bismuth the main change seems to be a "rotation" of the prominent maximum from near 0° to about 24° for all electron energies.

Extensions of these studies to higher electron energies and larger angles and to another family of elements as Al, Ga, In, may provide very interesting results both for LEED theory and for the verification of the electron scattering properties of atoms on a metal surface.

ACKNOWLEDGMENTS

My deepest and most sincere gratitude is extended to Professor Gabor A. Somorjai whose seemingly boundless energy and encouragement have constantly inspired me during my graduate studies. I wish to extend my appreciation to the Department of Chemistry and the Inorganic Materials Research Division of the Lawrence Radiation Laboratory of the University of California who have provided me with: (1) an almost perfect graduate student environment, and (2) teaching and research assistantships, respectively, to keep body and soul together during my residence here in Berkeley. Virtually every member of my research group is entitled to some commendation for kindnesses to me, but I wish to express special gratitude to: United States Navy Lt. Commander Hylan B. Lyon, Jr., whose early guidance was most helpful; Helen H. Farrell, whose personal help and kindness even overshadow her tremendous scientific contributions to my work; J. Gordon Davy and Whalun Szeto for their help in solving those endless experimental snags. Special thanks are also extended to Pat Shand, Nancy Monroe, and the entire staff for their help in the preparation of publications and this dissertation. To Duane Newhart and Emery Kozak I can only express my regrets... that two such master craftsmen (and very nice guys) may not be found anywhere else in this country.

I wish to express my appreciation to the United States Army for granting me an educational delay prior to entering active duty as a lieutenant in the Chemical Corps so that I could complete the doctoral program.

My research was performed under the auspices of the United States Atomic Energy Commission.

REFERENCES

1. J. J. Lander and J. Morrison, Surf. Sci. 6 (1), 1 (1967).

2. R. L. Park and H. E. Farnsworth, J. Chem. Phys. 43, 2351 (1965).

3. P. J. Estrup and J. Anderson, Surf. Sci. 8, 101 (1967).

4. R. E. Schlier and H. E. Farnsworth, Low Energy Electron Diffraction Studies of Cleaned and Gas-Covered Germanium (100) Surfaces, in Semiconductor Surface Physics, R. H. Kinston, ed., (University of Pennsylvania Press, Philadelphia, Pa., 1957).

5. N. R. Hansen and D. Haneman, Surf. Sci. 2, 566 (1964).

6. V. Heine and D. S. Boudreaux, The Relationship of LEED Intensities to Sample Band Structure: A Matching Formalism, presented at LEED Seminar, Sept. 8, 1967, Polytechnic Institute of Brooklyn.

7. A. J. Pignocco and G. E. Pellisier, J. Electrochem. Soc. 112 (12), 1188 (1965).

8. L. H. Germer and A. U. MacRae, J. Chem. Phys. 37, 1382 (1962).

9. A. E. Morgan and G. A. Somorjai, J. Chem. Phys., in press.

10. S. M. A. Bedair, Ph.D. Dissertation, University of California, Berkeley, 1969.

11. R. M. Goodman, H. H. Farrell, and G. A. Somorjai, J. Chem. Phys. 48 (3), 1046 (1968).

12. J. M. Charig, Appl. Phys. Letters 10 (5), 139 (1967).

13. A. M. Mattera, R. M. Goodman, and G. A. Somorjai, Surf. Sci. 7, 26 (1967).

14. B. C. Clark, R. Herman and R. F. Wallis, Phys. Rev. 139 (3A), 860 (1965).

15. J. J. Burton and G. Jura, Possible Interpretations of LEED Results, in The Structure and Chemistry of Solid Surfaces, G. A. Somorjai,

ed., (John Wiley and Sons, Inc., New York, 1969).

16. J. J. Gilvarry, Phys. Rev. 102, 308 (1956).

17. J. J. Lander, Low Energy Electron Diffraction and Surface Structural Chemistry, in Progress in Solid State Chemistry, Vol. 2, H. Reiss, ed., (Pergamon Press, New York, 1965).

18. C. Kittel, Introduction to Solid State Physics, 3rd. ed., (John Wiley and Sons, Inc., New York, 1966).

19. H. E. Farnsworth, Phys. Rev. 43, 900 (1933).

20. N. J. Taylor, Surf. Sci. 4, 161 (1966).

21. P. J. Estrup and J. Morrison, Surf. Sci. 2, 465 (1964).

22. P. W. Palmberg and T. N. Rhodin, Phys. Rev. 161, 586 (1967).

23. H. D. Heidenreich, Fundamentals of Transmission Electron Microscopy, (Interscience Publishers, New York, 1961).

24. R. L. Gerlach and T. N. Rhodin, Surf. Sci. 8, 1 (1967).

25. H. B. Lyon, Jr., Ph.D. Dissertation, University of California, Berkeley, 1967.

26. A. V. MacRae and L. H. Germer, Ann. N. Y. Acad. Sci. 101, 627 (1963).

27. J. J. Lander and M. Morrison, J. Appl. Phys. 34 (12), 3517 (1963).

28. H. H. Farrell and G. A. Somorjai, Phys. Rev., in press.

29. G. Gafner, Calculation of Back-Reflected Beam LEED Intensities Using a Plane Wave Multiple Scattering Mechanism, in The Structure and Chemistry of Solid Surfaces, G. A. Somorjai, (John Wiley and Sons, Inc., New York, 1969).

30. R. W. James, The Optical Principles of the Diffraction of X-ray, (Cornell University Press, Ithaca, New York 1965).

31. H. B. Lyon, Jr. and G. A. Somorjai, J. Chem. Phys. 46, 2539 (1967).

32. J. M. Ziman, Principles of the Theory of Solids, (Cambridge University Press, New York, 1964).

33. E. R. Jones, J. T. McKinney, and M. B. Webb, Phys. Rev. 151 (2), 476 (1966).

34. A. U. MacRae, Surf. Sci. 2, 522 (1964).

35. A. A. Maradudin and P. A. Flinn, Phys. Rev. 129 (6), 2529 (1963).

36. J. T. McKinney, E. R. Jones, and M. B. Webb, Phys. Rev. 160 (3), 523 (1967).

37. P. J. Estrup, The Effect of Temperature on LEED Intensities from Adsorbed Substances, in The Structure and Chemistry of Solid Surfaces, G. A. Somorjai, ed., (John Wiley and Sons, Inc., New York, 1969).

38. W. L. Bragg and E. J. Williams, Proc. Roy. Soc. 145A, 699 (1934).

39. J. J. Burton, Ph.D. Dissertation, University of California, Berkeley, 1967.

40. F. Jona, Surf. Sci. 8, 478 (1967).

41. D. G. Fedak and N. A. Gjostein, Acta. Met. 15, 827 (1967).

42. A. E. Morgan and G. A. Somorjai, Surf. Sci. 12, 405 (1968).

43. W. P. Ellis, Surface Configuration of the (111) Plane of UO_2, in Fundamentals of Gas-Surface Interactions, H. Saltsburg, J. N. Smith, Jr., and M. Rogers, eds., (Academic Press, New York, 1967).

44. A. Guinier, X-Ray Diffraction, (W. H. Freeman and Company, San Francisco, 1963).

45. R. Kaplow, S. L. Strong and B. C. Averbach, Phys. Rev. 138A, 1336 (1965).

46. D. M. North, J. E. Enderby, and P. A. Egelstaff, J. Phys. Chem., Proc. Phys. Soc. series 2, 1, 1075 (1968).

47. R. Leonhardt, H. Richter, and W. Rossteutscher, Z. Physik 165, 121 (1961).

48. F. Keywell, Phys. Rev. 97, 611 (1955).

49. Phillips Impregnated Cathode, Phillips Metalonics, Mt. Vernon, N. Y.

50. LEED Instruction Manual, Varian Associates, Palo Alto, Calif., January 1968.

51. E. Kozak and J. Morabito, UCRL 18030 (Internal Publication), 1968.

52. Single crystals from Materials Research Corporation, Orangeburg, New York and Alpha Crystals, Bradford, Pennsylvania.

53. J. W. May, Ind. and Eng. Chem. 57 (7), 19 (1965).

54. A. U. MacRae and G. W. Gobeli, J. Appl. Phys. 35, 1629 (1964).

55. L. G. Feinstein and D. P. Shoemaker, Surf. Sci. 3, 294 (1965).

56. J. A. Dillon, Jr., R. E. Schlier, and H. E. Farnsworth, J. Appl. Phys. 30, 675 (1959).

57. H. Tokutaka and M. Trutton, Surf. Sci. 11, 216 (1968).

58. T. M. French, private communication from this laboratory.

59. D. G. Fedak and N. A. Gjostein, Surf. Sci. 8, 77 (1967).

60. T. N. Rhodin and E. W. Plummer, Atomistic Considerations of Surface Binding of Metals, in The Structure and Chemistry of Solid Surfaces, G. A. Somorjai, ed., (John Wiley and Sons, Inc., New York, 1969).

61. S. L. Altman, C. A. Coulson, and W. Hume-Rothery, Proc. Roy. Soc., 240A, 145 (1957).

62. L. Brewer, Prediction of High Temperature Metallic Phase Diagrams, in High Strength Materials, V. F. Zackay, ed., (John Wiley and Sons, Inc., New York, 1965).

63. G. W. Simmons and K. R. Lawless, Trans. Amer. Crystall. Association 4, 72 (1968).

64. F. Jona, Surf. Sci. 8, 57 (1967).

65. A. R. Ubbelohde, Melting and Crystal Structure, (Oxford University Press, Oxford, 1965).

66. F. A. Lindemann, Phyzik Z. 14, 609 (1910).

67. W. K. Burton, N. Cabrera, and F. C. Frank, Phil. Trans. Roy. Soc. 243A, 299 (1951).

68. I. N. Stranski, W. Gans, and H. Rau, Ber. Bunsingessell. 67, 965 (1963).

69. R. M. Stern, A. Gervais, and H. Taub, Dynamical Origin of Electron Diffraction Intensities, in The Structure and Chemistry of Solid Surfaces, G. A. Somorjai, ed., (John Wiley and Sons, Inc., New York, 1969).

70. R. W. G. Wyckoff, Crystal Structures, (Interscience, New York, 1963).

71. W. L. Winterbottom and J. P. Hirth, The Vaporization Kinetics of Solid Silver, in Condensation and Evaporation of Solids, E. Rutner, P. Goldfinger, and J. P. Hirth, eds., (Gordon and Breach, New York, 1964).

72. J. E. Lester, Ph.D. Dissertation, University of California, Berkeley, 1968.

73. J. P. Hirth and G. M. Pound, J. Chem. Phys. 26, 1216 (1957).

74. J. Drowart, Mass Spectrometric Studies of the Vaporization of Inorganic Substances at High Temperatures, in Condensation and Evaporation of Solids, E. Rutner, P. Goldfinger and J. P. Hirth, eds., (Gordon and Breach, New York, 1964).

75. G. A. Somorjai, ASM Trans. Quarterly 57 (1), 26 (1964).

76. G. Ehrlich and F. G. Hudda, J. Chem. Phys. 44 (3), 1039 (1966).

77. N. A. Gjostein and W. L. Winterbottom, The Structure and Properties of Metal Surfaces, in Fundamentals of Gas Surface Interactions, J. N. Smith, Jr. and M. Rogers, eds., (Academic Press, N. Y., 1967).

78. M. Kass and S. Magun, Z. Kristall. 116, 354 (1961).

79. W. B. Hillig and D. Turnbull, J. Chem. Phys. 24, 914 (1956).

80. P. R. Pennington, Ph.D. Dissertation, University of California, Berkeley, 1966.

81. M. Volmer and O. Schmidt, Z. Physik Chem. 85, 467 (1937).

82. R. L. Cormia, J. D. MacKenzie and D. Turnbull, J. Appl. Phys. 34 (8), 2239 (1963).

83. N. G. Ainslie, J. D. MacKenzie and D. Turnbull, J. Chem. Phys. 65, 1718 (1962).

84. R. M. Goodman, H. H. Farrell, and G. A. Somorjai, J. Chem. Phys. 49 (2), 692 (1968).

85. T. Edmonds and R. C. Pitkethly, Surf. Sci. 15, 137 (1969).

86. A. G. Jackson and M. P. Hooker, LEED Study of Growth of Thin Films on the Nb(110) Surface, in The Structure and Chemistry of Solid Surfaces, G. A. Somorjai, ed., (John Wiley and Sons, Inc., New York, 1969).

87. J. E. Lennard-Jones and A. F. Devonshire, Proc. Roy. Soc. (London) A170, 464 (1939).

88. W. A. Harrison, Psuedo Potentials in the Theory of Metals, (Benjamin, New York, 1966).

89. M. Born, J. Chem. Phys. 7, 591 (1939).

90. D. Kuhlmann-Wilsdorf, Phys. Rev. 140 (5A), 1599 (1965).

91. W. T. Read, Jr., Dislocations in Crystals, (McGraw-Hill Book Company, New York, 1953).

92. V. I. Vladimirov, Soviet Solid State Physics, 10 (9), 2077 (1969).

APPENDIX A

Additional Surface Structures

One result of studying materials at high temperatures (up to the melting point) is the possibility for observing surface structures which would not appear at lower temperatures. In two experiments the apparent reactivity of tantalum holders with lead and nickel crystals produced surface structures depicted in Figs. A-1 and A-2. The Pb(111)-Ta? structure formed in a preliminary experiment using Ta holder at temperatures above 275°C. The Ni(111)-Ta? structure formed in an experiment using Ta holders at temperatures above 975°C.

The second group of surface structures are those which are the result of ambient interaction. Since there is no mass spectrometer in my LEED chamber I could not identify which constituents of the ambient were responsible. In this group are the Ni(111)-Q-?, Ni(111)-4×4-CO, Ni(111)-3×3-CO_2 structures reported by Edmonds and Pitkethly[85] attributed to effect of the electron beam on adsorbed ambient CO and CO_2. In addition I've obtained a Ni(111)-7×7 not previously reported as shown in Fig. A-3. In flash desorption studies from this surface, three pressure bursts were observed: the first at about 150°C, second at about 300°C, and a third at about 500°C; the first and third bursts were about ten times as large as the second and the total desorbed gas was about one monolayer. In the studies using nickel holders no other structures formed. The Ni(100) surface showed much less reactivity to ambient gases; other than the 1×1 structure, the only other structure observed was a Ni(100)-2×2-CO. Since its formation correlated with the work by Park,[2] I concluded it was caused by CO absorption. The Pd(111) surface showed very reproducible reactivity to ambient (as indicated in a previous publication) producing a

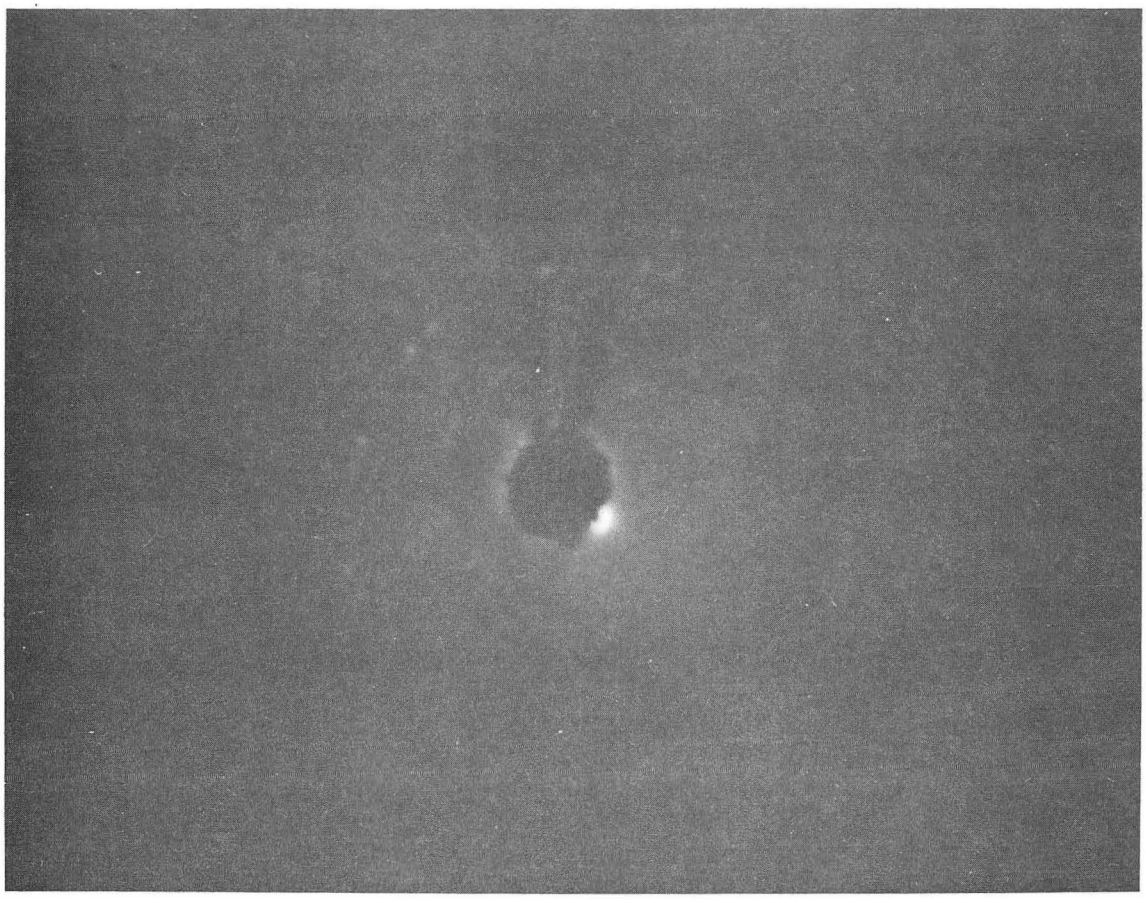

XBB 699-5791

Fig. A-1 LEED pattern from a Pb(111) - ? - Ta structure at 38 eV.

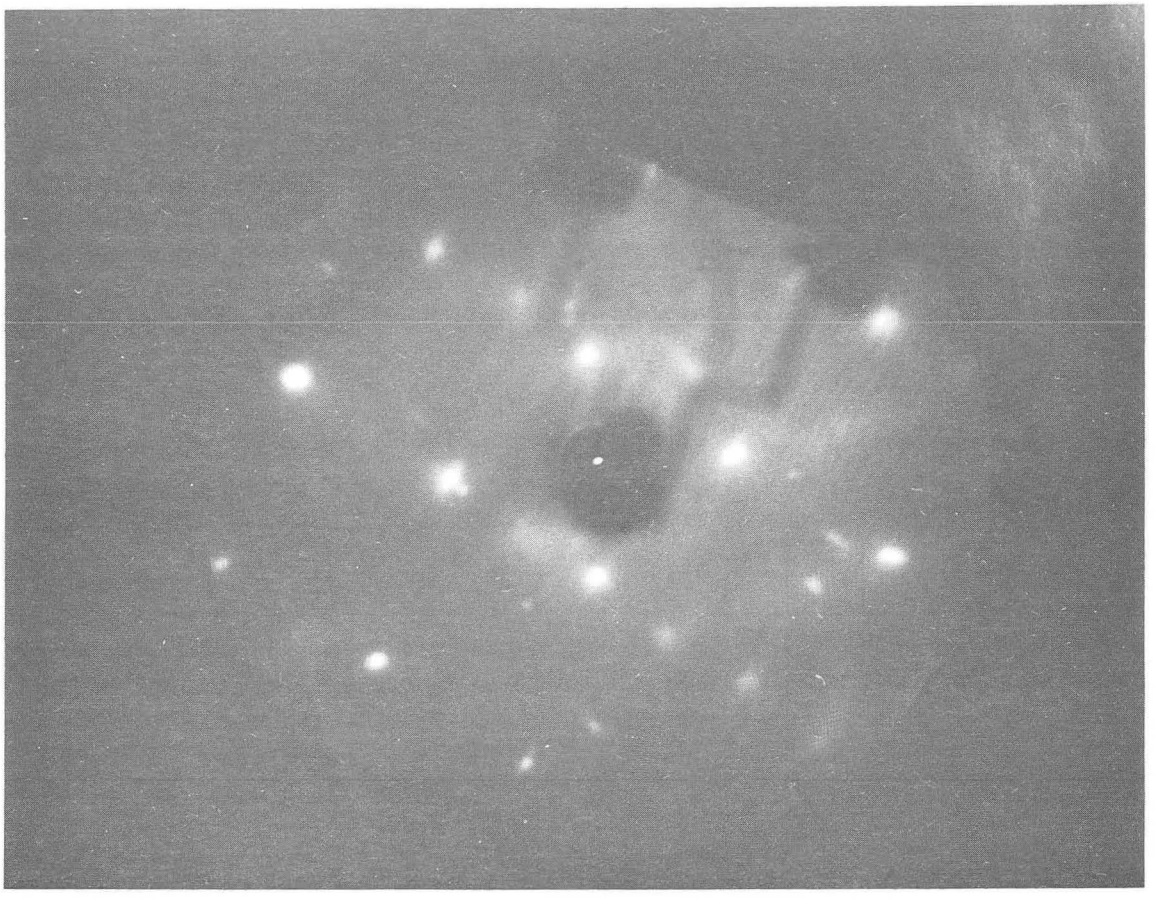

XBB 699-5792

Fig. A-2 LEED pattern from a Ni(111) - ? - Ta structure at 101 eV.

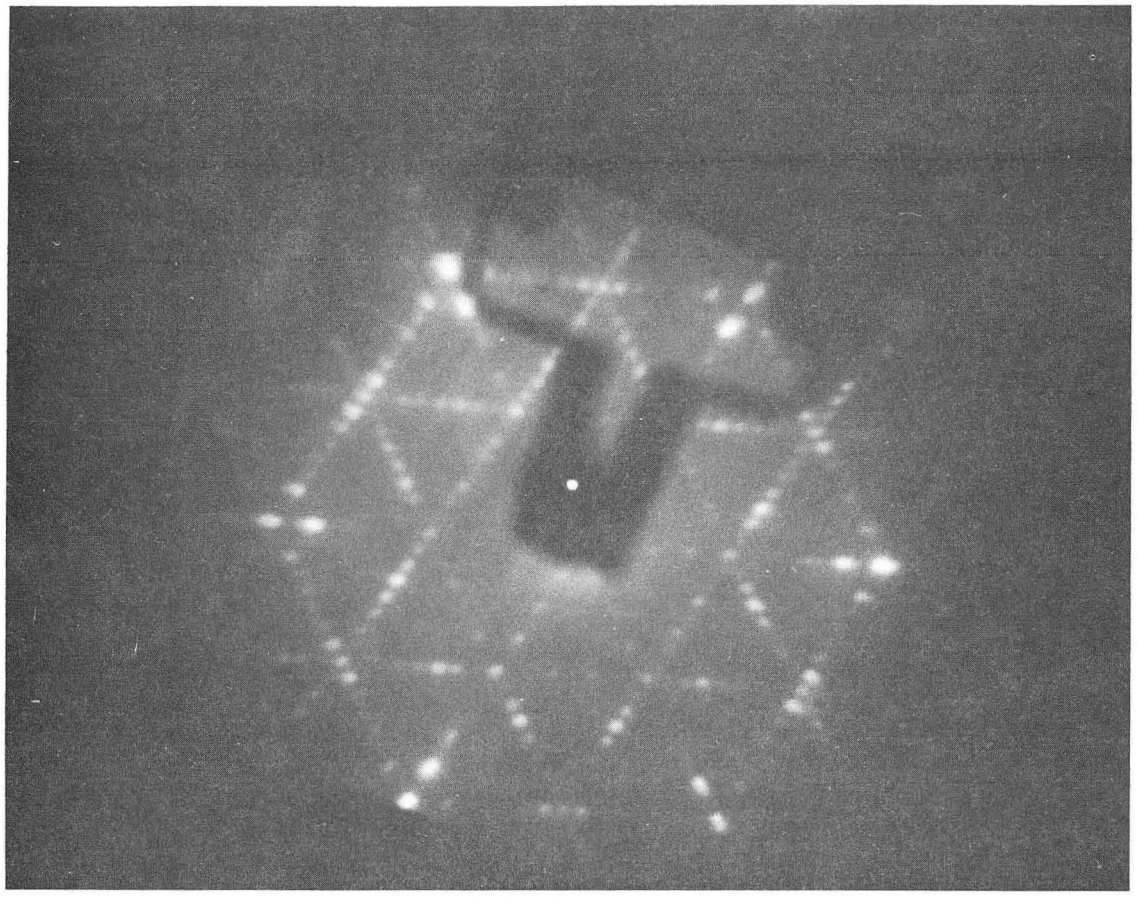

XBB 699-5793

Fig. A-3 LEED pattern from a Ni(111) - 7×7 - ? structure at 109 eV.

Pd(111)$\sqrt{3}$(1x1)R30°-? structure. In fact, kinetics of its formation at room temperature in the ambient were followed photographically, indicating perhaps a sticking coefficient of about 0.3-0.5. Occasionally streaking or other weak diffraction features were observed in addition to the Pd(111)$\sqrt{3}$(1x1)R30° structure, but these were quite irreproducible and were easily eliminated by heating and ion bombarding cycles.

The Sn(110)2x1R31°(?) structure depicted in Fig. IX-2 is a special case. This structure has been reproduced by Jackson and Hooker[86] in epitaxial studies of tin on Niobium(110). However, in neither their nor my studies were the ambient gases monitored. The extra spots disappeared at about 85°C with a dimming of all diffraction features, however, no pressure rise due to desorption was observed. Upon cooling to room temperature a very gradual sharpening of the extra spots was observed. It would be hard to decide without further study whether the structure was due to surface contamination which disordered at about 85°C or if the structure is a property of the clean Sn(110) surface.

The Pb(110) surface between about 150°C-250°C gave a diffraction pattern as shown in Fig. A-4. This pattern is quite unusual in that it does NOT have the symmetry of the substrate and the pattern is not in registry with the substrate. It was obtained in only one-half of the studies and once the surface was heated above 250°C it could not be regenerated by heating to 150°-250°C range again.

The last series of patterns obtained in my experiments are usually labelled ring structures. Two of them; the Ag(100) and Au(100) ring structures have been reported previously. A similar structure was occasionally obtained on the Pb(111) surface and has been found on all

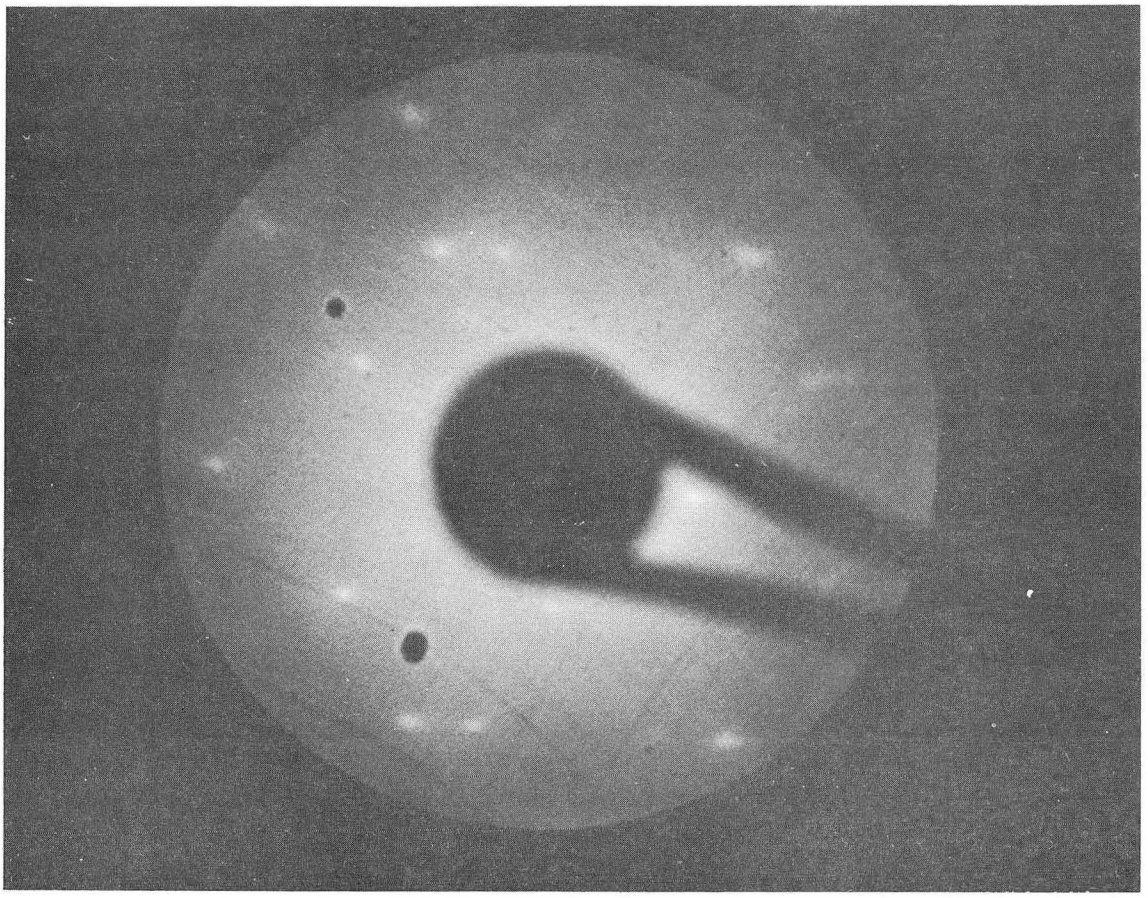

XBB 699-5794

Fig. A-4 LEED pattern from a Pb(110) - ? - ? structure at 59 eV.

three low-index faces of platinum. However, the platinum ring structures have definitely been established as due to carbon contamination from the high temperature "cracking" of ambient hydrocarbons, carbon monoxide or sub-diffusion of carbon from bulk to the surface. The inability to reproduce any of the other ring structures and the designation of the platinum rings as due to carbon suggests the possibility that these rings are due to ambient contaminants or, perhaps, as the other Ag(100) surface structures, is a function of ambient catalysis or mechanical strains.

APPENDIX B

Properties of the Specular Intensity

Most of the data on palladium and lead surfaces have been previously reported.[84] Figures B-1 and B-2 are the results from two the studies which are most related to the study of surface phase transformations by LEED. The major points to be emphasized are: (1) Intensity curves are altered as a function of surface structural changes and, in fact, "fingerprint" the different surface structural changes very accurately. (2) Studies by H. H. Farrell[28] indicate that features of the intensity curves are best described by a multiple scattering theory.

Figures B-3 through B-7 are intensity curves obtained from Pb(110), Bi(0001), Bi(01$\bar{1}$2), Ir(100), and Sn(110) surfaces. The Ir(100) curve fits previous correlations for fcc(100) surfaces quite well. The Pb(110) curve was obtained using a low temperature holder at a temperature of -125°C. The others have been included merely as data which should be useful for future correlations of intensity theories.

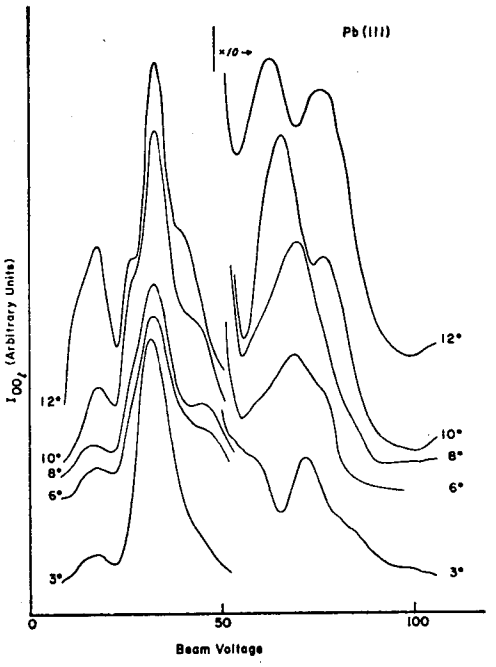

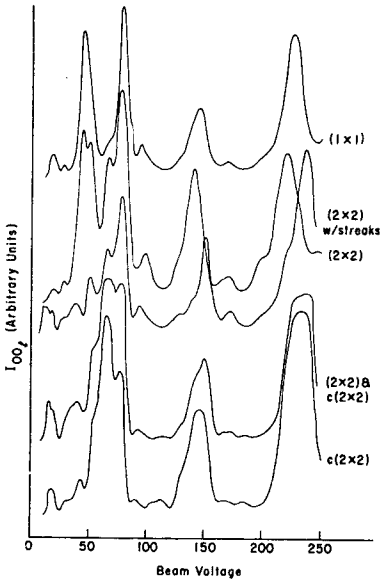

XBL 696-706

Fig. B-1 (Top) Set of I_{00} (eV) curves from a Pb(111) surface as a function of angle of incidence. Intensity scale above 50 eV is expanded 10×.

Fig. B-2 (Bottom) Set of I_{00} (eV) curves from a Pd(100) surface as a function of surface structure as indicated in the legend; angle of incidence 3°.

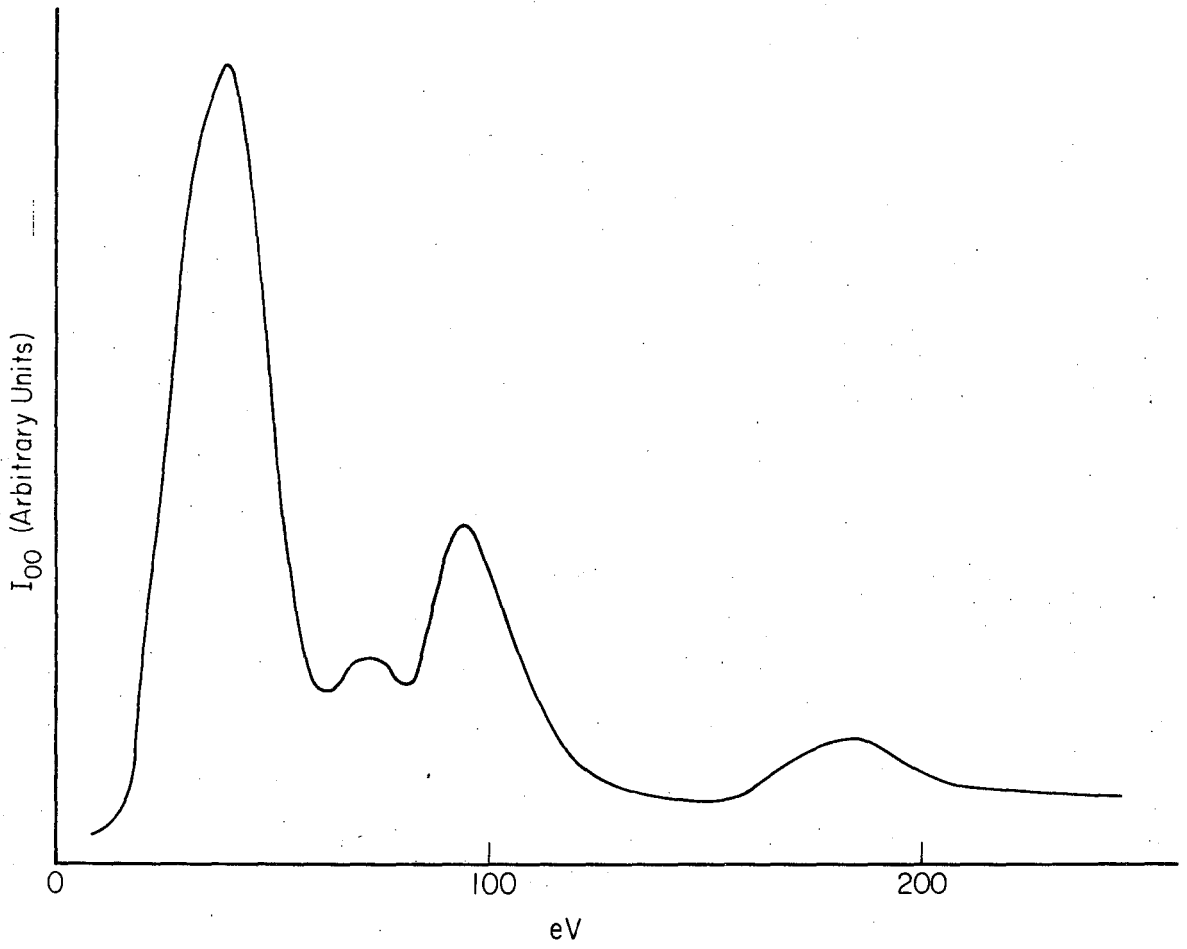

XBL 696-644

Fig. B-3 I_{00} (eV) curve from Pb(110)-1x1 surface at -125°C. Angle of incidence 11°.

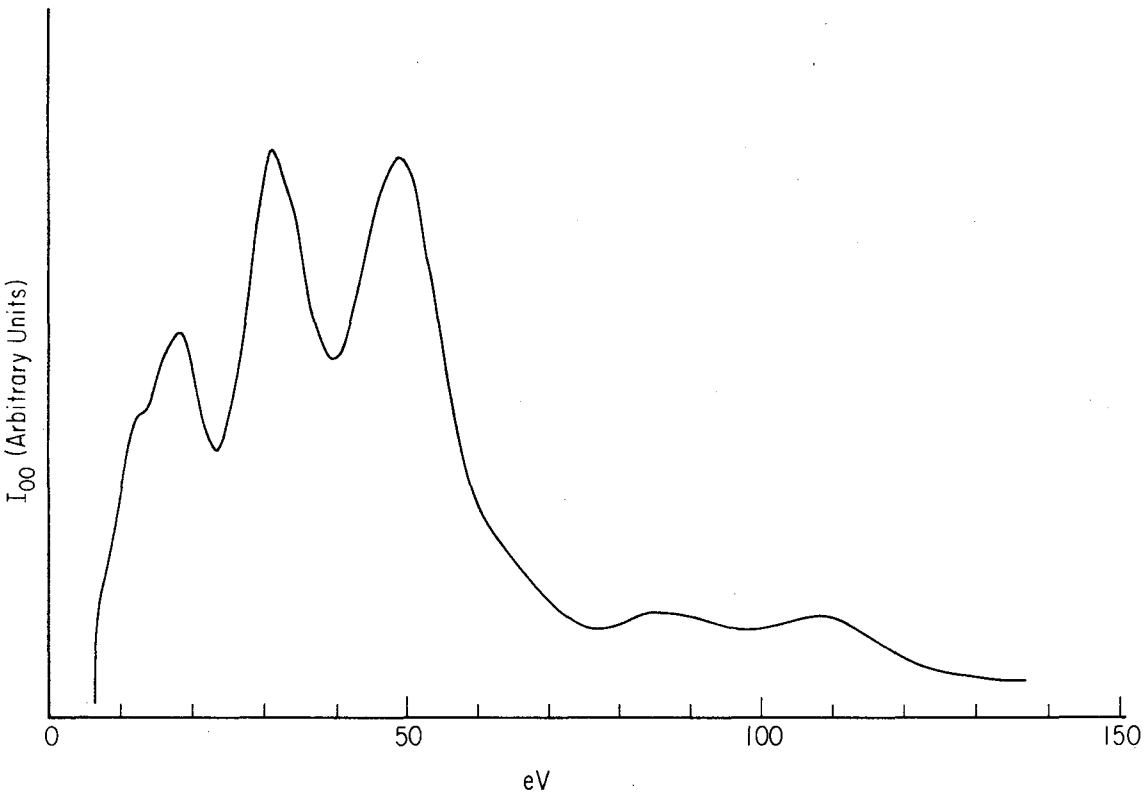

XBL 696-638

Fig. B-4 I_{00} (eV) curve from Bi(0001)-1x1 surface. Angle of incidence 5°.

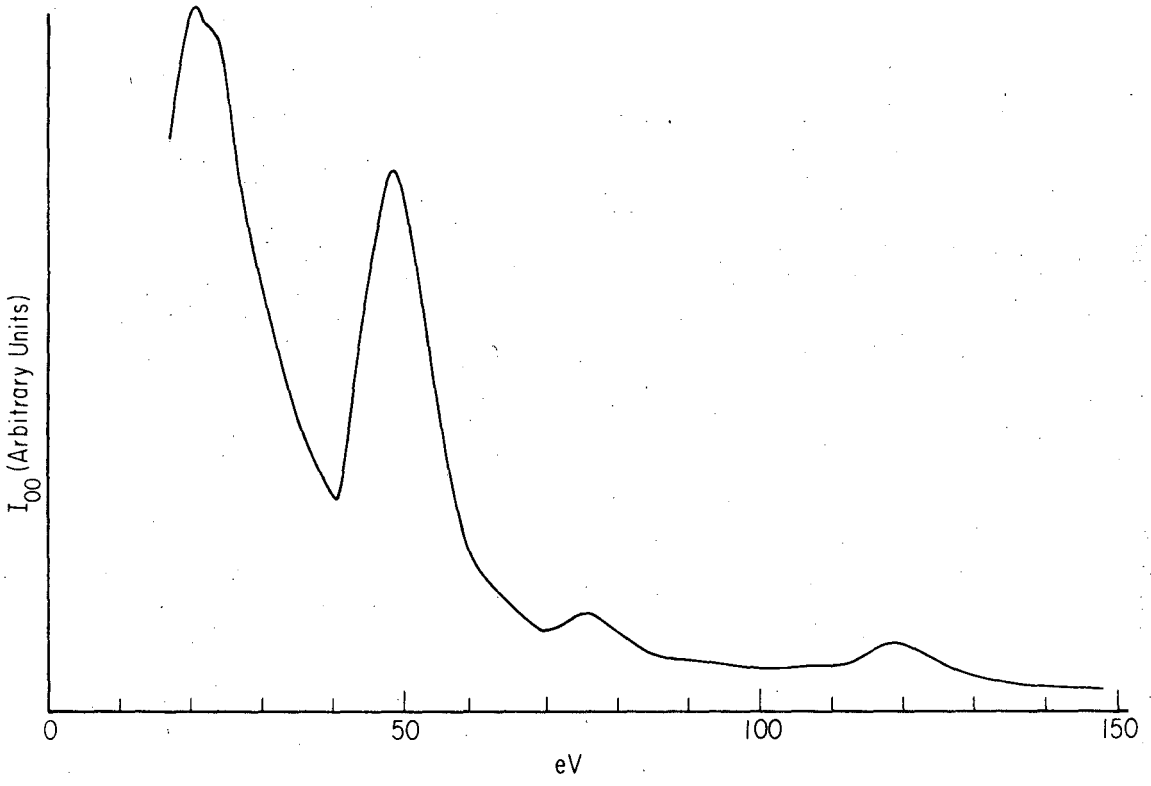

XBL 696-639

Fig. B-5 I_{00} (eV) curve from Bi(01$\bar{1}$2)-1x1 surface. Angle of incidence 5°.

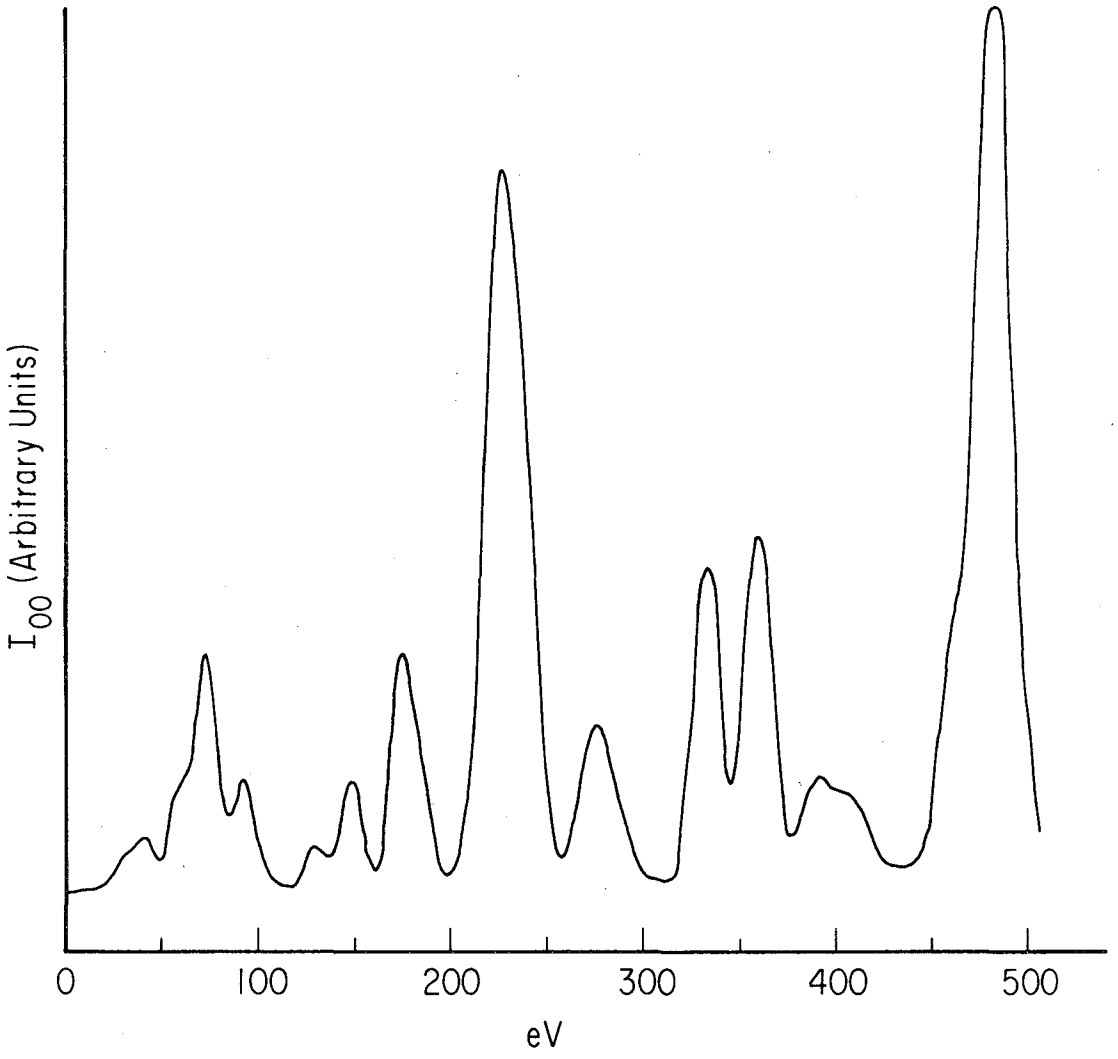

XBL 696-645

Fig. B-6 I_{00} (eV) curve from Ir(100)-1x1 surface. Angle of incidence 4°.

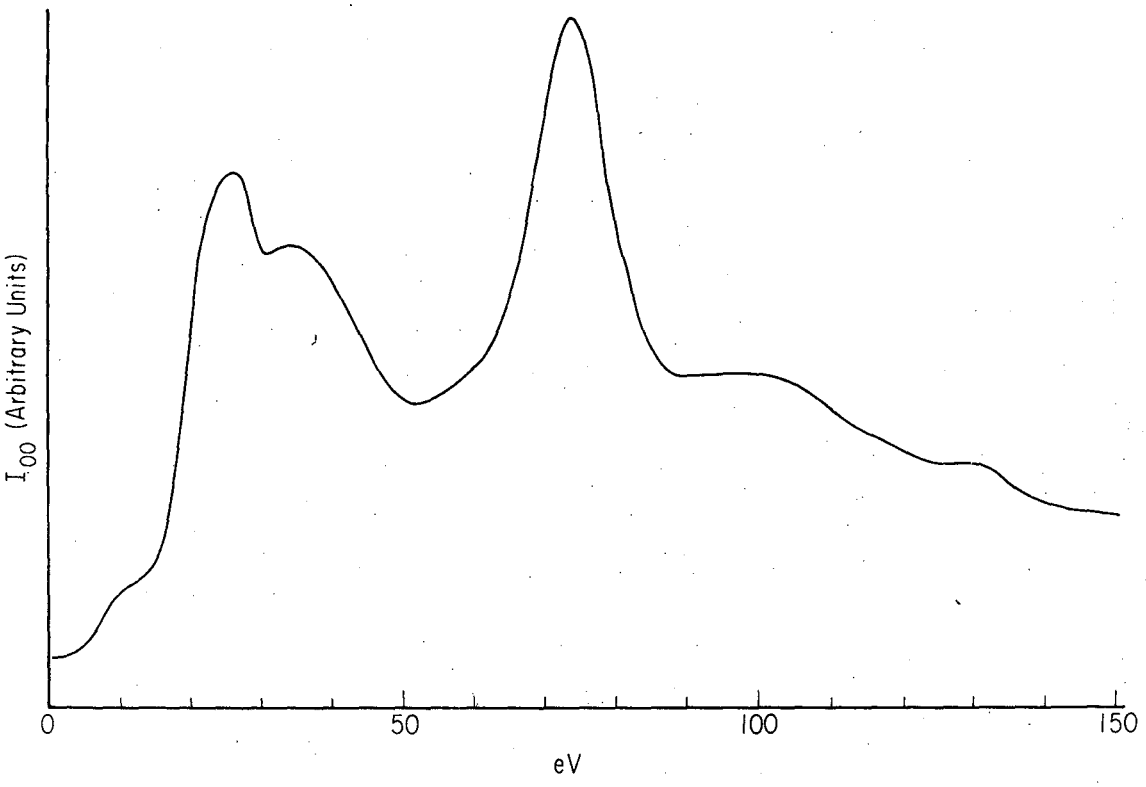

XBL 696-641

Fig. B-7 I_{00} (eV) curve from Sn(110)-2x1-R31°-? structure. Angle of incidence 5°.

APPENDIX C - Theories of Melting

The Lindemann Theory

Perhaps the oldest and most famous theory of melting is attributable to Lindemann.[66] Ironically, Lindemann did not consider his theory as a melting theory at all in titling his paper, "Uber die Berechnung molekularer Eigenfrequenzen." His basic concept was that

$$\nu_E = \text{const} \sqrt{\frac{T_m}{Ma}} \qquad C\ (1)$$

where ν_E = Einstein frequency, M = atomic mass, a = atomic volume. He postulated that melting occurs if the amplitude of the lattice vibrations became so large that atoms "touch." With this assumption the constant in Eq. C (1), which is an empirical observation, can be evaluated. Lindemann obtained

$$\nu_E = \frac{\sqrt{2R}}{\Pi\rho} \sqrt{\frac{T_m}{Mr^2} - \frac{R\beta}{2\pi^2\rho^2 r^2 M}} \qquad C\ (2)$$

where R = gas constant, r = nearest neighbor distance, $\beta = h/k$, h = Planck's constant, k = Boltzmann's constant, and ρ = parameter which characterizes that fraction of nearest-neighbor distance which is equivalent to touching of two atoms. Lindemann calculates a value for ρ from the classical Clausius-Mosotti dielectric theory which is approximately .05 for most materials. Substituting values for all the constants in Eq. C (2), Lindemann obtains for cubic metals,

$$\nu_E = 2.06 \times 10^{12} \sqrt{\frac{T_m}{M \sqrt[3]{a^2}}} \qquad C\ (3)$$

which gives values (relative to heat capacity determinations of ν_E) as shown in Table C-I.

Since Lindemann's original publication several alterations have been

made in the theory to increase the accuracy of its "predictions." For example, recent theorists use the Debye model (though in the high temperature limit the two theories are quite similar) and the ρ parameter has been redefined, as $\langle u^2 \rangle_{Av} = \rho^2 r^2$ according to Gilvarry,[16] where $\langle u^2 \rangle_{Av}$ is the mean square displacement at the melting point determined from Debye-Waller measurements. However, these adjustments to the basic Lindemann theory have not greatly improved the correlations, which are merely empirical correlations between the melting point and Debye temperature (or Einstein frequency). As a "melting theory," the Lindemann model satisfies almost none of the requirements mentioned above, i.e., it does not explain the effect of melting on such physico-chemical properties as density or resistivity, etc. In a modified form (see Eq. C (4) below) it predicts that the surface may melt at a lower temperature (since as shown in Section V, surfaces are characterized by lower θ_D's) than the bulk. In Section VI., it is shown that pre-melting is not found for monatomic metal surfaces.

In summary, therefore, it is best to consider Eq. C (3), or similar equations derived from it, as Gilvarry's formula which reduces to

$$\theta_D = \text{const} \sqrt{\frac{T_m}{M \sqrt[3]{a^2}}} \qquad C\ (4)$$

as merely empirical results which must be explained within a physically more meaningful theory.

Table C-I

Element	Pb	Sn	Pt	Ag	Si	C (diamond)
ν_E, calc.	1.4	1.8	3.1	3.2	7.0	20.8
ν_E, from C_p	1.2	2.7	3.1	3.3	10.7	27.3

The Theory of Lennard-Jones and Devonshire

Lennard-Jones and Devonshire (L-JD)[87] relate melting behavior to the interatomic potential between molecules in the solid. For those solids in which the interatomic potential can be expressed in the form $\phi = \phi_0 (v_0/v)^n$, where ϕ_0 and v_0 refer to the interatomic potential and molar volume at 0°K, respectively, an equation of state can be derived which gives the melting point as $T_m = \beta\phi_0/k$ where β = constant ~ 0.7 and k = Boltzmann's constant. The basic assumption used to derive their equation of state is that melting can be considered a cooperative phenomena arising from catastrophic disordering of the solid lattice. The technique follows the Bragg-Williams[38] theory of order-disorder transition in alloys by postulating the existence of two interpenetrating fcc lattices, called α and β lattices, to describe the structure of the solid. The basic theory assumes: 1) the solid is monatomic, 2) at sufficiently low temperatures the solid is perfectly ordered with all atoms located on the α sites, 3) the solid always remains perfectly isotropic, 4) that the movement of atoms is only between α and β sites and not from α to α sites or interstitial positions. 5) The lattice vibrations can be characterized by the Einstein model of individual atomic cells. If one defines a parameter Q = disorder parameter = number of atoms on α sites relative to the total number of atoms and if the energy necessary for an atom to jump from an $\alpha \rightarrow \beta$ site is described by an energy W of the form $W = W_0 (v_0/v)^l$, then the total partition function for the solid has the form:

$$F(Q) = f^N \gamma(Q) \exp\left[\frac{-ZNWQ(1-Q)}{kT}\right] \qquad C(5)$$

where f = partition function for any particular atomic arrangement of the form,

$$f = \left(\frac{2\pi mkT}{h^2}\right)^{3/2} v_f^* \, e^{-\Phi_0/NkT} \qquad C\ (6)$$

derived from an Einstein model with v_f^* as a parameter representing the average volume occupied by an atom in its "cell," and Φ_0 = equilibrium energy for a particle in its "atomic cell." $\gamma(Q)$ arises from statistical considerations describing the number of ways of arranging N atoms over the α and β sites, or

$$\gamma(Q) = \left\{ \frac{N!}{[NQ]!\ [N(1-Q)]!} \right\}^2 \qquad C\ (7)$$

The Boltzmann factor in Eq. C (5) is the crucial assumption of cooperative behavior, i.e., the energy of any particular configuration is a function of the order present. In effect, for any temperature below T_m, the derived "disorder free energy," $A' = -NkT\ \ell n\ F$ is a minimum for values of Q very near 1.0, but that right at T_m, A is a minimum for Q = 1/2, i.e. totally disordered.

From this model several fusion properties can be derived as volume expansion on melting, the entropy of fusion, or the coefficient of expansion, etc. For the noble gas solids such as argon (for which a potential of the form $\phi = \phi_0 \, (v_0/v)^{\ell}$ has been shown to be reasonable) Table C-II summarizes the success of the L-JD model. However, for other solids (as CO_2 or metals) which do not fit such a potential results differ frequently as much as 50%.

The stylized version of the theory (e.g. restricting atoms to α and β sites) cannot be an accurate physical picture of the melting transition. However, the theory is qualitatively reasonable in predicting a melting

transition with the appropriate physical characteristics and for systems describable by suitably simple potentials is quantitatively accurate. Perhaps, the use of pseudopotentials[88] for metals might produce quantitatively reasonable predictions for the melting properties of metals. The addition of more reasonable potentials may also make possible better predictions for describing the kinetic barriers which cause substances to superheat and undercool or selectively melt at certain sites, etc.

Table C-II Argon

Property	ΔV_m (at 83.8°K)	ΔS_m	P_m $\frac{\text{dynes}}{\text{cm}^2}$ at 90.3°K	α(%/°C)
Calculated	13.5%	1.70k	286×10^6	0.0040
Observed	12.0%	1.66k	291×10^6	0.0045

Born's Melting Theory

Born[89] is most concerned with the fact that liquids have no resistance to low frequency shearing stresses while the solid has relatively high resistance. Mathematically the free energy for a rigid body under shearing, non-torsional stresses can be expressed as a function of the temperature, lattice geometry, and the strain components as for a solid having cubic symmetry:

$$A = N f(T, a, X_x, Y_y, Z_z, Y_z, Z_x, X_y) \qquad C (8)$$

where a = lattice parameter, N = Avogadro's number, X_x, etc. are defined as follows: $2X_x = (a_x^2 - a^2)/a^2$, $2Y_y = (a_y^2 - a^2)/a^2$, $2Z_z = (a_z^2 - a^2)/a^2$, $Y_z = (\underset{\sim}{a}_y \cdot \underset{\sim}{a}_z)/a^2$, $Z_y = (\underset{\sim}{a}_z \cdot \underset{\sim}{a}_y)/a^2$, and $X_y = (\underset{\sim}{a}_x \cdot \underset{\sim}{a}_y)/a^2$ where the $\underset{\sim}{a}_x$, $\underset{\sim}{a}_y$, $\underset{\sim}{a}_z$ refer to the deformed lattice vectors. Born

obtains three stability conditions for the existence of the lattice. He indicates the violation of one of the conditions, that $C_{44} > 0$ where C_{44} is the shear modulus for a cubic crystal, implies the melting of the solid. He calculates the variation of C_{44} with temperature and pressure using the following assumptions: 1) that the lattice possesses cubic symmetry, 2) that thermal motions are harmonic, 3) that the interatomic potential can be expressed in the following form,

$$\phi = -\phi\ (r_0)\ \frac{nm}{n-m}\left[-\frac{1}{m}\left(\frac{r_0}{r}\right)^m + \frac{1}{n}\left(\frac{r_0}{r}\right)^n\right] \qquad C\ (9)$$

where $\phi\ (r_0)$ is the potential at the equilibrium internuclear distance, r_0, and that n and m are real numbers such that $n = 2m$. 4) Only nearest and next-nearest neighbors are significant in describing the lattice dynamics. I will not describe the mathematical detail which is necessary to obtain his solution, the solution itself is defined in the form of a complex set of simultaneous equations. However, the solution can be expressed by graphical means. Analysis of the graphical results gives C_{44} (and hence T_m) as a function of temperature and pressure, i.e., melting occurs at that temperature, T_m where $C_{44} = 0$ for any given pressure in terms of two parameters, $\Theta = \phi\ (r_0)/k$ and $p = R\,\Theta/V_0$ where R = gas constant, h = Boltzmann's constant, V_0 is the molar volume corresponding to r_0 for the equilibrium internuclear separations. Taking reasonable values for r_0 and $\Phi(r_0)$ he obtains data which fit the Lindemann relation and the Clausius-Clapeyron equation at high pressures qualitatively well.

Born has studied the question of the nature of melting in a very reasonable fashion; concentrating on one of the most dramatic differences between solids and liquids, namely the difference in ability to resist shearing forces. Despite theoretical and mathematical difficulties in

evaluating the stability conditions for a lattice he obtains reasonable solutions. Unfortunately, as Born was well aware, his theory presents no model for the liquid state and thus he cannot compare his theory with properties as ΔH_f, ΔS_f, etc. Finally, to make the mathematics tractable he had to use a potential as in Eq. C (9) which cannot be considered to be very satisfying to describe metallic solids.

The Theory of Kulhmann-Wilsdorf

In this model[90] the free energy of formation of dislocations is taken as positive in solids, as negative for liquids, and the melting temperature is postulated to be the temperature at which the free energy is zero. Thus, liquids are described as infinitely dislocated solids. The mathematical formalisms for dealing with dislocations are already well established, however, the quantitative calculation of the relevant energies of interaction between dislocations is still imprecise due to difficulties in performing the requisite experiments. The basic assumption of this model is supported by experimentally established properties of dislocations: 1) that dislocations are not thermodynamically stable below the melting point of solids and anneal out as the temperature is increased,[80] further, dislocation-free materials have been grown.[80] 2) That those properties most effected by dislocations are: resistance to shear and atomic ordering. Properties as heat capacity, molar volume, resistivity, etc. are almost unaffected by the presence of dislocations. Thus, characterizing liquids as "infinitely" dislocated solids seems qualitatively reasonable.

The quantitative aspects of the Kuhlmann-Wilsdorf model are based on

standard forms[18,91] for calculations for entropy and energy effects of dislocations. Kuhlmann-Wilsdorf obtains the melting point as

$$T_m = \frac{G\, r^3}{12\pi g k} \left(\frac{\alpha}{\chi}\right) \quad , \qquad C\ (10)$$

where G = modulus of rigidity, r = nearest neighbor distance (or shortest Burger's vector allowed for an edge dislocation in the solid), g = Gruneisen constant, k = Boltzmann's constant; (α/χ) is a parameter which is a function of the lattice but must vary between $(1/2 \rightarrow 4)$ based on the constraints of the formulation. The only quantitative check which is reasonable is to assume the correctness of Eq. C(10) which gives a value to the (α/χ) parameter and compares with other derived quantities. For example, the heat of fusion calculated from the model is:

$$\Delta H_m = \frac{3GM}{4d} \left(\frac{\alpha}{\chi}\right)\left(\frac{\chi}{q}\right) \qquad C\ (11)$$

where M = atomic weight of element, d = density and q is determined from an ideal lattice and represents the reciprocal of the maximum shear deformation, parallel to the crystallographic slip plane, which an ideal, dislocation-free crystal of the material could support. Table C-III lists the values of (α/χ) derived from Eq. C(1) and compares the experimental results for ΔH_m with these calculations from this theory.

Quantitative accuracy is not really expected for this model (as discussed above since it depends on such poorly known experimental values as, for example, the modulus of rigidity). However, the agreement is very encouraging and the physical assumptions are reasonable.

A recent model proposed by the Soviet worker Vladimiov[92] based on vacancies as the key defects (rather than dislocations) leads to reasonable quantitative results, also. Considering melting as the result of defect interaction provides a very illuminating basis for looking at the melting transition.

Table C-III

Substance	r(Å)	10^{-11}G (dynes/cm^2)	G	T_m(K)	$(\alpha/X)^{-1}$	(X/q)	ΔH_m (cal/mole) calc.	expt.	error
silver	2.95	1.76	2.40	1233	0.29	0.023	2580	2690	4%
nickel	2.54	4.50	1.88	1723	0.44	0.033	4000	4240	6%
lead	3.54	0.45	2.73	6006	0.24	0.018	1100	1160	6%
silicon	3.92	3.82	~ 2	1694	1.30	0.041	12000	12150	2%
aluminum	2.93	1.90	2.17	932	0.45	0.029	2200	2310	5%

The Theory of Stranski

Stranski's[68] model for melting is based on his studies of the stability of certain crystal surfaces as a function of temperature. He has found that certain crystal surfaces facet and are wetted by their own melt, while other faces remain stable and are not wetted by the melt even at temperatures very near the melting point. These results lead to a consideration of melting as a function of crystal surface, i.e. different cyrstal faces "melt" at different temperatures. According to Stranski, "melting" in his context refers to the ability of a crystal face to support large equilibrium concentrations of adsorbed (or disordered) atoms on its surface. The following equation relates the concentration ,n, of these "adsorbed" atoms to a parameter, β, and the absolute temperature:

$$n = n_{\infty} \exp\left[-\beta\phi_{1/2}/2kT\right] \qquad C\ (12)$$

where β = ratio of the binding energy for an atom in an equilibrium position in a particular surface plane to that in the half-crystal position ($\phi_{1/2}$) (which is equal to the average surface binding energy of atoms in the solid). The value of n = concentration of adsorbed atoms in equilibrium at any given absolute temperature, T; n_{∞} = the concentration of atoms/unit surface area for a particular crystal face. Actually, β, n and n_{∞} are functions of the particular surface and could be written as $\beta_{hk\ell}$, $n_{hk\ell}$, etc. Thus, large values of $\beta > 1$ imply stable faces, with very low concentration of "adsorbed" atoms and small values of $\beta < 1$ lead to high concentrations of adsorbed atoms and "pre-melting." For close-packed monatomic solids, if one assume all nearest-neighbor interatomic bonds are equivalent, then the value of β is proportional to the number of nearest neighbors. For example, $\beta_{111} = 9/6 = 1.5$, $\beta_{100} = 8/6 = 1.33$,

$\beta_{110} = 6/6 = 1.00$, where the value "6" in the denominators refers to the number of nearest-neighbors in the half-crystal position. Thus, according to Stranski, the (100) and (111) faces of fcc metals should not pre-melt and should form the equilibrium faces for the solid grown from the melt (in agreement with results discussed in Section VI and VIII). However, the (110) face is a special case in the Stranski model in that $\beta_{110} = 1.0$. Thus, effects of next-nearest neighbors, etc. would determine whether pre-melting might exist for this face. Several experimental results on the mechanisms of melting reported by Turnbull[79] and others are discussed in the next section and corrolate with the Stranski model.

The Stranski model postulates that melting initiates on high-index faces where β values are less than unity. The low-index faces (i.e. where $\beta > 1$) are stable at all temperatures to T_m (or higher) but that the melting of the "corners" or at the edges of these faces eventually leads to the melting of these faces by growth of the liquid from these edges inward. However, there is one very major flaw in the Stranski model: he presents no justification for the observed invariant bulk melting point. In short, there is no way or predicting from the Stranski model the thermodynamically observed melting point for a substance.

The Experimental Results on Melting

The most important results obtained from experiments on melting behavior are: 1) Careful studies indicate that several materials can be superheated and that in all cases growth of the liquid phase proceeds from definite sites, variously defined as "loose spots," faces not of the equilibrium form, or simply ledges, dislocations, etc. For example, studies by Pennington[80] and Volmer and Schmidt[81] indicate that not only can gallium be superheated but that nucleation of the liquid phase can occur at sites far removed from the source of heat input (i.e. the hottest region) and the advancing melting front. 2) Studies performed by Kass and Magun[78] indicate that ice can be superheated (0.30°C) by focussing radiation on the interior of the crystal despite the fact that all faces of ice are wetted by the melt. 3) Turnbull[79] has calculated the velocity, u, of the melting front in superheated solids,

$$u = [f\Delta H_m (T-T_m)/T_m] [3\pi\lambda^2\eta N] \qquad C (13)$$

where η = viscosity at a temperature $T > T_m$, λ = a "jump distance" and f = a parameter describing the fraction of interfacial sites at which melting can occur. This formula has been shown to be qualitatively accurate on melting studies of superheated SiO_2,[83] P_2O_5,[82] and gallium[80] metal, the former to temperatures as much as 300°C above the melting point. 4) My results which indicate that the (110) as well as the (111) and (100) faces of lead and the (0001) and (01$\bar{1}$2) faces of bismuth remained ordered up to the bulk melting point. This section has discussed several models, none of which explain even a part of these results. A possible qualitative suggestion to resolve this question has been discussed in the conclusions to my studies in Section X .

LEGAL NOTICE

TECHNICAL INFORMATION DIVISION
LAWRENCE RADIATION LABORATORY
UNIVERSITY OF CALIFORNIA
BERKELEY, CALIFORNIA 94720